Characterizing Reactive Nitrogen Sources and Abundances in Under-Sampled Regions of the World using Aircraft, Satellite Observations, and 3D Global Modelling

by

Nana Wei

A dissertation submitted in partial fulfilment

of the requirements for the degree of

Doctor of Philosophy
of
University College London

Department of Geography
University College London

September 16, 2025

I, Nana Wei confirm that the work presented in my thesis is my own. Where information has been derived from other sources, I confirm that this has been indicated in the thesis.

Abstract

Oxidized reactive nitrogen (NO_y) influences global climate, air quality, and atmospheric chemistry. But the understanding of its sources and abundances is limited and outdated in under-sampled areas of Sub-Saharan Africa and the global upper troposphere (UT; ~8-15km). This thesis utilizes sporadic NASA DC-8 aircraft campaign observations, screened for plumes and stratospheric influence, to characterize UT NO_y composition and evaluate current knowledge of UT NO_y as represented by a state-of-science model (GEOS-Chem). The use of DC-8 data is supported by its ability to reproduce NO_y seasonality from routine commercial aircraft measurements. I find that peroxyacetyl nitrate (PAN) dominates UT NO_y (30-64% of NO_y), followed by nitrogen oxides ($NO_x \equiv NO + NO_2$) (6-18%), peroxynitric acid (HNO_4) (6-13%), and nitric acid (HNO_3) (7-11%). The model consistently overestimates peroxypropionyl nitrate (PPN) and underestimates NO_2, as the model is missing PPN photolysis. An ~80 pptv (20-fold) underestimate in modelled methyl peroxy nitrate (MPN) over the Southeast US results from uncertainties in chemical aging of air masses. I derive top-down estimates of hotspot NO_x emissions in Sub-Saharan Africa using satellite observations from TROPOMI to address data gaps for a rapidly growing region. I estimate annual (2019) top-down NO_x emissions of 20 isolated hotspots totalling 322.8 Gg NO_x that range from 0.95 Gg for Ibadan (Nigeria) and Hwange (Zimbabwe) to 101 Gg for the industrial Highveld in South Africa. The agreement between modelled and TROPOMI NO_2 is significantly improved for large hotspots in South Africa when scaling down a widely used bottom-up emission inventory to match my top-down NO_x than the default. Both local and regional inventories overestimate hotspot NO_x emissions in South Africa by up to 65%. Further advancement of knowledge should focus on UT NO_y sources, advection, chemical processing, and NO_x emissions in data-deficit regions like Sub-Saharan Africa.

Impact statement

I use aircraft observations and modelling to characterise reactive nitrogen compounds that affect tropospheric ozone abundance and short-term climate. Not only does this inform future measurement campaigns to further advance our knowledge, but this also provides key information to assess tropospheric ozone abundances more accurately. This is crucial for determining the climate impact of one of the most important short-term climate forcers to feed into assessments like the Intergovernmental Panel on Climate Change (IPCC). A more certain estimate of the radiative forcing aids us in deciding how to prioritise climate actions and policies to mitigate anthropogenic influence on tropospheric ozone. I derived observationally-informed estimates of hotspot emissions of NO_x in Sub-Saharan Africa that was not possible before developing a method to automate sampling area selection that improves the success of the inverse method I use. Air quality modellers can apply these estimates to models to better estimate and attribute the formation of air pollutants, such as $PM_{2.5}$ and surface ozone, which are hazardous to human health, negatively impact food security, and alter the climate. Sub-Saharan Africa is a region that has scarce resources dedicated to air quality regulations, especially for developing routine, reliable inventories of emissions. This approach that I use addresses this data deficit without the need for computationally intensive models. I demonstrate that the top-down emissions values are reliable by using satellite observations and a model to assess these. This validation step is missing in almost all studies that use the same top-down method. Demonstrating reliability of the emissions estimates increases the possibility that regulators will use these data to inform policy decisions.

Research Paper Declaration Form

Details are provided below for a manuscript that is published that form part of my PhD research presented in this thesis. Required information, as per UCL guidelines, are given in italics.

1. For a research manuscript that has already been published.

(a) What is the title of the manuscript?

Characterization of reactive oxidized nitrogen in the global upper troposphere using recent and historic commercial and research aircraft campaigns and GEOS-Chem

(b) Please include a link to or doi for the work:

https://doi.org/10.5194/acp-25-7925-2025

(c) Where was the work published?

Atmospheric Chemistry and Physics (ACP).

(d) Who published the work?

European Geosciences Union (EGU)

(e) When was the work published?

25 Jul 2025

(f) List the manuscript's authors in the order they appear on the publication:

Nana Wei (NW), Eloise A. Marais (EAM), Gongda Lu (GL), Robert G. Ryan (RGR), and Bastien Sauvage (BS)

(g) Was the work peer reviewd?

Yes, as per standard for ACP articles.

(h) Have you retained the copyright?

Yes — The article is Open Access under the Creative Commons Attribution 4.0 License (CC BY 4.0), so authors retain copyright.

(i) Was an earlier form of the manuscript uploaded to a preprint server (e.g. medRxiv)? If 'Yes', please give a link or doi

Yes, the earlier form of the manuscript was uploaded to EGUsphere and here is the link: https://egusphere.copernicus.org/preprints/2024/egusphere-2024-3388/

2. For multi-authored work, please give a statement of contribution covering all authors:

Study concept by EAM and NW. NW led the data analysis, simulated GEOS-Chem and led writing all sections of the manuscript. EAM supervised the project and co-wrote the manuscript. GL aided in data analysis, RGR in the use of ObsPack, and BS in the use of IAGOS NO_y *observations. All authors reviewed and edited the manuscript.*

3. In which chapter(s) of your thesis can this material be found?

The submitted manuscript is integrated throughout the thesis, typically in the first subsections of the Introduction, Methodology, Results and Discussion and Conclusions

Acknowledgements

First and foremost, I would like to express my gratitude to my supervisor, Prof. Eloïse Ann Marais, for her invaluable guidance, patience, and support throughout my PhD journey. Her mentorship has shaped my research, strengthened my confidence, and equipped me with essential academic and professional skills. Her encouragement, belief in my potential, and intellectual curiosity have inspired me to explore my work more deeply, making this journey challenging, exciting, and rewarding. I am also sincerely grateful for her support in securing a PhD studentship that covered my international tuition fees and offering a project funding for living expenses, making this research possible.

I would also like to extend my sincere thanks to Keita Sekou, Rebecca Garland, and Mogesh Naidoo for sharing the latest emission inventories, a crucial part in my study. I also appreciate the DC8, IAGOS, and TROPOMI research teams for their valuable data, which form the foundation of my research. I am also grateful to NASA, ESA, ECMWF, and the European Commission for making their datasets publicly available.

I am grateful to Prof. Clifford Ben for offering me a research assistant position, Prof. Jonathan Holmes for the opportunity to serve as a teaching assistant, and Dr. Ellen Webborn for her mentorship meetings, all of which have made my PhD journey more fulfilling. I also extend my sincere appreciation to my master’s tutor, Prof. Alasdair Rae, and my bachelor’s supervisor, Prof. Wu Hanning. Their guidance, encouragement, and support during my early academic years inspired me to pursue this PhD.

I would also like to express my gratitude to all my friends and colleagues, both past and present, at University College London (UCL) for their invaluable support through problem-solving sessions, peer-to-peer feedback, and social gatherings. A special thanks to Karn for his guidance and support in every issue I have sought advice on, Gongda for discussing my coding questions, Connor for his suggestions and kindness during my challenging moments, and

Bex and Eleanor for their support, kindness, and encouragement. I am grateful to all of you for fostering an inclusive and supportive research environment that has made my time at UCL enjoyable.

I feel blessed to have met Yueting Cui, Tariq, Yuguang Dang, Fan Jia, Yuan Mao, Amada, Casper, Jane, Yu Cui, Jiazhagn Qian, Dongyue Li, Zhaoge, Jize, Linqi, LiuBo, ZhaoBo, Guoguo, Trisita, Jie, Wanxin, Feng, Bin, Huilin who have made my life in London memorable.

Finally, and most importantly, I would like to express my gratitude to my parents, for their endless support, both emotionally and financially, to Will for helping me push through the toughest times.

This PhD journey has been one of the most challenging yet rewarding experiences of my life, and I am thankful to everyone who has been a part of it.

Table of Contents

List of Figures

List of Tables

List of Abbreviations

AEIC	Aviation Emissions Inventory Code
ALKNs	alkyl nitrates
AMFs	air mass factors
AMS	Aerosol Mass Spectrometer
APAN	peroxyacryloyl nitrate
ARCTAS	Arctic Research of the Composition of the Troposphere from Aircraft and Satellites
ATom	Atmospheric Tomography Mission
BrO	bromine monoxide
C1 ALKN	methyl nitrate
C3 ALKN	isopropyl nitrate
CARIBIC	Civil Aircraft for the Regular Investigation of the Atmosphere Based on an Instrument Container
CEDS	Community Emissions Data System
CEDSGBD-MAPS	CEDS developed for the Health Effects Institutes the Global Burden of Disease – Major Air Pollution Sources project
CEMS	Continuous Emissions Monitoring
CH_3O_2	methyl peroxy radical
CH_4	methane
CIMS	chemical ionization mass spectrometry
CL	chemiluminescence

CO	carbon monoxide
CO_2	carbon dioxide
CSIR	Council for Scientific and Industrial Research
CTMs	Chemical Transport Models
DACCIWA	Dynamics-aerosol-chemistry-cloud interactions in West Africa
DC3	Deep Convective Clouds and Chemistry
DICE-Africa	Diffuse and Inefficient Combustion Emissions in Africa
DOAS	differential optical absorption spectroscopy
EDGAR	Emissions Database for Global Atmospheric Research
EMG	Exponential Modified Gaussian
ESA	European Space Agency
GC	GEOS-Chem
GEOS	Goddard Earth Observing System
GEOS-FP	Goddard Earth Observing System Forward Processing
GFAS	Global Fire Assimilation System
GFED4s	Global Fire Emissions Database version 4 with small fires
GMAO	Global Modelling and Assimilation Office
GOME	Global Ozone Monitoring Experiment
H_2	hydrogen
HCN	hydrogen cyanide
HEMCO	Harmonized Emissions Component

HNO_3	nitric acid
HNO_4	peroxynitric acid
HO_2	hydroperoxyl radical
HTAP	Hemispheric Transport of Air Pollution
IAGOS	In-service Aircraft for a Global Observing System
INTEX-NA	Intercontinental Chemical Transport Experiment-North America
JPL	Jet Propulsion Laboratory
KORUS-AQ	Korea-United States Air Quality
KPP	Kinetic PreProcessor
LIF	Laser Induced Fluorescence
LST	local solar time
MEGAN	Model of Emissions of Gases and Aerosols from Nature
MERRA-2	Modern-Era Retrospective Analysis for Research and Applications
MOZAIC	Measurement of Ozone and Water Vapor by Airbus In-Service Aircraft
MPAN	peroxymethacryloyl nitrate
MPN	methyl peroxy nitrate
N	nitrogen atoms
N_2O_5	dinitrogen pentoxide
NASA	National Aeronautics and Space Administration
NO	nitrogen oxide
NO_2	nitrogen dioxide
NO_3	nitrate radical

NO_x	nitrogen oxides
NO_y	oxidised reactive nitrogen
O	oxygen atoms
O_3	ozone
OH	hydroxyl radical
OMI	Ozone Monitoring Instrument
OPE	O3 production efficiency
PAN	peroxyacetyl nitrate
PANs	peroxyacyl nitrates
PANTHER	PAN and Trace Hydrohalocarbon
PBzN	peroxybenzoyl nitrate
PiBN	peroxyisobutyryl nitrate
PnBN	peroxy-n-butyryl nitrate
pNO_3	aerosol nitrate
PNs	peroxy nitrates
PPN	peroxypropionyl nitrate
PSS	photochemical steady state
$RC(O)O_2$	peroxy acyl radicals
RO_2	organic peroxy radicals
RO_2 (non-acyl)	non-acyl peroxy radicals
S5P-PAL	Sentinel-5P Products Algorithm Laboratory
SCD	slant column density
$SEAC^4RS$	Studies of Emissions and Atmospheric Composition, Clouds and Climate Coupling by Regional Surveys
TD-LIF	Thermal–Dissociation LIF

TES	Tropospheric Emission Spectrometer
TROPOMI	TROPOspheric Monitoring Instrument
UT	Upper troposphere
UV	Ultraviolet
VOCs	Volatile Organic Compounds
WAS	Whole Air Samplers

1: Introduction

1.1 Tropospheric Reactive Nitrogen Sources, Chemistry, and Fate

The chemical family of reactive oxidised nitrogen (NO_y) defined as the sum of nitrogen oxide (NO) and nitrogen dioxide (NO_2), collective called nitrogen oxides (NO_x), and NO_x reservoir compounds are crucial in atmospheric chemistry. NO_y impacts air quality, climate, and the oxidizing capacity of the whole troposphere (Bradshaw et al., 2000; Dahlmann et al., 2011; Mickley et al., 1999; Worden et al., 2011; Wei et al., 2024). The availability of NO_x impacts tropospheric ozone (O_3) formation, an air pollutant and the third most important greenhouse gas in terms of radiative forcing after carbon dioxide (CO_2) and methane (CH_4) (Dahlmann et al., 2011; Rap et al., 2015; Worden et al., 2011). NO_y also impacts the abundance of the hydroxyl radical (OH), the main atmospheric oxidant that determines the rate of removal of air pollutants carbon monoxide (CO) and volatile organic compounds (VOCs) and the long-lived greenhouse gas CH_4 (Butler et al., 2020; Murray et al., 2013; Seltzer et al., 2015). Understanding NO_y sources and abundances is essential for modelling OH and O_3, developing policies and strategies to mitigate air pollution and climate change (Singh et al., 2007; Geddes& Martin, 2017; Butler et al., 2020).

The emission of NO_y is from direct release of NO_x (NO + NO_2) into the atmosphere. Global annual NO_x emissions are estimated to total about 57 teragram (Tg) N based on modelling for the year 2015 (Shah et al., 2023). Fossil fuel combustion by vehicles, ships, power plants, and industrial processes contributes ~60% (Hoesly et al., 2018). Open burning of biomass, that is, the burning of vegetation types like savannas and forests, and burning of agricultural waste, contributes ~12% (Fowler et al., 2013; Giglio et al., 2013). The key regions of biomass burning are the tropics, particularly Sub-Saharan Africa, the Amazon Basin, and India, and boreal regions, such as Canada, and

Siberia (Randerson et al., 2012). Microbial activities in soils, classified as natural emissions, accounts for ~14% of NO_x (Hudman et al., 2012). These are all processes occurring at the surface, those that release NO_x aloft include lightning emissions contributing ~10% to the global total (Murray et al., 2012) and aircraft emissions accounting for ~2% (Stettler et al., 2011). The other non-emitting NO_x sources that contribute to NO_y in the troposphere include downwelling of stratospheric air masses laden with nitric acid (HNO_3) and NO_2 that also promote prompt formation of peroxyacetyl nitrate (PAN) on mixing with cold upper tropospheric air (Liang et al., 2011; Jacob et al., 2010; Levy II et al., 1980).

Figure 1.1 presents the oxidized reactive nitrogen reaction pathways in the troposphere, starting with primary emissions of NO_x. High flame temperatures (~2000 K) during combustion of fossil fuels thermally dissociate O_2 into oxygen atoms (O) and N_2 into nitrogen atoms (N) to produce NO (Singh et al., 2007; Miyazaki et al., 2003; Geddes& Martin, 2017). This process generates "thermal NO_x". At lower flame temperatures, such as those that result from burning of biomass, NO and NO_2 form from oxidation of nitrogen in the fuel, termed "fuel NO_x" (Ye et al., 2017).

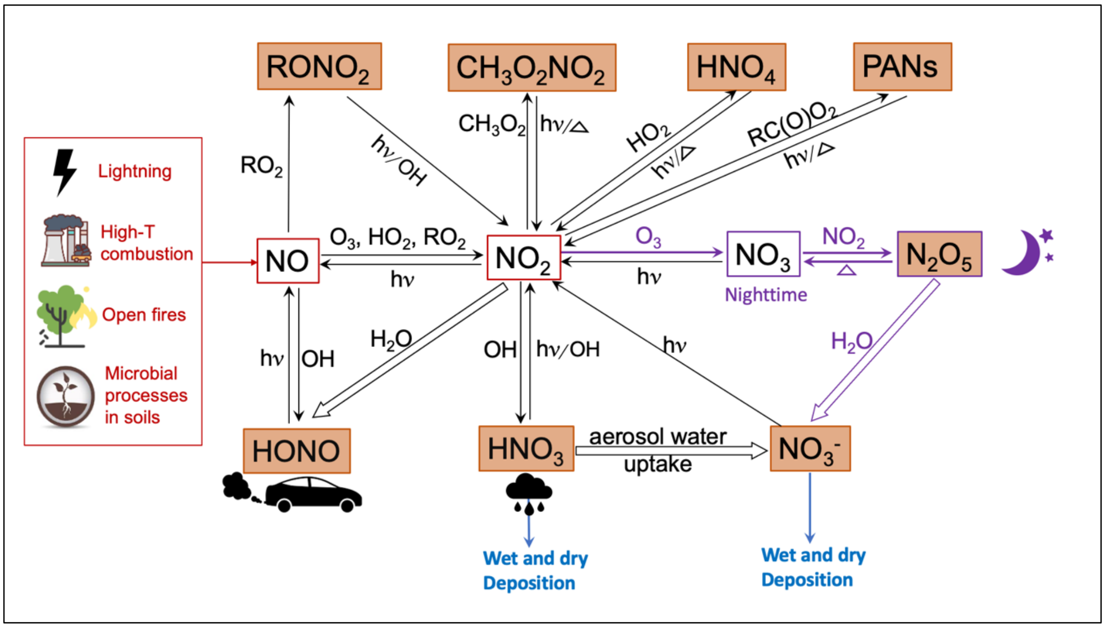

Figure 1. 1: Oxidized nitrogen reaction pathways in the troposphere. Colours indicate NOx reservoirs (filled orange boxes) and reactions prominent at night (purple reaction lines). Δ indicates reservoir compounds that are thermally unstable. Stratosphere downwelling, a non-emission source of HNO_3 and NO_2 to the upper troposphere, is not shown.

NO and NO_2 cycle rapidly during the daytime, achieving photo-stationary steady state that is a dynamic equilibrium under continuous sunlight where the rates of their interconversion are balanced, maintaining constant concentrations over time. The NO is oxidised mostly by O_3 to produce NO_2 (R1). The other less prominent oxidants on a global scale, that convert NO to NO_2 include hydroperoxyl radical (HO_2) and organic peroxy radicals (RO_2) (Brasseur& Jacob, 2017). NO_2 is photolyzed to regenerate NO and produce odd oxygen which then promptly reacts with O_2 (R2). At photo-stationary state, the rate of NO_2 photolysis equals the rate of NO oxidation by ozone, HO_2 and RO_2, leading to a steady ratio of NO_2 to NO concentrations.

RO_2 and HO_2 are not directly emitted but form in the atmosphere through reactions between volatile organic compounds (VOCs) and oxidants such as OH, ozone (O_3), or nitrate radicals (NO_3). During the day, OH radicals oxidize VOCs to create RO_2 radicals, while HO_2 arises from reactions like CO oxidation or RO_2 decomposition. At night, NO_3 radicals become important oxidants for generating RO_2 and HO_2 (Brasseur& Jacob, 2017).

Reaction (R1) to (R2) is a null cycle for O_3, as O_3 consumed in (R1) is regenerated in (R2). When HO_2 competes with O_3 to react with NO in (R3) instead of O_3 in (R1) and this is followed by (R2), there is net generation of O_3. Similarly, reaction of NO with RO_2 leads to net production of O_3. Reaction (R3) also generates OH radicals that determines the oxidizing capacity of the atmosphere.

$$NO + O_3 \longrightarrow NO_2 + O_2 \quad \text{(R1)}$$

$$NO_2 + h\nu\ (\lambda < 400\ \text{nm}) \xrightarrow{O_2} NO + O_3 \quad \text{(R2)}$$

$$HO_2 + NO \longrightarrow OH + NO_2 \quad \text{(R3)}$$

NO_x reacts in the troposphere to form oxidized nitrogen compounds that are temporary NO_x reservoirs. For NO_2, these include HNO_3 from reaction with OH, peroxyacyl nitrates (PANs, formula: $RC(O)O_2NO_2$) from reaction with peroxy acyl radicals ($RC(O)O_2$), peroxynitric acid (HNO_4) from reaction with the HO_2, and methyl peroxy nitrate (MPN, formula: $CH_3O_2NO_2$) from reaction with the methyl peroxy radical (CH_3O_2). HNO_3 uptake by pre-existing aerosols forms aerosol nitrate (pNO_3) (Schneider et al., 2017). NO_y components that are more prominent at night are the nitrate radical (NO_3) formed from reaction of NO_x with O_3, and dinitrogen pentoxide (N_2O_5) from reaction of NO_3 with NO_2. During the daytime, NO_3 is rapidly photolyzed back to NO_2 with a lifetime of less than a minute, as a result, N_2O_5 is predominantly abundant at night. Reservoir compounds formed from NO include alkyl nitrates (ALKNs, formula: $RONO_2$) from reaction with non-acyl peroxy radicals (RO_2), and HONO from reaction with OH. At night, HONO accumulates, but during the day HONO is very short-lived, as it undergoes rapid photolysis back to NO and OH.

Table 1.1 presents various PANs species along with their molecular formulas and chemical structures. The most abundant PANs compound is PAN. Many other PAN-type compounds include peroxypropionyl nitrate (PPN), peroxyacryloyl nitrate (APAN), peroxymethacryloyl nitrate (MPAN), peroxyisobutyryl nitrate (PiBN), peroxy-n-butyryl nitrate (PnBN) and peroxybenzoyl nitrate (PBzN) (Slusher et al., 2004; Zheng et al., 2011).

Table 1.1: Chemical Formulas and Structures of PAN-type Compounds

PANs Species	Formula	Chemical Structure
PAN	$CH_3C(O)O_2NO_2$	$CH_3–C(=O)–O–O–NO_2$
PPN	$CH_3CH_2C(O)O_2NO_2$	$CH_3–CH_2–C(=O)–O–O–NO_2$
APAN	$CH_2CHC(O)OONO_2$	$CH_2=CH–C(=O)–O–O–NO_2$
MPAN	$CH_2=C(CH_3)C(O)O_2NO_2$	$CH_2=C(CH_3)–C(=O)–O–O–NO_2$
PiBN	$(CH_3)_2CHC(O)OONO_2$	$(CH_3)_2CH–C(=O)–O–O–NO_2$
PnBN	$CH_3(CH_2)_2C(O)OONO_2$	$CH_3–CH_2–CH_2–C(=O)–O–O–NO_2$
PBzN	$C_6H_5C(O)OONO_2$	$C_6H_5–C(=O)–O–O–NO_2$

Recycling of reservoir compounds back to NO_x is by photolysis for almost all reservoir compounds and by thermal decomposition for the thermally labile peroxy nitrates (PNs) family compounds: PANs, HNO_4, and MPN. This recycling along with NO_y sources to the troposphere sustains tropospheric NO_x concentrations at < 35 pptv over the remote ocean and 60-380 pptv over polluted landmasses (Shah et al., 2023; Marais et al., 2018; Horner et al., 2024). Stable NO_x reservoir compounds are transported long distances in the remote, cold upper layers of the troposphere, before subsiding and decomposing on warming (Zhai et al., 2024). This process supplies other parts of the world with oxidants (HO_x) and O_3 precursors (NO_x and RO_2) (Zhai et al., 2024).

Processes that remove NO_y species from troposphere permanently occur through wet and dry deposition, which transfer NO_y from the atmosphere to Earth’s surface. Wet deposition occurs via precipitation such as rain, snow or cloud water carrying dissolved nitrogen compounds like HNO_3. This process tends to dominate in regions with high rainfall. Dry deposition is the direct settling of nitrogen gases (e.g., NO, NO_2) and particles such as pNO_3 onto surfaces without precipitation. This plays a major role in arid and polluted regions such urban and industrial areas (Fowler et al., 2013).

In the troposphere, NO_y has a lifetime of less than one day in the planetary boundary layer that is the lowest part of the atmosphere and is directly influenced by Earth's surface. This short lifetime is due to rapid removal processes such as dry and wet deposition, as well as high turbulence and mixing that facilitate quick dispersion and reactive radicals, especially hydroxyl radicals, drive photochemical reactions that break down NO_y quickly in this layer. NO_y has a longer lifetime of 10–20 days in the cold upper troposphere. This is because lower concentrations of radicals slow chemical degradation, reduced turbulence limits mixing, and colder temperatures slow down reaction rates. Furthermore, transport processes, including stratosphere–troposphere exchange, can lead to the accumulation of NO_y in this region. (Logan, 1983; Prather& Jacob, 1997).

NO_x has a lifetime of about a week in the cold upper troposphere compared to less than a day in the boundary layer (<2 km), because lower concentrations of radicals and stable cold atmospheric conditions allow NO_x to persist longer in the UT, while in the boundary layer, rapid photochemical reactions, deposition processes, high turbulence, and the presence of abundant volatile organic compounds enhance its removal (Shah et al., 2020; Jaeglé et al., 1998). The lifetimes of NO_x reservoir compounds cover a wide range, depending on their thermal stability. The lifetime of PAN, for example, has exponential dependence on temperature, ranging from one hour at 295 K in the relatively warm planetary boundary layer, to months at 250 K typical of the cold upper troposphere (Jordan et al., 2020). Similarly, the lifetime of HNO_4 ranges from ~20 seconds to 8 hours. MPN is least stable and has a reported lifetimes of a few minutes to hours under warm conditions (Trainer et al., 1991) to several days to weeks under cold conditions (Nault et al., 2015). $RONO_2$ compounds are more thermally stable than PNs family and the lifetimes are mainly dependent on the photolysis rates that vary with season because of the available solar flux (Talukdar et al., 1997; Worton et al., 2010).

1.2 In Situ and Remote Sensing Measurements of Reactive Nitrogen

The measurements of reactive nitrogen concentrations are made in situ, when air is drawn into an instrument, or remotely, when the instrument records a spectroscopic signal integrated over an atmospheric line of sight. Figure 1.2 shows the in-situ instruments that observe many reactive nitrogen species. The chemiluminescence (CL) instrument has been frequently used for both ground-based and airborne in-situ measurements of NO, NO_2 and NO_y. It uses the CL detection of NO with O_3 added as reagent gas (Ryerson et al., 2000; Pollack et al., 2010; Bourgeois et al., 2022). The signal is generated by the emission of photons during the reaction between NO and O_3 forming electronically excited NO_2 that relaxes to its ground state by emitting photons. These photons are detected by a photomultiplier tube and their intensity is proportional to the NO concentration, allowing for the measurement of NO, NO_2, and NO_y. These are measured on three independent channels of the instrument. The NO channel measures NO, the NO_2 channel measures the sum of NO and photolyzed NO_2 via a photolytic converter as NO, and the NO_y channel measures total reactive oxidized nitrogen reduced to NO through a heated gold catalyst with CO. NO_2 is determined from the difference between signals from the NO and NO_2 channels. Research-grade instruments deployed on aircraft for field campaigns are continuously upgraded and improved to improve the accuracy and precision of the instrument, even measurement techniques as established as CL. The estimated uncertainty for the most recent version of the National Oceanic and Atmospheric Administration (NOAA) NOyO3 CL instrument is ±(4 % + 6 pptv) for NO, ±(7 % + 20 pptv) for NO_2, and ±(12 % + 15 pptv) for NO_y (Bourgeois et al., 2022).

NO_2 can also be measured using a Laser Induced Fluorescence (LIF) instrument, because NO_2 strongly absorbs ultraviolet (UV) light and emits fluorescence that can be analysed to determine its concentration. The widely used Thermal–Dissociation LIF (TD-LIF) instrument measures NO_2, HNO_3, total ALKNs ($RONO_2$), total PNs and MPN based on the differences in thermal dissociation temperatures of the reservoir compounds. The air is drawn into an inlet and then directed through five dissociation heaters set at different temperatures to break down specific compounds: HNO_3 + ALKNs + PNs (650°C), ALKNs + PNs (400°C), PNs (200°C), MPN (60°C) and NO_2 (unheated, 15–25°C). The NO_2 produced by the 5 separate channels fluoresces after being excited by a UV laser. The strength of the fluorescence signal is then used to quantify the relative concentration of NO_2 in each sample cell. The difference between higher temperature samples and the lower temperature samples is used to determine HNO_3, ALKNs, PNs and MPN concentrations. The TD-LIF uncertainty is estimated to be 5% for NO_2, 15% for ALKNs and HNO_3, 10% for PNs and 40% for MPN (Wooldridge et al., 2010; Nault et al., 2015).

Even though the reported uncertainties in CL and TD-LIF instruments are relatively low, both instrument measurements of NO_2 are susceptible to biases. This is because of interference (additional NO_2) from thermal decomposition of the least stable NO_x reservoirs, HNO_4 (HO–O–NO_2) and MPN. The TD-LIF measurements of NO_2 in the upper troposphere have 5% interference from HNO_4 and 21%–40% from MPN (Nault et al., 2015). The interference in the UT NO_2 of CL measurements is estimated to be 30%–40% for HNO_4 and 100% for MPN (Bourgeois et al., 2022). The larger interference from HNO_4 and MPN for CL instruments than for TD-LIF instruments is because the higher temperature of the cell and longer residence time of air in the cell promote more efficient decomposition of these compounds (Bourgeois et al., 2022).

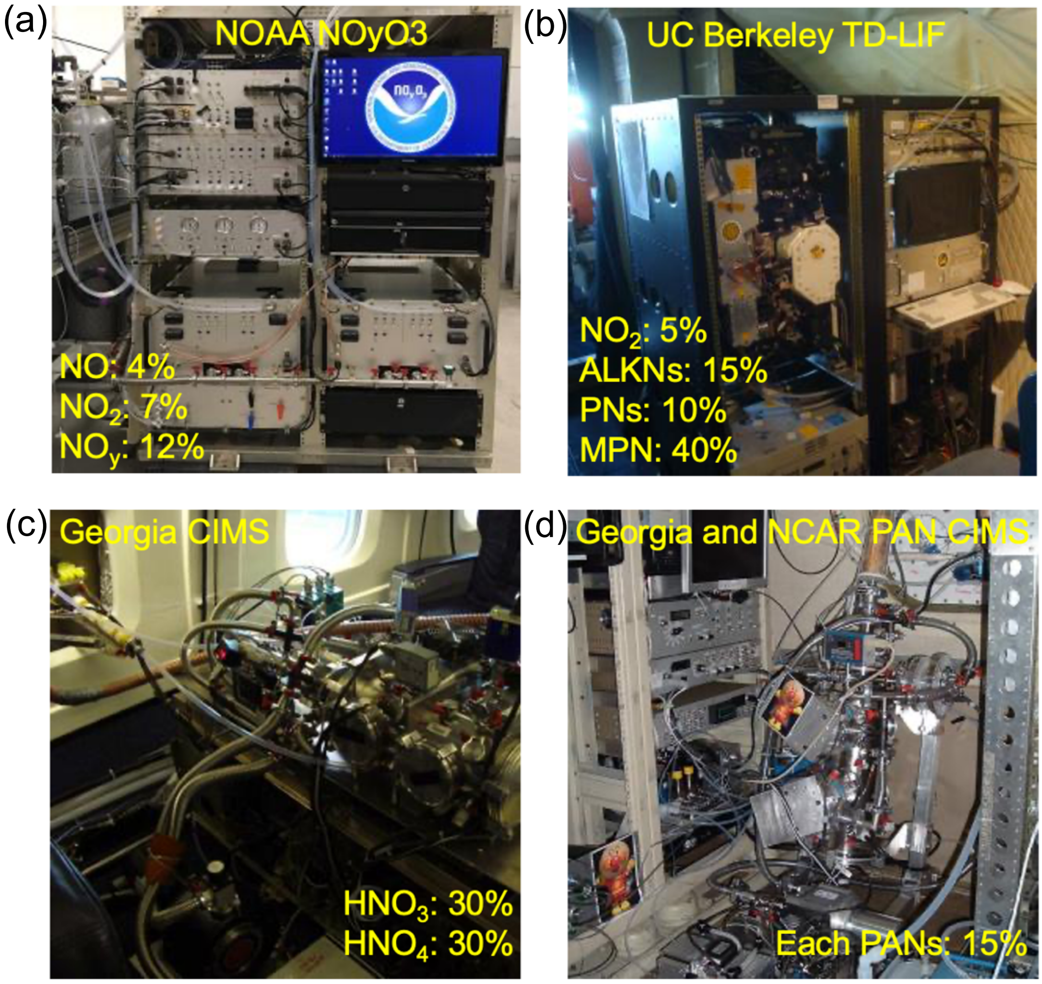

Figure 1. 2: In situ instruments for reactive nitrogen compounds. Adapted from images of DC8 payload from the NASA website (URLs:

(a) https://espo.nasa.gov/spade/instrument/PAN_CIMS_Instrument_by_Georgia_Tech_and_NCAR
(b) https://espo.nasa.gov/instrument/NOAA_Nitrogen_Oxides_and_Ozone
(c) https://airbornescience.nasa.gov/instrument/Thermal-Dissociation_Laser_Induced_Fluorescence
(d) https://airbornescience.nasa.gov/instrument/Chemical_Ionization_Mass_Spectrometer_1

Last access: 25th Feb 2025). Insert percentage values are uncertainties for each compound measured by each instrument. The four instruments shown are the NOAA NOyO3 CL instrument (a), the UC Berkeley TD-LIF (b), the Georgia Tech CIMS (c), and the PAN CIMS co-developed by Georgia Tech and NCAR (d).

The most widely used instruments for HNO_3 are based on chemical ionization mass spectrometry (CIMS). CIMS is a highly sensitive and selective technique for ambient measurements of atmospheric trace gases (Huey, 2007). The CIMS instruments use injected reagent ions (e.g., SiF_5^-, SF_6^-, I^-) to react with target molecules in air samples to form distinct product ions. These ions are separated based on their mass-to-charge ratios measured by a mass spectrometer. The number of these ions are counted by the ion detector and used to quantify ambient concentrations (Huey, 2007). The HNO_3 NOAA CIMS instruments used in both ground-based and aircraft campaigns uses SiF_5^- reagent ions and achieves a measurement uncertainty is 10% (Neuman et al., 2002; Neuman et al., 2000). The single mass analyser California Institute of Technology (CalTech) CIMS uses CF_3O^- reagent ions to measure both HNO_3 and HNO_4 with uncertainties of 30% for HNO_3 and 35% for HNO_4 (Crounse et al., 2006; Allen et al., 2021). A third CIMS developed by the Georgia Institute of Technology (Georgia Tech) uses SF_6^- reagent ions to also measure both HNO_3 and HNO_4 and has an estimated uncertainty of 30% for each (Huey, 2007; Kim et al., 2007).

A TD-CIMS method, utilizing I^- as a reagent ion was developed to detect multiple PANs (Slusher et al., 2004). The TD-CIMS is a modified CIMS that includes a heated chamber to dissociate thermally labile PANs into RO_2 that then react with I^- ions. The mass spectrometer detects the corresponding carboxylate ions (Slusher et al., 2004; Zheng et al., 2011). For example: PAN thermally dissociates in the inlet to form $CH_3C(O)O_2$ and NO_2. The $CH_3C(O)O_2$ reacts with I^- to form $CH_3C(O)O^-$ and IO (Villalta& Howard, 1996). The carboxylate ion such as $CH_3C(O)O^-$ forms stronger bonds with water than does I^- and the carboxylate ion is detected as the signal for PAN concentrations (Villalta& Howard, 1996). Other PAN-type species are detected in a similar manner. The PAN species that are measured include PAN, PPN, PiBN, PnBN, PBzN, APAN and MPAN with the same ~15% uncertainty (Slusher et al., 2004; Zheng et al., 2011). N_2O_5 and NO_3 can be measured with the same TD-CIMS instrument using I^- ions. Both N_2O_5 and NO_3 are detected as NO_3^-. N_2O_5 forms NO_2 and NO_3 upon thermal dissociation in the inlet. Once the NO_3 enters the flow tube, I^- charge transfers it to form NO_3^- (Davidson et al., 1977). N_2O_5 also reacts directly with I− to form NO_3^- (Huey et al., 1995). PAN is also measured with the so-called PAN and Trace Hydrohalocarbon Experiment (PANTHER) instrument that uses gas chromatography with electron capture detection (Flocke et al., 2005).

The C1-C5 ALKNs are collected with Whole Air Samplers (WAS) during the flight campaign and analysed later in the laboratory using gas chromatography with flame ionization and atomic emission (Blake et al., 2003). These ALKNs are methyl, ethyl, propyl, butyl, and pentyl nitrates.

The in-situ instruments have been deployed to many platforms, such as static ground-based stations, and mobile platforms such as vehicles, ships and aircraft. The prominent mobile platform of relevance to this thesis is research and commercial aircraft. Research aircraft offer the advantage of flexibility in mission planning, allowing targeted observations of atmospheric phenomena in specific regions. They can be equipped with specialized instrumentation to measure a wide range of meteorological, chemical, and physical properties, providing high-resolution, high-accuracy datasets. Research aircraft can operate at a range of altitudes, from the boundary layer to the upper troposphere and lower stratosphere, depending on the altitude ceiling of the aircraft. This enables studies of atmospheric composition and dynamics in regions that are otherwise difficult to access, such as global upper troposphere. The research aircraft campaigns enable concurrent measurements of a wide range of various compositions but limited to spatial and temporal coverages. Commercial aircrafts provide a complementary dataset by offering continuous, long-term observations over a broad spatial scale. But since commercial aircraft usually carry one container for instruments, the number of instruments and thus the variations of compositions that can be measured are limited.

Like the in situ LIF technique, remote sensing takes advantage of absorption of UV-visible light by NO_2. Remote sensing instruments measure solar backscattered radiation and use the wavelength range 405-465 nm to detect NO_2 (Van Geffen et al., 2015). There have been instruments in space measuring NO_2 since 1996 starting with The Global Ozone Monitoring

Experiment (GOME) launched by the European Space Agency (ESA) and more recently the Ozone Monitoring Instrument (OMI) (Levelt et al., 2006) launched by National Aeronautics and Space Administration (NASA) in July 2004 and the TROPOspheric Monitoring Instrument (TROPOMI) launched by ESA in October 2017 (Griffin et al., 2019; Lamsal et al., 2021; van Geffen et al., 2020; Goldberg et al., 2021a; Levelt et al., 2018).

Figure 1.3 shows the light paths measured by space-based UV-visible instruments measuring solar backscattered radiation. The retrieval of NO_2 from satellite observations involves three main steps. The first step is an NO_2 slant column density (SCD) retrieval using a differential optical absorption spectroscopy (DOAS) technique, which provides the total amount of NO_2 along the effective light path from sun through atmosphere to the satellite. Next, a model and assimilated data are used to calculate the stratospheric component of NO_2 SCD and remove it to isolate the tropospheric component. And finally, the isolated tropospheric SCDs are converted to vertical tropospheric column densities using an air mass factors (AMFs) (van Geffen et al., 2020). The AMF also includes information about the viewing geometry from the sun to the sensor, absorption and scattering by trace gases, aerosols and clouds along the viewing path, and the reflectivity of the surface of the Earth (Palmer et al., 2001). The accuracy of these retrievals depends on the precision of the AMFs (Verhoelst et al., 2021; Hong et al., 2017). The estimated uncertainty contribution of the AMF is ~50%, largely due to error contributions from clouds (Beirle et al., 2011; Goldberg et al., 2021b).

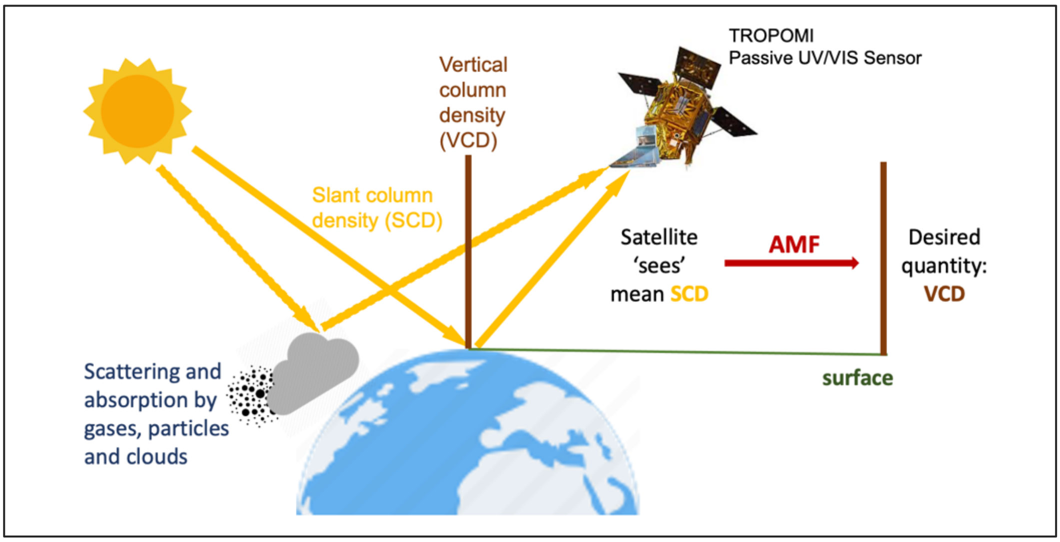

Figure 1. 3: Light path measured by space-based UV-visible instruments for the detection of NO_2.

1.3 Bottom-up and Top-down Emissions Estimates of Reactive Nitrogen

Emission inventories that document the emissions of primary reactive nitrogen compounds, such as NO_x, from a wide range of natural and anthropogenic sources at global, regional, and local scales are essential for chemical transport models. These inventories aid in interpreting air pollutant concentration distributions, understanding their spatial and temporal variations, and formulating well-informed policy recommendations. Emission estimation primarily relies on two methodologies: bottom-up and top-down approaches (Brasseur& Jacob, 2017).

The bottom-up method estimates emissions by compiling data based on activity rates and emission factors across different sectors. It calculates emissions as the product of the two. Activity factors provide information like the amount of fuel or energy consumed, the distance travelled by a car, ship or aircraft, or the amount of a particular product produced. The emission factor is then the rate of production of a primary air pollutant per unit of activity (Fung et al., 2023). Scaling factors can also be applied to account for local variations, such as meteorological conditions, surface properties, weekday/weekend effects, and variability at finer time scales (hourly) than the available activity data (monthly/annual) (Brasseur& Jacob, 2017). For example, NO_x emissions from a power plant are calculated by multiplying the annual fuel consumption (activity rate), the amount of NO_x emitted per unit of fuel burned of the power plant (emission factor), and a seasonal scaling factor that adjusts for variations in power demand due to seasonal energy requirements.

This method can provide detailed insights into specific sectors, such as transportation or industrial processes, by utilizing localized data (Zhang et al., 2018; Li et al., 2018), but it is often hampered by significant uncertainties, particularly in complex urban environments where vehicle emissions can vary widely based on operational conditions (Palacios et al., 2001; Cifuentes et al., 2021). It often suffers from the challenge of data availability and quality, as it requires accurate and timely information on activity rates and emission factors, which can be difficult to obtain, especially in rapidly developing regions. The emissions factors could be not representative of local conditions and in the low time resolution but broad assumptions about finer time resolution variability are required (Itahashi et al., 2019; Zhang et al., 2007).

The top-down approach uses observations to determine emissions from a source by measuring and/or modelling changes in atmospheric concentrations in the proximity to the source. This approach can be particularly useful in regions undergoing rapid changes in economic activity or regulatory environments, as it offers more current data than is available to construct bottom-up emission inventories (Elguindi et al., 2020; Daniels et al., 2023). These top-down approaches include inverse modelling that scales bottom-up emissions in the modelling to match the modelled NO_x abundances to the observations (Konovalov et al., 2006). These model-based top-down approaches necessitate prior knowledge of the NO_x lifetime (τ), which is primarily determined during daytime by the reaction between NO_2 and the OH, resulting in the formation of HNO_3 (Section 1.1) (Spicer, 1982). The NO_x lifetime (τ) can be derived from atmospheric chemistry models, either directly through explicit modelling or indirectly using inverse modelling techniques.

However, the accuracy of these emission estimates is inherently constrained by the models' ability to accurately simulate OH concentrations. This limitation is particularly pronounced in megacities, where highly nonlinear and small-scale chemical interactions present significant challenges to reliable modelling (Spicer, 1982) .

Figure 1.4 shows the basic pathway of top-down estimate of NO_x emissions from satellite column densities of NO_2. Observations are converted to emissions using a simple mass balance approach that uses the modelled ratio of columns densities to emissions from chemical transport models to convert NO_2 tropospheric columns densities to surface emissions of NO_x (Leue et al., 2001; Martin et al., 2003). The approach works, as NO_x has a relatively short lifetime (2-6 hours) at or near sources, so the NO_x concentrations would centre at the source point and would not be transported away from the source (Leue et al., 2001). This is suitable for estimating gridded emissions at scales suitable for compounds that persist for 2-6 hours, but it requires a computationally expensive chemical transport model for the conversion.

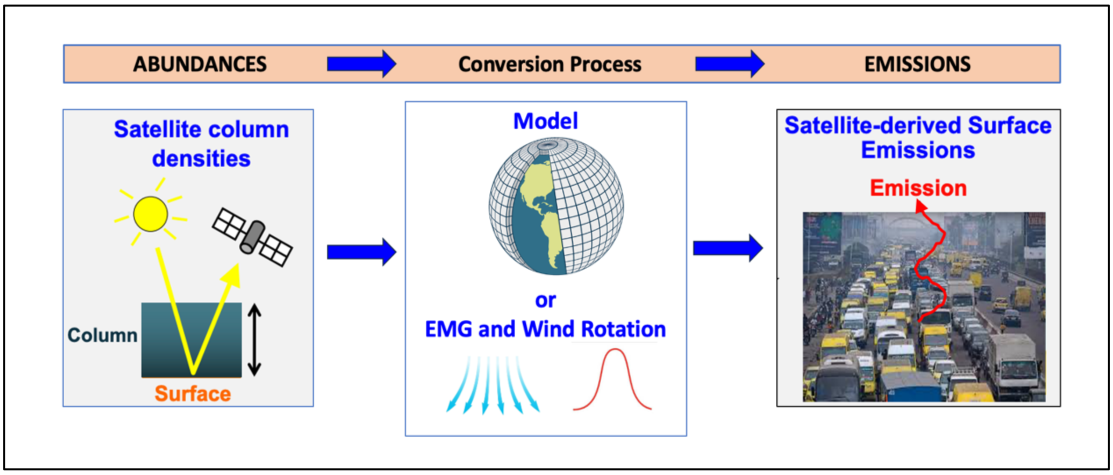

Figure 1. 4: The illustration of top-down approach of NO_x emissions estimates.

Beirle et al. (2011) firstly introduced a top-down method without the need for resource-intensive models that stead, can be applied directly to isolated NO_2 hotspots observed by satellite instruments measuring tropospheric NO_2

column densities (Section 1.2). Such hotspots correspond to large point sources of NO_x, including large urban areas, industrial complexes, and fossil-fuelled power plants. The top-down method proceeds in two main steps. First, individual satellite pixels around a source are rotated according to the local wind direction so that all pixels are aligned with a common north–south axis. This procedure, known as the wind-rotation method (Fioletov et al., 2015), preserves the relative position of each pixel with respect to the source: the distance from the source ($r = \sqrt{x^2 + y^2}$) remains unchanged, as does the upwind/downwind relationship. The rotation ensures that pixels from multiple days with varying wind directions can be combined into a single, coherent, gridded plume. Importantly, the measured NO_2 values are not altered by this rotation. A schematic of this procedure is illustrated in Figure 1.5.

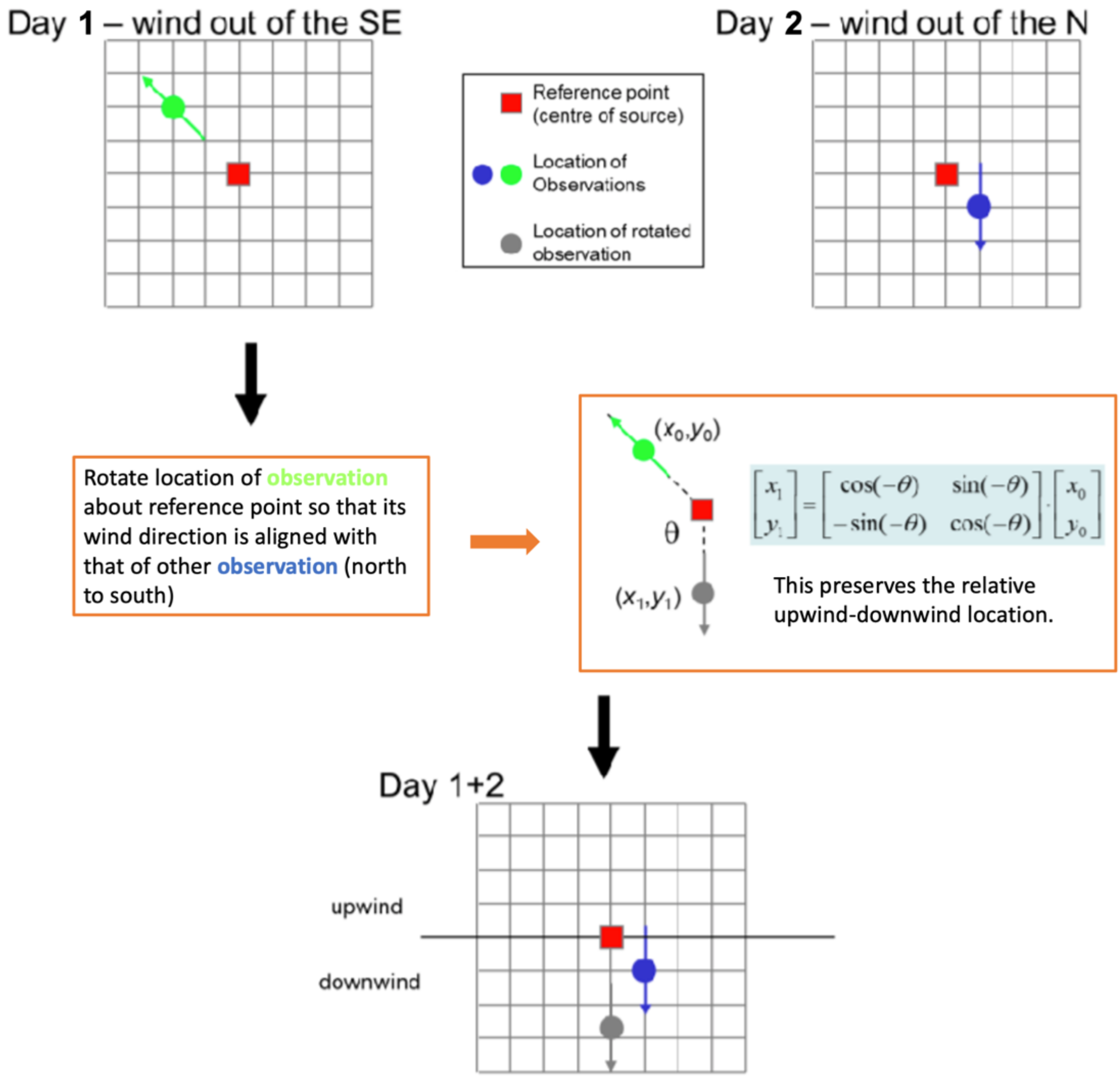

Rotate location of observation about reference point so that its wind direction is aligned with that of other observation (north to south)

$$\begin{bmatrix}x_1\\ y_1\end{bmatrix}=\begin{bmatrix}\cos(-\theta) & \sin(-\theta)\\ -\sin(-\theta) & \cos(-\theta)\end{bmatrix}\cdot\begin{bmatrix}x_0\\ y_0\end{bmatrix}$$

This preserves the relative upwind-downwind location.

Figure 1. 5: Schematic illustration of the wind-rotation method, adapted from (Fioletov et al., 2015). To preserve the relative upwind–downwind positions of the observations, each pixel is rotated by an angle of −θ, where θ is the wind direction, around the emission source. This rotation aligns all wind vectors to a common direction, so that the effective wind direction for all observations is standardized as blowing from the north to the south.

Once the rotated plume is constructed, a mathematical function is fit to the observed NO_2 distribution. This function captures both the Gaussian cross-plume shape and the exponential decay of NO_2 concentrations along the downwind axis. The function, known as an Exponentially Modified Gaussian (EMG), yields parameters that can be used to estimate NO_x emissions. The fitted plume width provides information on atmospheric dispersion, while the exponential decay length gives the effective atmospheric lifetime of NO_2, representing the combined effect of chemical and physical loss. The amplitude of the fitted function corresponds to the peak enhancement of NO_2 above background near the source, and therefore reflects the strength of the emission plume. By jointly analysing the amplitude and the decay of the plume, the method retrieves both the emission rate at the source and the effective lifetime of the pollutant (Beirle et al., 2011; Valin et al., 2013). Details of the EMG fitting, and its implementation are described in Chapter 2, Section 2.2.1.

This wind rotation and EMG fit method has been applied to satellite observations that resolve isolated urban, industrial and power plant hotspots predominantly in the US, worldwide (de Foy et al., 2014; Goldberg et al., 2019b; Lu et al., 2015; Goldberg et al., 2021b), in western Europe (Pope et al., 2022; Lorente et al., 2019), China (Wu et al., 2021a), the US (Goldberg et al., 2019a), as well as to investigate changes in NO_x emissions due to COVID-19 lockdown measures in the New York Metropolitan Area (Tzortziou et al., 2022) and for select cities worldwide (Lange et al., 2022).

1.4 Chemical Transport Modelling of Reactive Nitrogen

The bottom-up emission inventories detailed in Section 1.3 are input to chemical transport models to simulate ambient concentrations for a range of applications, such as air pollutant concentration estimates, to test current understanding of atmospheric composition, for AMFs needed to retrieve satellite observations (Section 1.2), and to interpret the causes for air quality degradation, amongst others. Figure 1.6 shows the general layout of the 3D chemical transport model, GEOS-Chem. GEOS-Chem is driven with offline meteorological input generated with the Goddard Earth Observing System (GEOS) from the NASA Global Modelling and Assimilation Office (GMAO) (Bey et al., 2001). The model is on a fixed latitude-longitude (cartesian) grid and has 47 terrain-following vertical layers extending from the surface of the Earth to 0.01 hPa. The meteorology data includes Goddard Earth Observing System Forward Processing (GEOS-FP) for 2012-present that has a high horizontal resolution of 0.25° latitude x 0.3125° longitude with 72 vertical levels and Modern-Era Retrospective Analysis for Research and Applications (MERRA-2) reanalysis product. MERRA-2 is used to achieve consistency in simulations from 1979 (the start of the satellite record of meteorology) to the present day, but it is at coarser horizontal resolution (0.5° x 0.625°) than GEOS-FP.

In addition to the reactive nitrogen sources detailed in Section 1.1, the model includes many other natural and anthropogenic primary air pollutant emissions that are gridded from the emission inventory resolution to the model resolution and have temporal and environmental scaling factors applied using the Harmonized Emissions Component (HEMCO) emissions package (Keller et al., 2014).

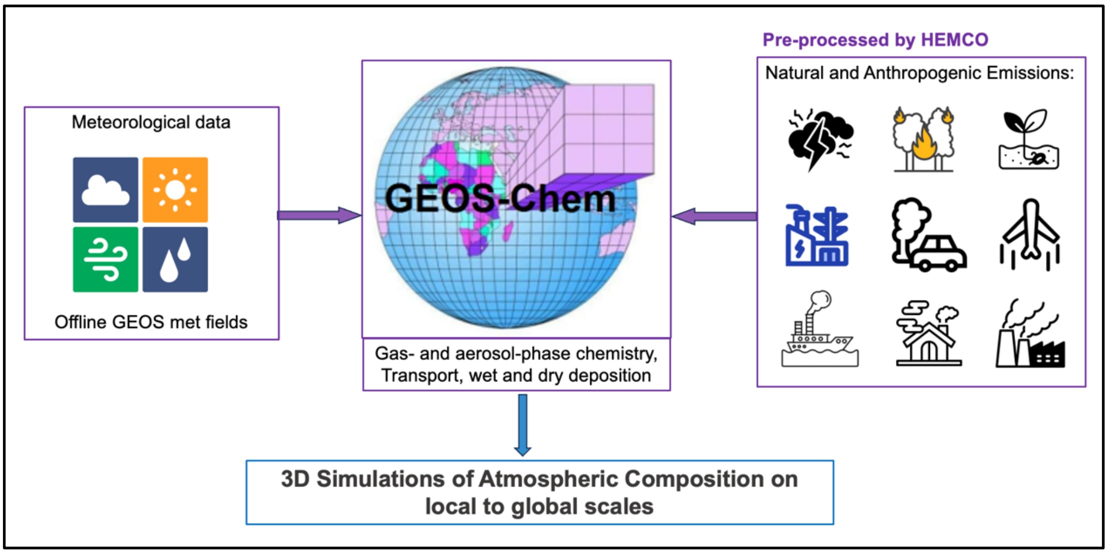

Figure 1. 6: General schematic of the overall structure of a 3D chemical transport model such as GEOS-Chem that uses offline meteorology.

GEOS-Chem simulates detailed gas- and aerosol-phase chemistry in the troposphere and stratosphere. This is achieved with a chemical solver that, for GEOS-Chem, is the Kinetic PreProcessor (KPP) (Lin et al., 2023). This code contains files that specify the chemical compounds, chemical reaction mechanisms, and reaction rates. It covers nearly all reactive nitrogen species shown in Figure 1.1, except that only a subset of PANs is represented. These PANs in the model are PAN, PPN, and MPAN. Chemical mechanism kinetics in GEOS-Chem generally follow JPL/IUPAC recommendations (Bates et al., 2024).

The transport in GEOS-Chem include the advection that is computed using the advection algorithm of Lin and Rood (1996) on the latitude-longitude grid of the meteorological data, convective transport that is computed from the convective mass fluxes in the meteorological archive as described by Wu et al. (2007) and boundary layer mixing that uses the non-local scheme implemented by Lin and McElroy (2010). Dry deposition in GEOS-Chem is represented by the resistance-in-series scheme, where deposition velocity is determined by the sum of aerodynamic resistance (Ra), quasi-laminar boundary layer resistance (Rb), and canopy/surface resistance (Rc) (Wesely, 1989). Ra is common to all species and depends on meteorological factors such as wind speed, turbulence, and surface roughness. Rb and Rc are species-specific: Rb is controlled by molecular diffusivity, while Rc depends on vegetation type, stomatal conductance, and the chemical/physical properties of each species, particularly solubility and surface reactivity (Wang et al., 1998; Wesely, 1989). Highly soluble and reactive species like HNO_3 deposit rapidly, whereas more volatile and less soluble species such as PANs have slower deposition rates. Aerosol nitrogen uses a size-dependent scheme accounting for gravitational settling and hygroscopic growth (Zhang et al., 2001). Wet deposition parameterizations include the scavenging of soluble species by convective updrafts, rainout and washout from convective anvils, and large-scale precipitation processes (Liu et al., 2001). The efficiency of scavenging depends on each species' solubility, represented through Henry's law constants, and for aerosols, on their particle size and hygroscopic properties (Amos et al., 2012). Wet deposition effectively removes both aerosols and soluble gas HNO_3.

The GEOS-Chem model offers a suite of flexible diagnostics to output concentrations, meteorological fields, emissions, reaction rates, deposition rates, and other simulated or input parameters as 24-hour averages, coincident with low-Earth orbiting satellite overpass times, or sampled at the same time and location as aircraft measurement campaigns. The latter uses the NOAA ObsPack data product (https://gml.noaa.gov/ccgg/obspack/, last accessed September 2022) that, essentially, flies the research aircraft through the model.

1.5 Reactive Oxidized Nitrogen in the Global Upper Troposphere: Importance and Uncertainties

NO_y in the upper troposphere (UT) impacts global climate, surface air quality and the oxidizing capacity of the whole troposphere (Bradshaw et al., 2000; Dahlmann et al., 2011; Mickley et al., 1999; Worden et al., 2011). NO_y is an important climate driver, because tropospheric O_3 production is limited by the availability of NO_x throughout the free troposphere. The effect of O_3 on climate is particularly pronounced in the upper troposphere, where the radiative forcing efficiency (W m^{-2} per unit change in concentration) of O_3 peaks (Dahlmann et al., 2011; Rap et al., 2015; Worden et al., 2011). Influence on tropospheric O_3 production also affects abundance of OH, with already discussed knock-on effects on CH_4, CO, VOCs, and aerosols (Murray et al., 2013; Seltzer et al., 2015; Storelvmo et al., 2019).

The UT extends from as low as 450 hPa (~8 km) near the poles to as high as ~100 hPa (16 km) in the tropics, according to the tropopause height from the NASA GMAO MERRA-2 meteorology, an offline data product that is used as input to GEOS-Chem (Section 1.4). The variability in tropopause height with latitude results from differential heating of the Earth. Warmer at the tropics, cooler at the poles. This causes deeper convection at the Equator, leading to a higher altitude tropopause (Houghton, 2002). Local sources of primary NO_x in the UT include lightning and aircraft (Brasseur et al., 1996; Jacob et al., 1996; Jaeglé et al., 1998; Bertram et al., 2007). Lighting is the dominant source of NO_x to the UT, especially in the tropics (Brasseur et al., 1996; Marais et al., 2018).

The metric O_3 production efficiency (OPE) is routinely used to quantify the efficiency with which NO_x sources produce ozone (Dahlmann et al., 2011). The OPEs of different O_3 sources, obtained with a chemical transport model, are shown in Figure 1.7 (a). The OPE is calculated as the molecules of O_3 produced per molecule of NO_x lost to temporary reservoirs (Section 1.1). The OPE of the UT is much greater than anywhere else in the troposphere due to the persistence (longer lifetime) of NO_y in the cold and dry UT, discussed in Section 1.1. This is why sources abundant in the UT like aircraft and lightning have much greater OPEs than sources at the surface like industry, road traffic, ships, and open burning of biomass.

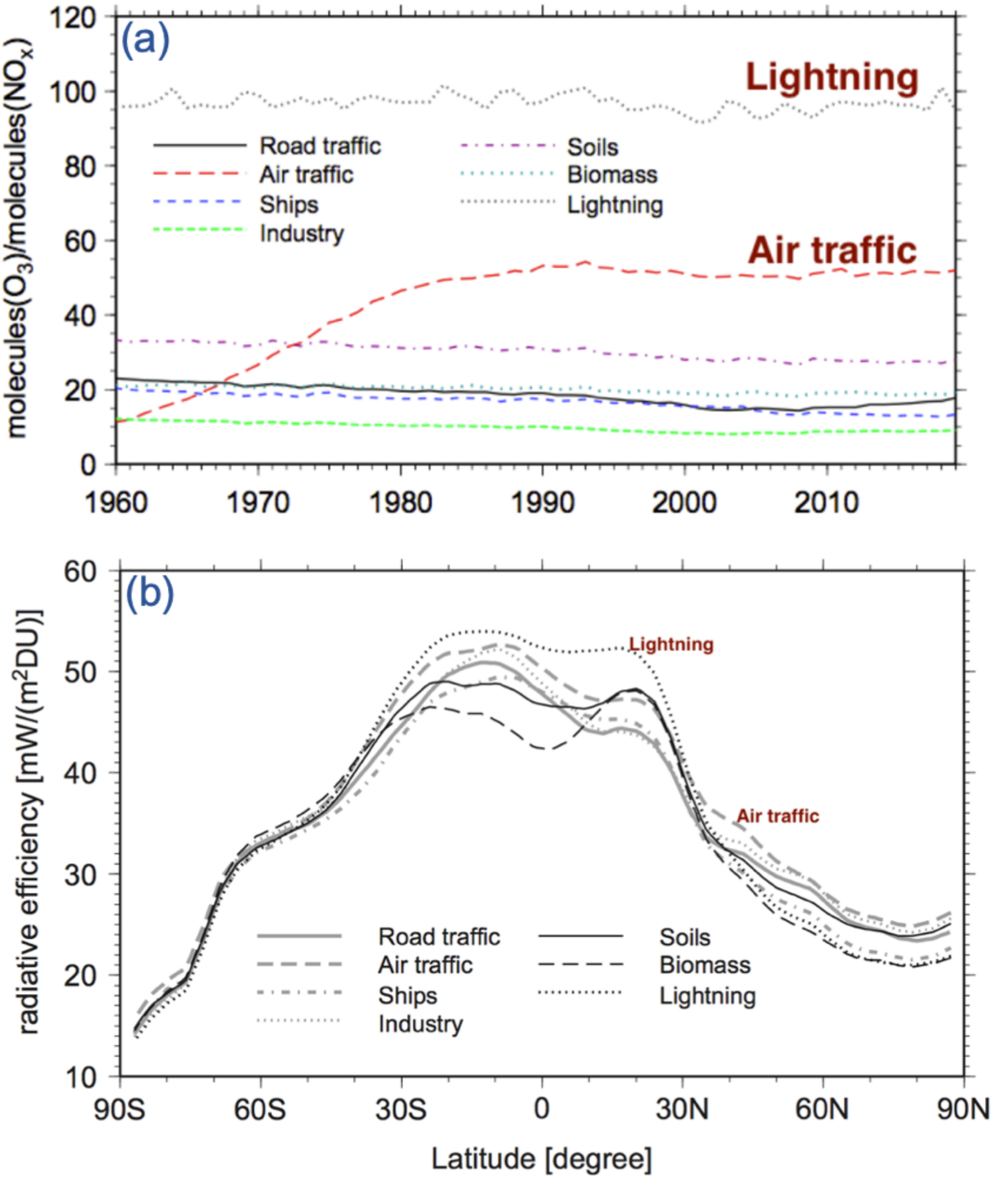

Figure 1. 7: Global mean O_3 production efficiencies (OPEs) from different NOx sources (a) and zonal mean of O_3 radiative efficiency for different sources for 2010-2019 (b). Adapted from Dahlmann et al. (2011). Lines in (a) show time series of the OPE of different sources obtained with a chemical transport model. Values in (b) are given in mW/(m^{2}DU), where DU is Dobson Units (1 DU = 2.69 × 10^{20} molecules/m^2).

O_3 radiative forcing is greatest in the upper troposphere (UT), particularly in the tropics (Dahlmann et al., 2011), as illustrated in Figure 1.7 (b) and consistent with earlier modelling by Mickley et al. (1999). In the UT, abundant incoming solar radiation, colder temperatures, and lower optical thickness combine to enhance the radiative impact of ozone. Ozone strongly absorbs terrestrial longwave radiation in the 9.6 μm band. For this UT region, the earth surface below is much warmer, emitting strong longwave radiation upward, while the colder ozone layer in the UT emits less radiation to space than it absorbs from below, in accordance with the Stefan–Boltzmann law. The resulting imbalance produces a net trapping of heat and thus positive radiative forcing. The lower air density at high altitudes also reduces optical thickness, allowing ozone to influence the Earth–space radiation balance more efficiently than at lower levels (Lacis et al., 1990; Mickley et al., 1999; Aghedo et al., 2011).

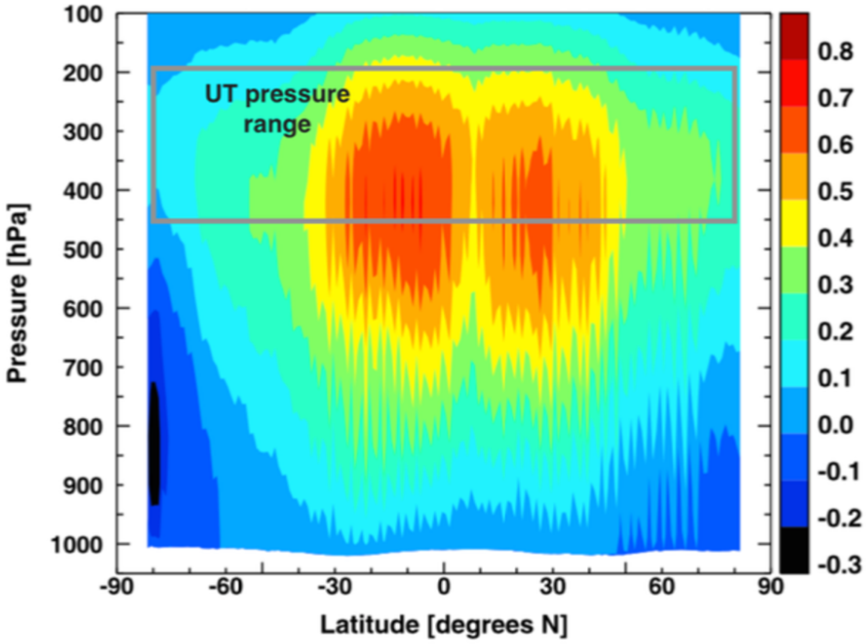

Figure 1. 8: The zonal mean distribution of the O_3 radiative forcing (in mW/m2/ppbv) in August 2006. Adapted from Aghedo et al. (2011) that obtained these estimates using Tropospheric Emission Spectrometer (TES) all-sky instantaneous longwave radiative forcing kernels (sensitivity of longwave radiative forcing response to changes in abundances of tropospheric ozone). The grey box is upper troposphere.

Using data from the Tropospheric Emission Spectrometer (TES) aboard NASA's Aura satellite, Aghedo et al. (2011) found that instantaneous longwave radiative forcing from ozone perturbations is greatest (> 0.5 mW m^{-2} $ppbv^{-1}$) in the free troposphere between 180 hPa and 650 hPa, peaking in the UT, as demonstrated in Figure 1.8. As a result, O_3 formed from NO_x emitted by lightning flashes and aircraft at cruising altitudes has a greater longwave radiative forcing efficiency than O_3 formed from ground-based precursors shown in Figure 1.7 (b).

The impact of NO_y on climate is complex and uncertain. Radiative forcing from NO_y is either positive due to formation of O_3 or it is negative due to formation of OH that decreases abundance of CH_4 (Stratmann et al., 2016; Fuglestvedt, 1999). The net effect might be negative, as the effect of CH_4 is currently understood to outweigh the effect on tropospheric O_3 (IPCC, 2023), but this conclusion is drawn with models with large uncertainties in the sources and chemical and physical processing of UT NO_y.

Knowledge of dominant NO_y compounds, sources, chemistry, fate, and persistence in the UT has been largely informed by observations and models used as part of research and commercial aircraft campaigns (Boersma et al., 2011; Marais et al., 2018; Silvern et al., 2018; Travis et al., 2020; Travis et al., 2016) (Section 1.1). Instruments onboard research aircraft that sample the UT, in particular the recently retired NASA DC-8 platform, have undergone substantial development to directly measure and derive estimates of a large suite of UT NO_y compounds (Section 1.2).

These aircraft campaigns have confirmed that sources of NO_y to the UT are dominated by lightning NO_x emissions (Marais et al., 2018; Levy II et al., 1999; Gressent et al., 2016; Gressent et al., 2014), causing a seasonal maximum in NO_y in summer months and a minimum in winter in parts of the world such as the northern midlatitudes where there is large seasonal variability in lightning activity (Stratmann et al., 2016; Blakeslee et al., 2014). Other NO_y source contributors include NO_x emissions from cruising altitude aircraft (Brasseur et al., 1996), stratospheric downwelling of air masses laden with HNO_3, NO_2 and promoted prompt formation of PANs as discussed in Section 1.1 (Liang et al., 2011; Jacob et al., 2010; Levy II et al., 1980), deep convective uplift of surface pollution (Ehhalt et al., 1992; Jaeglé et al., 1998; Bertram et al., 2007), and aged air masses initially very photochemically active that gradually accumulate MPN from reaction of its precursors in the aged air (Nault et al., 2015).

Chemical cycling of dominant daytime NO_y components in the UT is illustrated in Figure 1.9, essentially showing a subset of Figure 1.1 that are pertinent to the daytime UT. All compound shorthand names used below to describe Figure 1.9 are detailed in Section 1.1. During the day, NO oxidation, mostly about 75% by O_3 (Silvern et al., 2018), is balanced by NO_2 photolysis. PANs in the UT are typically dominated by PAN followed by PPN (Roberts, 1990; Roberts et al., 1998; Roberts et al., 2002; Singh, 1987). Recycling of reservoir compounds back to NO_x is dominated by photolysis, as thermally labile PNs are stable against decomposition in the cold UT. This recycling along with NO_y sources to the UT sustains upper tropospheric NO_x concentrations at ~30 pptv over the remote ocean and ~100 pptv over polluted landmasses (Shah et al., 2023; Marais et al., 2018; Marais et al., 2021). Loss processes in the UT are slow and dominated by subsidence and convection to the middle and lower troposphere. NO_y has a lifetime of 10-20 days and NO_x of about one week in the UT (Logan, 1983; Prather& Jacob, 1997; Jaeglé et al., 1998). NO_3 and N_2O_5 are rapidly photolyzed during daytime in the UT and only abundant during night (Bertram et al., 2009), so are not included in the cycle. HONO would also photolysis away promptly in the UT so is not included.

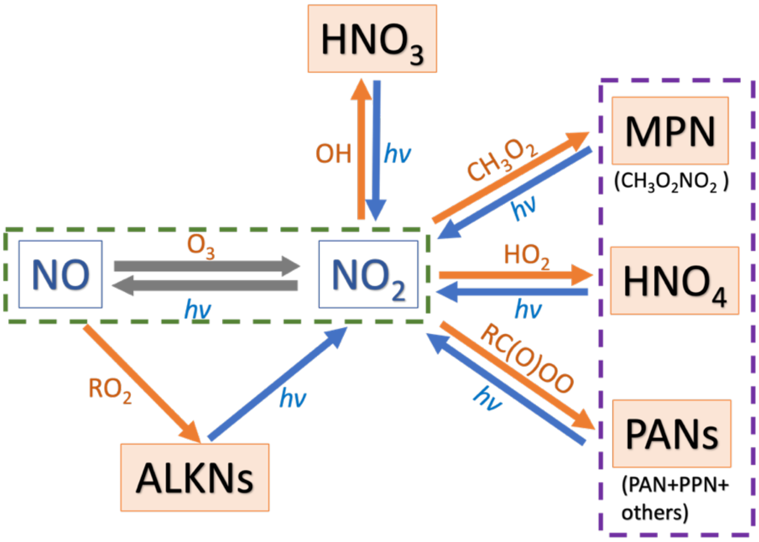

Figure 1. 9: Dominant daytime gas-phase reactive oxidised nitrogen components and reaction pathways in the upper troposphere. Arrow colours distinguish formation (orange) and photolytic (*hv*) decomposition (blue) of reservoir compounds. Dashed boxes indicate compounds of the NO_x family (green) and classed as peroxy nitrates or PNs (purple). "R" in RC(O)OO represents alkyl groups that range in carbon chain length and branching.

Accurate representation of NO_y sources, chemistry, and abundances in Chemical Transport Models (CTMs) is critical for reducing uncertainties in simulating photochemical ozone production and OH concentrations, as the production of OH and ozone is significantly impacted by reactive nitrogen. The large errors in simulated NO_x concentrations therefore lead to significant errors in OH and ozone abundance estimates. It then will impact our understanding of atmospheric chemistry, air quality, and radiative forcing that rely on accurate estimates of these oxidants (Akimoto& Tanimoto, 2021; Paulot et al., 2013; Neuman et al., 2006; Martin et al., 2008; Kanakidou et al., 2016; Geddes& Martin, 2017). Models also provide prior information of the vertical NO_2 distribution that is needed to calculate NO_2 columns from satellite observations. So, errors in modelled vertical NO_2 profiles impart errors in satellite observations that are widely used to understand air pollution abundances and precursor emissions (Martin et al., 2004).

There are large errors of UT NO_y in atmospheric chemistry transport models that represent our best understanding of chemical and physical processes in the atmosphere. Figure 1.10 (a) compares the vertical distribution of modelled and measured NO_x, as well as combined HNO_3 and aerosol nitrates (NO_3^-) from Travis et al. (2016). NO_3^- is concentrated mainly near the surface and constitutes a small fraction of total HNO_3. Measurements are from an aircraft campaign measuring tropospheric composition in August-September 2013 over the Southeast US (Toon et al., 2016). GEOS-Chem Modelled NO_x is underestimated by as much as 400 pptv in the UT but overestimated by 60-70% in the boundary layer. Modelled HNO_3 is overestimated by ~200 pptv in the UT and ~500 pptv in the boundary layer. Travis et al. (2016) decreased surface and lightning NO_x emissions in GEOS-Chem model to correct the 60-70% overestimate of NO_x and HNO_3. This adjustment was informed by wet deposition measurements of reduced nitrogen, which provide constraints on surface NO_x sources. This downscaling addressed the discrepancy in NO_x and HNO_3 in the boundary layer, but worsened the NO_x discrepancy in the UT, where NO_y levels are influenced not only NO_x emissions but also by chemical production, long-range tropospheric transport, and stratospheric downwelling.

Figure 1.10 (b) presents a vertical comparison of measured and modelled NO-to-NO_2 ratios, NO, and NO_2, as reported by Silvern et al. (2018). Their analysis indicates that the NO-to-NO_2 ratio simulated by GEOS-Chem is more than twice the observed values in the UT, suggesting that the photo-stationary steady state of NO and NO_2 assumed in models may not be valid. This leads to a 30% overestimate in satellite observations of tropospheric columns of NO_2 concentrations, due to the greater vertical sensitivity of these instruments to NO_2 in the upper layers of the troposphere (Silvern et al., 2018). To investigate further, they tested the model by decreasing the photolysis rate of NO_2 by 20%. And that improved the agreement between the modelled and measured NO, NO_2, and the NO-to-NO_2 ratio. However, this adjustment also amplified the discrepancy between measured and modelled O_3.

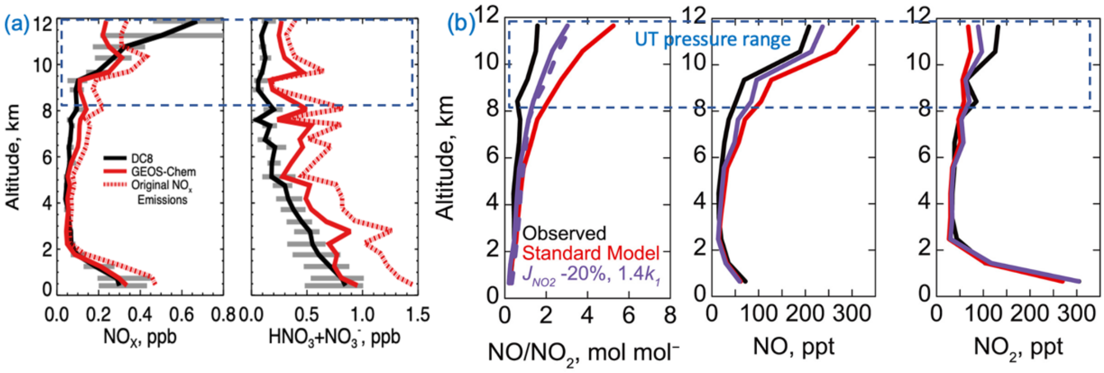

Figure 1. 10: Past studies identifying model biases in NO_y components in the upper troposphere. Panels are large model biases in UT NO_x, combined HNO_3 and aerosol nitrates (a), in UT NO-to-NO_2 ratio, UT NO and NO_2 concentrations (b), The blue dashed boxes show the upper troposphere. In (a), DC8 refers to observations from the NASA DC8 aircraft, dashed red line is GEOS-Chem output with original NO_x emissions, red line is GEOS-Chem output after addressing overestimated lightning and anthropogenic surface NO_x emissions. Adapted from Travis et al. (2016). In (b), aircraft observations are in black, standard GEOS-Chem output in red, and GEOS-Chem with an adjusted NO_2 photolysis in purple. Adapted from Silvern et al. (2018).

A way to quantify the effect of the NO_2 discrepancy on satellite retrievals is by quantifying the AMF (described in Section 1.2). The mean AMF over the southeast US is 1.28 when using vertical distributions from a chemical transport model but is much more (1.67) when using observed vertical NO_2 profiles from an aircraft campaign. The underestimation of the AMF is attributed to the modelled underestimate of UT NO_2. As a result, using model-derived AMFs leads to an ~23% underestimation of tropospheric NO_2 column densities compared to AMFs derived from observations (Lamsal et al., 2014).

In addition to modelling uncertainties, recent studies have shown that in situ NO_2 measurements using CL and TD-LIF instruments are susceptible to interference from decomposition of the least thermally stable NO_x reservoir compounds, HNO_4 and MPN (Section 1.2), that are abundant in the cold upper troposphere (Shah et al., 2023; Ryerson et al., 2000). NO_y from CL instruments can also be biased by decomposition of non-NO_y fixed nitrogen compounds prevalent in the troposphere, such as hydrogen cyanide (HCN) (Bradshaw et al., 1998). The size of the bias in HCN depends on seasonal HCN ambient concentrations (Li et al., 2003; Le Breton et al., 2013).

The modelling studies that have identified stark discrepancies between observed and modelled total NO_y, NO_x, and the ratio of NO-to-NO_2 in the UT have either focused on a few NO_y components, or a single aircraft campaign (Talbot et al., 1999; Lee et al., 2022; Bertram et al., 2007; Huntrieser et al., 2016; Liang et al., 2011; Nault et al., 2015; Fisher et al., 2018; Cohen et al., 2023). A more holistic investigation of all NO_y components is needed, as is advocated by Murray et al. (2021), to reduce uncertainties in knowledge of the current, past, and potential future abundances of tropospheric oxidants. Past studies have also documented the challenges examining measurements made in the UT. These include screening for stratospheric influence, determining the height of the chemical tropopause, and selecting observations and campaigns that are climatologically representative of a standard atmosphere (Barth et al., 2015; Fuelberg et al., 2000; Bertram et al., 2007; Huntrieser et al., 2016; Weinheimer et al., 1994).

1.6 Reactive Nitrogen Precursor Emissions in Under-Sampled Sub-Saharan Africa

Emissions in atmospheric chemical transport models are often a major source of error, particularly for surface and boundary layer concentrations of air pollutants and atmospheric oxidants. These emissions are typically derived from bottom-up inventories (Section 1.3), which for Africa rely on limited local data for activities and region-specific emission factors (Bockarie et al., 2020; Liousse et al., 2014; Keita et al., 2021; Marais& Wiedinmyer, 2016). Key region-specific sources include widespread reliance on diesel and petrol generators for electricity, use of solid fuels, plastics, and dung for cooking, poorly regulated vehicle fleets, limited enforcement of vehicle emissions standards, and the proliferation of motorcycles as a means of navigating congested urban centres (Marais& Wiedinmyer, 2016; Keita et al., 2021).

These bottom-up emissions estimates from reliable, routinely updated, and publicly available regional inventories developed by regulatory agencies are fundamental for models of air quality, climate change and the development of control and mitigation strategies. Such a coordinated effort for reactive nitrogen precursor emissions (NO_x) is absent for Sub-Saharan Africa. Only South Africa has a well-established measurement network collecting data to constrain large point sources of NO_x that are used to build inventories of emissions focused on air quality priority areas (Matandirotya& Burger, 2023). There are some regional inventories for Africa that have been developed by research communities, such as Diffuse and Inefficient Combustion Emissions in Africa (DICE-Africa) (Marais& Wiedinmyer, 2016) and the Dynamics-Aerosol-Chemistry-Cloud Interactions in West Africa (DACCIWA) inventory (Keita et al., 2021), but these are already outdated. The most recent years are 2013 for DICE-Africa and 2015 for DACCIWA. Even though these regional inventories are available for Africa, most chemical transport models use global emission inventories such as the Emissions Database for Global Atmospheric Research (EDGAR) (Crippa et al., 2020), the Hemispheric Transport of Air Pollution (HTAP) (Crippa et al., 2023) and the Community Emissions Data System (CEDS) (Hoesly et al., 2018). There is also an updated version of CEDS developed for the Health Effects Institutes the Global Burden of Disease – Major Air Pollution Sources project ($\text{CEDS}_{\text{GBD-MAPS}}$) (McDuffie et al., 2020) that incorporates DICE-Africa 2013 emissions and extends these to 2017.

Air quality in Sub-Saharan Africa is degrading rapidly (Vohra et al., 2022), due to unprecedented population growth, urbanization, demand for energy, transport, food, and industrial goods, and a dearth of effective regulation (Keita et al., 2021; Adedini, 2022; Lamsal et al., 2013; Liousse et al., 2014). Accurate knowledge of precursor emissions of pollutants is crucial to develop evidence-based regulation needed to mitigate environmental harm (Mukwevho, 2024; Isaxon et al., 2022; Martínez-Alonso, 2023; Bofa, 2024). Only few ground-based monitors are available even in rapid developing South Africa and local data in Sub-Saharan Africa are missing (Garland et al., 2017). Top-down emissions estimates of NO_x, derived from routine satellite observations of tropospheric column densities of NO_2, offer promise (Martínez-Alonso, 2023). Especially relevant to Sub-Saharan Africa are top-down methods that estimate NO_x emissions from emissions hotspots, such as fast-growing urban areas, industrial zones, and power plants (Mukwevho, 2024). NO_x sources in most urban areas in Africa are either already or increasingly dominated by combustion of vehicular fuel, but also include traditional sources like household burning of fuelwood and charcoal (Marais& Wiedinmyer, 2016; Keita et al., 2021). Non-urban hotspots detected with space-based instruments include coal-fired power plants Medupi and Matimba in South Africa close to the border with Botswana (Hakkarainen et al., 2024) and the established industrial Highveld also in South Africa that is a cluster of energy-intensive industries such as mining, metallurgy, and synthetic fuels production (Keita et al., 2021).

So far, the wind rotation and EMG fit (detailed in Section 1.3) has only been applied to 4-5 cities in Sub-Sahara Africa as part of global studies (Goldberg et al., 2021b; Lange et al., 2022). All these past studies have typically compared to bottom-up inventory estimates to validate the EMG approach, but this isn’t suitable for Sub-Saharan Africa where inventory estimates are error-prone due to lack of reliable data for activity factors and lack of emission factors measuring conditions typical of Africa.

It is crucial and urgent to derive recent top-down NO_x emissions for hotspots in Sub-Saharan Africa to constrain NO_x emissions from urban and non-urban hotspots, to evaluate regional emission inventories, to identify underestimated, overestimated, missing, or incorrect spatial allocation of NO_x sources in widely used global and regional emissions inventories and models, and to recommend future research priorities to address discrepancies between top-down and bottom-up estimates of emissions.

1.7 Research Aims

The following are key research aims that this thesis seeks to achieve.

1. To characterise reactive nitrogen seasonality and composition in the global upper troposphere including its partitioning, sources, and abundances by making innovative use of commercial and research aircraft observations and the GEOS-Chem chemical transport model.

2. To identify and quantify errors in model simulations of reactive nitrogen in the upper troposphere from statistical analysis of in situ observations and co-sampled GEOS-Chem abundances and propose potential causes for discrepancies and, where sufficient data exists, suggest solutions.

3. To derive top-down NO_x emissions of hotspots in Sub-Saharan Africa using satellite observations and a near-automated inversion method and use these to evaluate the performance of local and regional bottom-up emissions inventories used for regulatory and research purposes.

4. To propose and test an approach to quasi-independently validate the top-down emissions estimates from (3) using GEOS-Chem and satellite observations rather than the current, widely adopted approach of comparing top-down estimates to regulatory bottom-up inventories.

2: Methodology

2.1 Characterising Oxidized Reactive Nitrogen in the Global Upper Troposphere

I use NASA DC-8 research and In-service Aircraft for a Global Observing System (IAGOS) commercial aircraft campaign measurements, each spanning more than a decade, to characterize global NO_y seasonality and composition in the UT. This follows careful campaign and data selection to isolate observations sampling the UT under standard (climatologically average) conditions and broad assessment of consistent NO_y seasonality between DC-8 and routine IAGOS observations. I go on to use the DC-8 data to critique contemporary understanding of UT NO_y as simulated by the GEOS-Chem model.

2.1.1 Research Aircraft Observations of Total and Components of NO_y

The DC-8 research aircraft has sampled ambient air covering the full extent of the troposphere since its maiden campaign in 1985 (Culter, 2009). Many of the initial campaigns included instruments that measured a subset of the NO_y components shown in Figure 1.9, typically continuous measurements of total NO_y, NO, HNO_3, PAN and PPN, and WAS collection and laboratory detection of C1-C5 ALKNs (Singh et al., 1999). Since 2004, DC-8 campaigns have also included continuous measurements of HNO_4, other PAN-type species and total PNs. Given this, I only consider DC-8 campaigns with a relatively consistent suite of instruments that mostly sampled well-mixed air representative of a climatologically standard atmosphere and that have limited influence from stratospheric air. These criteria eliminate the summer 2004 Intercontinental Chemical Transport Experiment-North America (INTEX-NA) campaign (Singh et al., 2006; Singh et al., 2009) that is the only DC-8 campaign since 2004 to not include a NO_x and NO_y chemiluminescence analyzer, and the summer 2012 Deep Convective Clouds and Chemistry (DC3) campaign that targeted convective thunderstorms influenced by fresh surface pollution and lightning NO_x emissions (Barth et al., 2015).

The DC-8 campaigns I use are the Arctic Research of the Composition of the Troposphere from Aircraft and Satellites (ARCTAS) over the Arctic and sub-Arctic in spring and summer 2008 (Jacob et al., 2010), the Studies of Emissions and Atmospheric Composition, Clouds and Climate Coupling by Regional Surveys (SEAC^{4}RS) over the Southeast US in late summer and early autumn 2013 (Toon et al., 2016), the Korea-United States Air Quality (KORUS-AQ) over South Korea in late spring and early summer 2016 (Crawford et al., 2021), and the Atmospheric Tomography Mission (ATom) that included 4 sub-campaigns along the same flight path from pole to pole over the Atlantic and Pacific Oceans in all 4 seasons from 2016 to 2018 (Thompson et al., 2021). ATom sub-campaigns are ATom-1 in July-August, ATom-2 in January-February, ATom-3 in September-October and ATom-4 in April-May. The data for these campaigns are from NASA data portals for each campaign downloaded as merged 1-minute files for ARCTAS (NASA, 2009), SEAC^{4}RS (NASA, 2015) and KORUS-AQ (NASA, 2017) and as two separate merged files for ATom with the WAS C1-C5 ALKNs data at variable time intervals of 40 s, 1 min and 2 min and without the WAS C1-C5 ALKNs data at 1-minute resolution (NASA, 2021).

Figure 2.1 shows the global sampling extent of the UT by NASA DC-8 after applying filtering criteria to the data to isolate observations representative of photochemical steady-state conditions. For this, I select daytime (08h30-15h30 local solar time or LST) observations within a wide pressure range of 180 to 450 hPa (~8-12 km). The sampling ceiling for DC-8 of 12 km limits the analysis to 180 hPa. The altitude range I use covers the full vertical extent of the UT in the midlatitudes and polar regions but is lower than the vertical extent of the UT in the tropics that reaches to ~100 hPa or 16 km (Section 1.5).

I separate the stratosphere from the troposphere with a tropopause definition that can be applied to all datasets. I remove data with observed O_3 concentrations above regionally and temporally (season) specific thresholds that represent the location of the chemical tropopause (Zahn et al., 2002). The thresholds I use are a single year-round value for the tropics (20°N to 20°S) of 100 ppbv (Dameris, 2015) and seasonally varying values everywhere else calculated using the day-of-year dependent O_3 tropopause equation derived by Zahn et al. (2002) from the inverse relationship between O_3 and CO observations from commercial aircraft campaigns. These thresholds are 120 ppbv in spring, 103 ppbv in summer, 74 ppbv in autumn, and 91 ppbv in winter. I also screen for stratospheric intrusions that result from events like stratospheric folding (identified as observations with O_3/CO > 1.25 mol mol^{-1}) (Hudman et al., 2007), fresh NO_x emissions (NO_y/NO < 3 mol mol^{-1}), fresh convection (large (> 10 nm diameter) condensation nuclei > 10^4 cm^{-3}), biomass burning plumes (CO > 200 ppbv and acetonitrile > 200 pptv) (Shah et al., 2023), as well as instances where NO_2 photolysis frequencies are approximately zero. The latter removes high latitude ATom measurements obtained at 08h30-15h30 LST under dark conditions during polar twilight or polar night. The data that are retained correspond to solar zenith angles ≤ 80^0 in polar regions, and ≤ 60^0 at other latitudes.

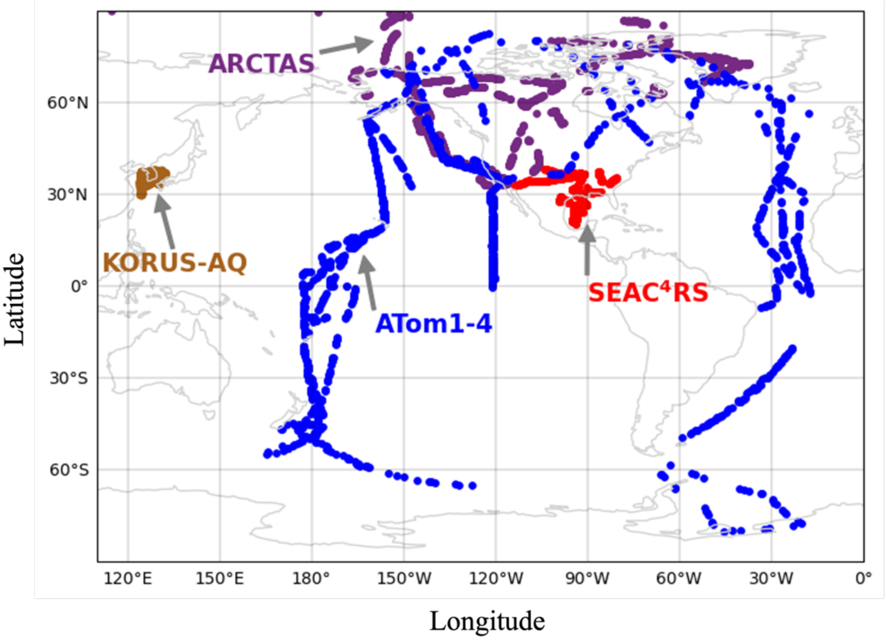

Figure 2. 1: Extent of NASA DC-8 sampling of the upper troposphere under standard, steady-state conditions. Colours distinguish ARCTAS (plum), SEAC^{4}RS (red), KORUS-AQ (brown), and ATom (blue). ATom points are the 1-minute resolution data.

The DC-8 instruments measuring NO_y components (Figure 1.9) are detailed in Section 1.2 along with the uncertainties associated with all measurements and the biases inherent in chemiluminescence NO_2 measurements. The instruments that are common to all campaigns selected include a chemiluminescence instrument measuring NO, NO_2, and total NO_y (Ryerson et al., 2000; Pollack et al., 2010; Bourgeois et al., 2022), a CIMS measuring HNO_3 (Crounse et al., 2006), a CIMS measuring HNO_4, PAN, PPN, and other PANs (Slusher et al., 2004), and a WAS collecting samples analysed in the laboratory using gas chromatography with flame ionization and atomic emission to detect C1-C5 ALKNs (Blake et al., 2003). The other PANs measured with the CIMS are APAN, PiBN, PBN, and PBZN (chemical formulae and names given in Section 1.1). Other instruments deployed for select campaigns are TD-LIF measuring NO_2, total PNs and total ALKNs (ARCTAS, KORUS-AQ, SEAC^{4}RS) and the PANTHER instrument measuring PAN (ATom). There are also TD-LIF MPN measurements reported in the SEAC^{4}RS dataset and derived for ARCTAS by Browne et al. (2011).

Concentrations of NO_2 in the UT (~8 pptv) remote areas are close to the chemiluminescence instrument detection limit (~6 pptv) (Pollack et al., 2010; Bourgeois et al., 2022) and the measurements include interference from decomposition of NO_x reservoir compounds in the instrument inlet (Section 1.2). This effect is particularly severe in the UT where the temperature gradient between the ambient atmosphere and the aircraft is large. Also, thermally unstable reservoir compounds HNO_4 and MPN are abundant in the UT. The Reed et al. (2016b) temperature-dependent inlet temperature decomposition profiles of individual NO_x reservoir compounds for an instrument similar to that operated on the DC-8 suggests interference of 80-100% MPN and 15-45% HNO_4 for the typical inlet temperature range of the DC-8 chemiluminescence instrument of 20-30°C (Bourgeois et al., 2022). For the campaigns that measured HNO_4 and derived or measured MPN, this amounts to 13-27 pptv for ARCTAS and 71-92 pptv for SEAC^{4}RS. Given this, I instead calculate NO_2 using the NO-NO_2 photochemical steady state (PSS) approximation (Section 1.1), as is now standard (Shah et al., 2023; Travis et al., 2016). Conversion of NO to NO_2, mostly (75%) due to oxidation by O_3 in the UT (Silvern et al., 2018), is balanced by NO_2 photolysis back to NO (Section 1.1). As NO_x is in steady state for the daylight observations I isolate, NO_2 can be calculated as follows:

$$\mathrm{NO_2} = \mathrm{NO} \times \left(\frac{k_1[\mathrm{O_3}]+k_2[\mathrm{HO_2}]+k_3[\mathrm{BrO}]}{j_{\mathrm{NO_2}}}\right) \quad (1).$$

Compounds in square brackets are in molecules cm^{-3}. NO and NO_2 are in pptv. Terms not introduced yet in this chapter include the NO_2 photolysis frequency, $j_{\mathrm{NO_2}}$, in s^{-1}, bromine monoxide (BrO), and the rate constants of NO oxidation (R1) (k_{1-3}), in cm^3 molecule^{-1} s^{-1}. Temperature-dependent values of k_{1-3} are those recommended by the Jet Propulsion Laboratory (JPL) (Burkholder, 2020). I calculate these using DC-8 ambient temperature measurements. NO, [O_3], and $j_{\mathrm{NO_2}}$ are from the DC-8 measurements and [HO_2] is from the DC-8 measurements for all campaigns, except SEAC^{4}RS when it was not measured. I use GEOS-Chem (general description in Section 1.3, description specific to this study in Section 2.1.3) simulated [HO_2] to estimate SEAC^{4}RS PSS NO_2. [BrO] is from GEOS-Chem for all campaigns. NO is also converted to NO_2 by

RO_2, but I ignore this reaction, as it is relatively insignificant in the UT (Shah et al., 2023).

2.1.2 Commercial Aircraft Observations of Total NO_y

I use routine observations of UT total NO_y from instruments on commercial long-haul passenger aircraft to determine if, despite the intermittency and brevity of DC-8 campaign observations, these are representative of climatological conditions. The IAGOS European research infrastructure (https://www.iagos.org, last accessed May 2024) provides routine in situ chemiluminescence measurements of NO_y (Petzold et al., 2015). These are available from two IAGOS programmes: the Measurement of Ozone and Water Vapor by Airbus In-Service Aircraft (MOZAIC) (Marenco et al., 1998) from 2001 to 2005 (Volz-Thomas et al., 2005) and the Civil Aircraft for the Regular Investigation of the Atmosphere Based on an Instrument Container (CARIBIC) since December 2004 (Stratmann et al., 2016; Brenninkmeijer et al., 2007).

I consider the MOZAIC and CARIBIC observations together (collectively named IAGOS), as both programmes employed a chemiluminescence instrument with the same NO_y detection technique (Brenninkmeijer et al., 2007; Volz-Thomas et al., 2005). Direct intercomparison of NO_y is not possible, as there is no overlap in MOZAIC and CARIBIC NO_y. Data for 2003 to 2019 are used. These are for 2003-2005 from MOZAIC and 2005-2019 from CARIBIC. I isolate upper tropospheric observations by applying the same O_3 tropopause, stratospheric intrusion, and daytime filtering as is applied to DC-8 data (Section 2.1.2). I do not screen for observations impacted by fresh emissions, vertical convection or biomass burning plumes, due to unavailability of concurrent measurements of suitable chemical tracers in the IAGOS data. As I consider 17 years of IAGOS data, I assume that the influence of these events is dampened in the long-term median of NO_y. Both the IAGOS and DC-8 data are gridded to the same 2° latitude × 2.5° longitude grid.

2.1.3 The GEOS-Chem Model

I use the GEOS-Chem global 3D chemical transport model version 13.0.2 (https://doi.org/10.5281/zenodo.4681204; last accessed May 2021) to represent contemporary understanding of UT NO_y for comparison to DC-8. The model is driven with consistent NASA MERRA-2 assimilated meteorology at 2° × 2.5° (latitude × longitude) over 47 vertical layers from the surface of the Earth to 0.01 hPa. The model emissions local to the UT include cruising altitude aircraft from the Aviation Emissions Inventory Code (AEIC) (Stettler et al., 2011) and lightning emissions as described in Murray et al. (2012). Surface emissions of NO_x and VOCs precursors of ALKNs and PNs are from the anthropogenic CEDS inventory of Hoesly et al. (2018), the Model of Emissions of Gases and Aerosols from Nature (MEGAN) inventory version 2.1 for biogenic VOCs emissions (Guenther et al., 2012), the soil NO_x emission inventory of Hudman et al. (2012), and the Global Fire Emissions Database version 4 with small fires (GFED4s) for open burning of biomass (Giglio et al., 2013). Wet deposition of gas-phase HNO_3, the terminal sink for NO_y subsiding from the UT, includes in-cloud (rainout) and below-cloud (washout) scavenging as detailed in Amos et al. (2012) and enhanced scavenging as described by Luo et al. (2020).

I sample the model at the same time and location as the DC-8 observations using the ObsPack diagnostic (https://www.esrl.noaa.gov/gmd/ccgg/obspack/; last accessed 23 October 2024) following a minimum 10-month spin-up preceding each campaign to initialize chemistry and large-scale circulation throughout the troposphere. Modelled components of NO_y include NO, NO_2, HNO_3, HNO_4, PAN, PPN, MPAN, MPN, and individual C1-C3 ALKNs.

2.2 Deriving NO_x Emissions of Hotspots across Sub-Saharan Africa

I use the recently published near-automated, multisampling approach of Lu et al. (2025) with wind rotation and an EMG fit to isolated hotspots observed from the space-based UV-visible TROPOMI to estimate annual NO_x emissions for these hotspots. I assess the reliability of these top-down estimates by scaling a widely used global emission inventory to match the top-down emissions and sample tropospheric columns of NO_2 from the GEOS-Chem model driven with the updated emissions to evaluate against TROPOMI. Finally, I compare my evaluated top-down emissions to a regional inventory for Africa and a bespoke inventory used to inform regulatory action to address poor air quality in priority areas in South Africa.

2.2.1 Top-down Estimate of Hotspot NO_x Emissions

I use Level-2 retrieval version 02.03.01 TROPOMI NO_2 tropospheric vertical column densities for 2019 from the Sentinel-5P Products Algorithm Laboratory (S5P-PAL) portal (https://data-portal.s5p-pal.com/, last accessed 5 April 2024). TROPOMI achieves daily global coverage with a 2600 km swath and an Equator crossing time of 13:30 LST. For the target year (2019), the nadir pixel resolution increases from 7 km × 3.5 km to 5.5 km × 3.5 km on 5 August 2019. Only cloud-free, high-quality data (identified with the provided quality flag ≥ 0.75) are selected (van Geffen et al., 2020). I apply oversampling to TROPOMI NO_2 to grid the data to a fine spatial resolution of 0.05° (~6 km × ~5 km at the Equator) (Figure 2.2) to resolve potential target hotspots. Oversampling improves spatial resolution by combining multiple overlapping satellite observations, filling gaps, smoothing data using mathematical functions, and projecting onto a finer grid to reveal small-scale details. This is enabled by deliberate sub-pixel shifts in the satellite's orbit or sensor positioning, which allow multiple observations of the same area from slightly different perspectives (Sun et al., 2018).

Figure 2.2. shows annual mean oversampled TROPOMI tropospheric NO_2 vertical column densities over Sub-Saharan Africa in 2019. From this map, I manually select 28 isolated hotspots. Isolated hotspots are selected, as these yield discernible plumes when wind rotated (Beirle et al., 2011). If hotspots are too close together, the neighbouring hotspot forms part of the background of the other hotspot, leading to biases in the emissions estimates. The hotspots that are selected for Sub-Saharan Africa include 26 cities across Sub-Saharan Africa and two non-city hotspots in South Africa. The non-city hotspots are the industrial Highveld east of Johannesburg and the combined NO_2 enhancement from the Medupi and Matimba coal-fired power stations located ~6 km apart. In comparison to hotspots isolated for other regions of the world, most of the cities in Africa have relatively modest enhancements in tropospheric column NO_2, as these cities are still dominated by inefficient combustion sources that produce relatively more CO and VOCs than NO_x in comparison to cities in Europe, the US, China, and Southeast Asia (Liu et al., 2021; Goldberg et al., 2019b; Sekiya et al., 2022; Wu et al., 2021b; Lu et al., 2025). The maximum enhancement for selected cities north of South Africa is ~3×10^{15} molecules cm^{-2} compared to >6×10^{15} molecules cm^{-2} for South and Southeast Asia (Lu et al., 2025) >8×10^{15} molecules cm^{-2} for the North China Plains (Wu et al., 2021b), and $5\text{-}10 \times 10^{15}$ molecules cm^{-2} for cities in Europe and North America (Liu et al., 2021; Goldberg et al., 2019b; Sekiya et al., 2022). The extensive hotspots in South Africa that include the two neighbouring cities Pretoria and Johannesburg to the west and the industrial Highveld to the east are amongst the largest global hotspots of tropospheric NO_2, due to emissions of NO_x from traffic, energy generation, energy-intensive industrial processes, and synthetic fuels production (Lourens et al., 2016; Lourens et al., 2012).

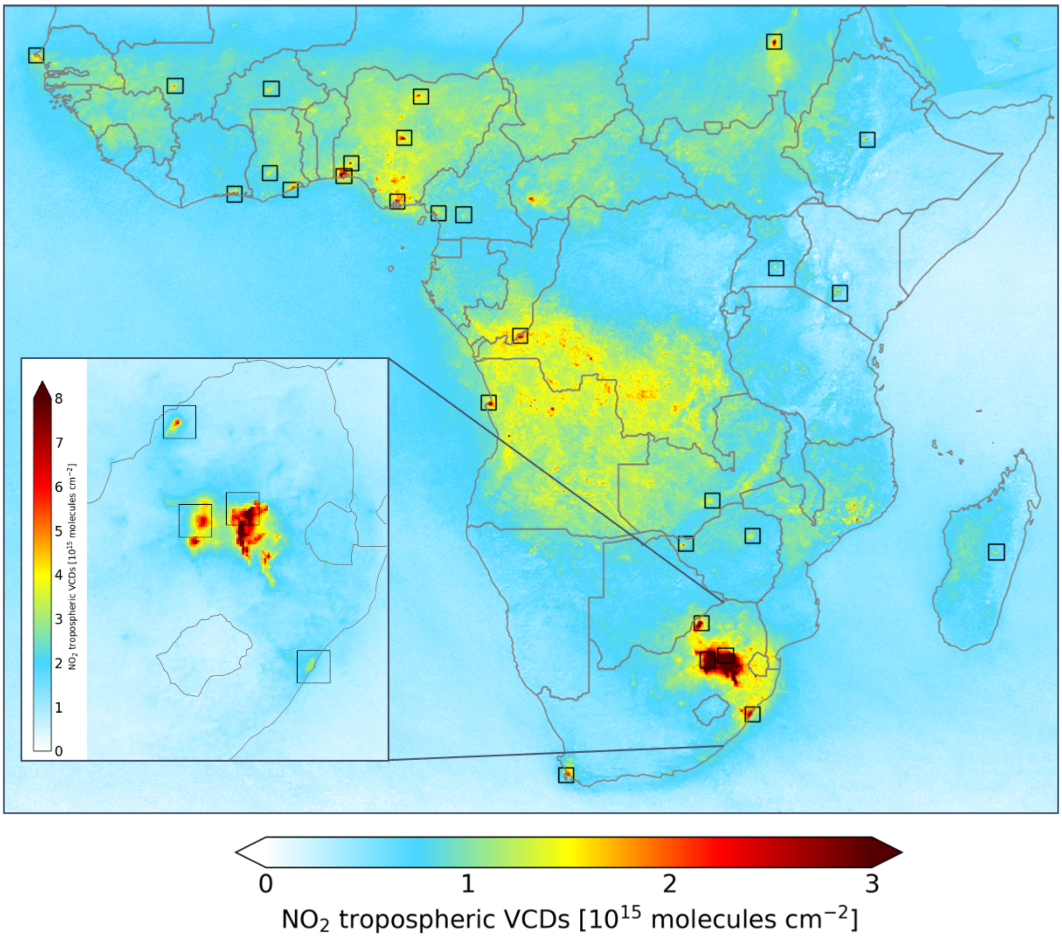

Figure 2. 2: Annual mean TROPOMI tropospheric NO2 vertical column densities over Sub-Saharan Africa in 2019. Map shows Sub-Saharan Africa NO_2 oversampled to $0.05^0 \times 0.05^0$. Squares are 28 selected hotspots. Inset is northeast South Africa on a separate scale.

The traditional EMG fit approach (Section 1.3) requires that a user define a sampling area around the city that effectively captures the wind rotated plume. The area selected varies with city size and plume length (Goldberg et al., 2019b; Lange et al., 2022; Lu et al., 2015). This approach often yields no or poor EMG fits and non-physical best-fit parameters (Laughner& Cohen, 2019), decreasing the likelihood of deriving top-down emissions. Lu et al. (2025) updated this top-down approach by defining many (54) sampling areas that they test with TROPOMI NO_2 observations over 19 cities in South and Southeast Asia. This updated approach eliminated the need for subjective sampling area selection and increases success of deriving annual emissions from 40-60% with a single sampling area to 100% (all 19 cities) with 54 sampling areas. This aspect is particularly pertinent for Sub-Saharan Africa where the hotspots range in size and many are more similar to the surrounding background concentrations than other regions of the world. So, I follow the approach from Lu et al. (2025) to calculate NO_x emissions for the hotspots selected in Figure 2.2. This approach automates the process of sample box selection around each hotspot by defining 54 sampling boxes for each hotspot with varying lengths.

Figure 2.3 outlines the hotspot sampling and the EMG fit to the 54 sampling boxes to derive annual NO_x emissions for Lagos (Nigeria), the most populated city in Africa and one of the fastest growing cities in the world (Yuen& Kumssa, 2011). The wind speeds and directions used to rotate TROPOMI NO_2 columns are calculated using the ERA5 3D hourly wind components (u and v) at 0.25° × 0.25° resolution (https://cds.climate.copernicus.eu, last accessed 6 April 2024). At each TROPOMI NO_2 pixel, collocated mean ERA5 wind speeds and directions are computed within 30 minutes of the 13:30 LST TROPOMI overpass, using the lowest 5 layers (≥ 900 hPa) to capture dispersion of near-surface NO_2 plumes. Within a 4° × 4° domain around the hotspot centre, TROPOMI pixels with wind speeds >2 m/s are selected. This wind speed threshold is selected, as it is consistent with thresholds from prior studies (Beirle et al., 2011; Pope et al., 2022; Lu et al., 2025). NO_2 pixels are rotated by wind direction, aligning the pixels along the same upwind-downwind axis (north-south in this study). These rotated pixels are gridded to a 0.05° × 0.05° resolution using point-in-box averaging rather than oversampling (Figure 2.2), as the NO_2 is to be integrated along the west-east direction anyway. NO_2 concentrations for any unfilled cells, though rare given the high sampling frequency of a year of TROPOMI observations, are obtained by interpolation nearest neighbour grid squares. This is to minimize biases in the integration step that follows.

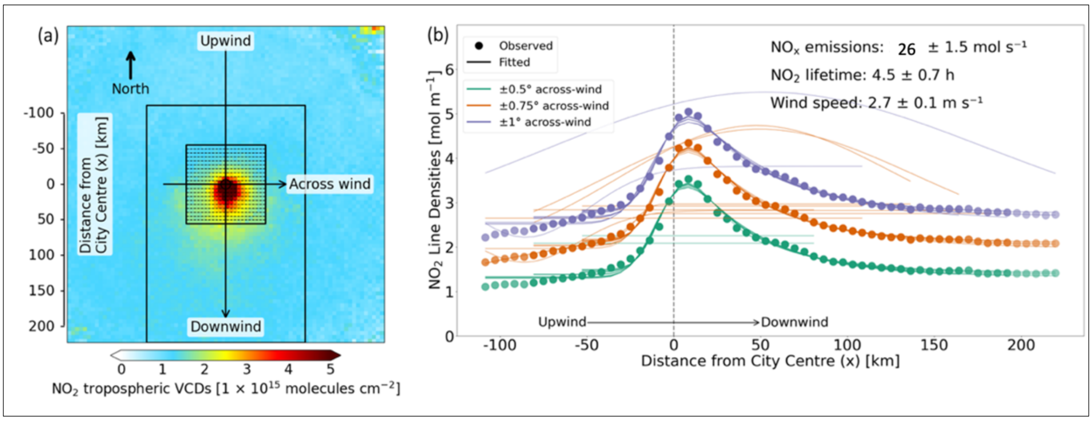

Figure 2. 3: Major steps in wind rotation and EMG fitting to derive NOx emissions for Lagos in 2019. Panel (a) is TROPOMI NO$_2$ pixels are wind-rotated and gridded to 0.05° × 0.05°. Black rectangles outline the largest and smallest sampling areas, with dashed lines in the smallest area indicating 0.05° increments used for line density calculations in (b). Panel (b) is EMG fits (solid lines) to observed line densities (filled circles), with 39 successful fits. Values indicate the mean and standard deviation of NO$_x$ emissions (Eq. (2)) and the ERA5 wind speed for all successful fits.

The 2D map in Figure 2.3 (a) is converted into 1D line densities by summing grid cells across the east-west direction in 0.05° north-south increments within the defined area (filled circles in Figure 2.3(b)). Following Lu et al. (2025), multiple areas are selected, defined as distances from the city centre, of 0.5°, 0.75°, and 1° upwind; 0.5° to 2.0° downwind in 0.25° increments; and 0.5°, 0.75°, and 1° across-wind. Downwind distances are not shorter than the upwind distances to ensure the full city plume is captured. This requirement and the defined box lengths result in 54 boxes and corresponding line densities. The smallest and largest areas sampled, as well as across-wind 0.05° increments summed for line densities, are illustrated in Figure 2.3 (a).

The EMG model I use to fit to the observed 1D line densities is the Laughner and Cohen (2019) formulation:

$$F(x|a, x_0, \mu_x, \sigma_x, B) = \frac{a}{2x_0}\exp\left(\frac{\mu_x}{x_0} + \frac{\sigma_x^2}{2x_0^2} - \frac{x}{x_0}\right)\operatorname{erfc}\left(-\frac{1}{\sqrt{2}}\left[\frac{x-\mu_x}{\sigma_x} - \frac{\sigma_x}{x_0}\right]\right) + B \qquad (2),$$

where x is the distance of each line density upwind and downwind from the city centre (Figure 2.3 (b)), with the best-fit parameters a, x_0, μ_x, σ_x and B defining key aspects of the plume. Specifically, a is total NO_2 in the plume (in moles), x_0 is the e-folding distance or length scale of NO_2 decay (in km), and μ_x is the apparent source location relative to the city centre (in km), corresponding to the peak of the Gaussian fit, which in Figure 2.3 is located approximately 20 km downwind (south) of the city centre. The parameter σ_x is the Gaussian smoothing length scale (in km), and *B* represents the background NO_2 concentration (in moles per meter).

I use initial guesses for the best-fit parameters in Equation (2) similar to Lu et al. (2025). The fitting procedure I use is also that developed by Lu et al. (2025) that was coded using the scipy.optimize.curve_fit module (SciPy v1.7.3). I iterate over the fit until changes in best-fit parameters are negligible (<0.001%) for up to 10 iterations. Convergence is typically achieved within 3 iterations. Fits are retained only if these achieve a goodness-of-fit of $R^2 > 0.8$, as is standard (Laughner& Cohen, 2019; Lu et al., 2025). I further filter to ensure that only physically plausible parameters are retained. To do so, I use criteria detailed by Lu et al. (2025): a is positive, x_0 is at least 1.6 km ($1/e$ of the grid resolution), μ_x is within the sampling area, $\sigma_x < x_0$ (emission width less than e-folding distance), background NO_2 is positive and less than the maximum line density, x_0 falls between the plume centre and the sampling area edge, and x_0 is within the sampling area (i.e., x_0 < downwind sampling area length).

Successful EMG fits are used to derive effective NO_x lifetimes ($\tau_{\mathrm{NO_x}}$; reported in h) and midday NO_x emissions ($E_{\mathrm{NO_x}}$; in moles s^{-1}) using the equation:

$$\tau_{\mathrm{NO_x}} = \frac{x_0}{\omega} \quad (3)$$

$$E_{\mathrm{NO_x}} = \frac{\gamma \times a}{\tau_{\mathrm{NO_x}}} \quad (4).$$

Here, ω is the mean wind speed ($m\ s^{-1}$) and γ is the molar ratio of $[NO_x]/[NO_2]$ to convert moles NO_2 to moles NO_x in the sampling area. Up to 54 estimates of $\tau_{\mathrm{NO_x}}$ and E_{NO_x} are averaged to get values for each hotspot.

I use $[NO_x]/[NO_2] = 1.32$ as in Beirle et al. (2011) to represent rapid NO–NO_2 cycling. While this ratio is original from the textbook on atmospheric chemistry of Seinfeld and Pandis (2016) for a specific case, subsequent studies have tested its broader suitability. Liu et al. (2022) showed through synthetic experiments that city-scale NO_x emission estimates are relatively insensitive to variations in $[NO_x]/[NO_2]$, though their work focused on US cities. Lu et al. (2025) provide further justification by explicitly assessing whether the fixed ratio is appropriate in other regions using the GEOS-Chem chemical transport model. They compared simulations from both coarse-resolution (2° × 2.5°) and high-resolution (~25 km) configurations of GEOS-Chem, sampled around the TROPOMI overpass time. Their results confirmed that midday NO_x is in photochemical steady state (section 1.1), making the NO–NO_2 partitioning relatively stable across different resolutions and city environments, including coastal locations. Lu et al. (2020) also quantified uncertainties in the ratio by evaluating deviations from 1.32 in the model and concluded that the ±10% uncertainty estimate proposed by Beirle et al. (2011) remains appropriate. Thus, there is model-based evidence that the $[NO_x]/[NO_2] = 1.32$ ratio is a reasonable and robust choice across diverse urban environments.

As in Lu et al. (2025), emission uncertainties are calculated by combining individual errors in quadrature, including best-fit parameters (a and x_0), mean wind speed (), and TROPOMI NO_2 observations. Errors in a and x_0 are determined using the relative standard deviation from successful EMG fits. The uncertainty estimates I use for account for uncertainties due to the choice of spatial (< 900 hPa) and temporal (30 min before and after 13h30 LST) sampling, and the windy condition thresholds. I use 10% for the temporal sampling error and 5% for the vertical sampling error, as in Beirle et al. (2011). The AMF, a major source of error in NO_2 VCDs (Section 1.2), remains similar for OMI and TROPOMI (van Geffen et al., 2020). Thus, a 30% error applied to the OMI NO_2 observations by Beirle et al. (2011) is also appropriate to apply to the TROPOMI NO_2 observations used here.

2.2.2 Evaluation of Top-down NO_x Emissions Using GEOS-Chem and TROPOMI

The typical approach that is used to evaluate top-down NO_x emissions from the wind rotation and EMG method involves comparison of the top-down NO_x emissions to bottom-up values (Goldberg et al., 2021b; Beirle et al., 2011; Lange et al., 2022). This approach is not suitable for Sub-Saharan Africa, as the bottom-up emissions estimates are not as reliable as those developed for regions such as Europe, the US, and China. These parts of the world have well-developed bottom-up emission inventories development methodologies, routinely update the inventories, and use detailed activity factor data and local emission factor data to build the inventories.

Given these limitations of existing bottom-up emissions estimates for Africa, I instead assess the top-down NO_x emissions by comparing simulated tropospheric columns of NO_2 to TROPOMI. I use the GEOS-Chem chemical transport model (GCClassic, version 13.0.2; https://zenodo.org/records/4681204) in its finest horizontal resolution flexible nested grid configuration (0.25° latitude x 0.3125° longitude) to simulate NO_2 column densities. The model is simulated twice, driven with (i) default bottom-up anthropogenic emissions and (ii) the bottom-up anthropogenic emissions scaled to match the top-down emissions derived with wind rotation and the EMG fit (Section 2.2.1). To do so, I conduct multiple model runs of nested domains covering 18 of the 28 isolated hotspots in Figure 2.4. These domains are: a) Dakar, Senegal (6-24°N, 8-26°W), b) Abidjan (Ivory Coast), Accra (Ghana), Lagos, Ibadan, Kano, Port Harcourt (Nigeria) and Douala (Cameroon) (6°S-20°N, 12°W-18°E), c) Khartoum, Sudan (5-25°N, 22-42°E), d) Addis Ababa, Ethiopia (1°S-19°N, 29-49°E), e) Nairobi, Kenya (10°S-8°N, 28-45°E), f) Luanda, Angola (0-18°S, 5-22°E), g) Hwange, Zimbabwe (10-28°S, 18-38°E), h) northeast South Africa hotspots of the Highveld, Johannesburg, Durban and the Medupi-Matimba power stations (15-36°S, 14-35°E) and i) Cape Town, South Africa (24-44°S, 8-28°E) (Figure 2.3).

NO_x emissions in the model are from the anthropogenic CEDS version 2 (CEDSv2) at 0.1° resolution (McDuffie et al., 2020) for almost all anthropogenic source sectors (energy, industry, shipping, traffic, residential and commercial), except aircraft, that are from AEIC (Stettler et al., 2011). The time resolution of NO_x emissions in CEDSv2 is monthly. The model then applies hourly scale factors to represent variability in emissions during the day. These are from the EDGAR emissions inventory. Biomass burning emissions are from GFED4s (Giglio et al., 2013). Natural emissions are read in as offline resolution-independent files generated using the Hudman et al. (2012) parameterization for soils and the Murray et al. (2012) parameterization for lightning. Boundary conditions, updated every 3 hours, are from the global 4° x 5° model. The model undergoes a spin-up for chemical initialization of 1 year for the global boundary conditions and 2 months for each of the nested domains. Model concentrations of NO_2 are sampled during the TROPOMI overpass time (12:00-15:00 LST) to calculate annual tropospheric column NO_2 means for 2019.

Models typically underestimate NO_2 throughout the free troposphere (Horner et al., 2024) and include large biases in emissions of NO_x from open burning of biomass (Zheng et al., 2018). For the relatively small concentrations of NO_2 typical of hotspots in most of Sub-Saharan Africa, these biases can have a large influence on tropospheric NO_2 column densities. To mitigate influence of this known model bias on assessment of the top-down NO_x emissions, I determine and subtract off the background contribution to the tropospheric columns by sampling NO_2 in a 20 km^2 box located either west, east, north, or south of each hotspot before comparing the enhancement in NO_2 above the background from TROPOMI and from GEOS-Chem. The GEOS-Chem output that is compared to TROPOMI is obtained both before and after adjusting NO_x emissions to match the top-down estimates.

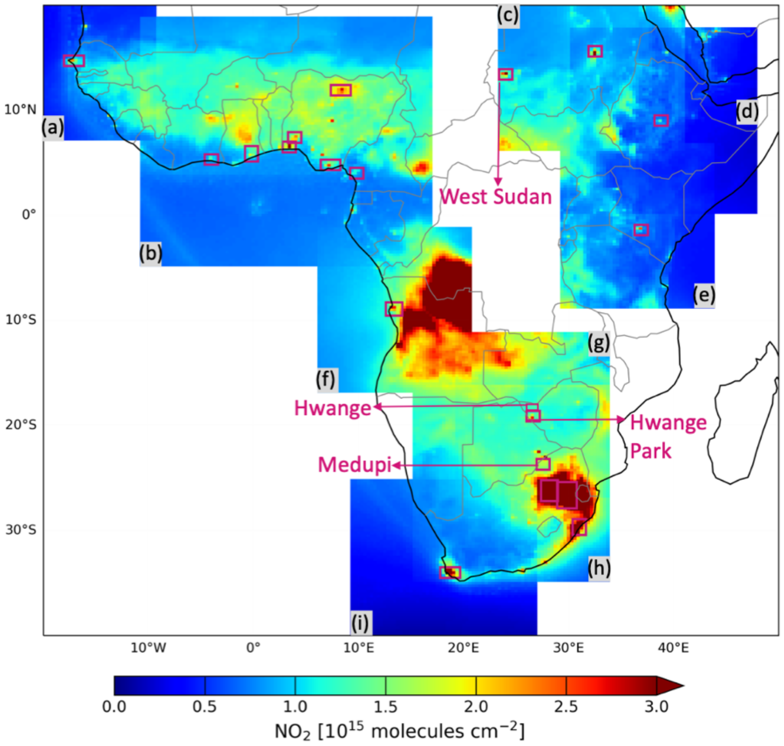

Figure 2. 4: GCClassic tropospheric NO_2 vertical column densities for 2019. Values are obtained with the default NO_x emissions inventories detailed in Section 2.2.

2.2.3 Assessment of Regional Bottom-up Emissions Inventories

The evaluated top-down NO_x emissions are then used to evaluate the northeast South Africa emission inventory for 2019 and a newly developed version of the DACCIWA regional bottom-up emission inventory for 2018. The DACCIWA inventory has a spatial resolution of 0.1° × 0.1° and a temporal resolution of one year (annual emissions). The original inventory DACCIWA was developed for 1990–2015 (Keita et al., 2021), but this has since been extended by the lead inventory developer to 2018 that I evaluate. DACCIWA is an African regional anthropogenic emission inventory that accounts for the main African polluting sources (wood and charcoal burning, charcoal making, trucks, cars, buses and two-wheeled vehicles, open waste burning, and natural gas flaring) and incorporates emission factors that are specific to conditions in

Africa (Keita et al., 2021; Liousse et al., 2014). These, for example, account for relatively inefficient combustion sources such as diesel and petrol generators that are often the primary source of electricity for many residential areas in Africa. Other sources include widespread use of motorcycles or two-stroke engines that produce large quantities of CO and organic aerosols (OA) and are a relatively modest source of NO_x in comparison to four-stroke engine vehicles (Liousse et al., 2014).

The South African emission inventory does not have an accompanying peer-reviewed publication. It is developed by researchers based at the South African Council for Scientific and Industrial Research (CSIR). The data are provided as annual means on a 6 km × 6 km fixed horizontal grid. The inventory covers the northeast portion of South Africa where there is a dedicated air quality priority region to address severe air pollution from industrial, power plant and city sources. The data used to construct the inventory include reported emissions provided by industry and the large energy utility in South Africa, Eskom. Also included to develop the inventory are data from Continuous Emissions Monitoring (CEMS) that measure gas and particle concentrations at industrial stacks to determine the emissions of these (Woollatt, 2015).

I compare NO_x emissions from the DACCIWA and the northeast South Africa inventories to my top-down NO_x estimates to assess consistency between the top-down and bottom-up approach, and to identify future research needs based on the size of discrepancies between the two approaches.

3: Characterization of Reactive Oxidized Nitrogen in the Global Upper Troposphere

The work presented in this Chapter has been published in Atmospheric Chemistry and Physics (ACP): Wei, N., Marais, E. A., Lu, G., Ryan, R. G., and Sauvage, B.: Characterization of reactive oxidized nitrogen in the global upper troposphere using recent and historic commercial and research aircraft campaigns and GEOS-Chem, Atmos. Chem. Phys., 25, 7925–7940, https://doi.org/10.5194/acp-25-7925-2025, 2025.

This chapter presents the results and discussion of a study that uses reactive nitrogen observations from the NASA DC-8 research aircraft and the IAGOS campaigns to characterize the seasonality and composition of reactive oxidized nitrogen (NO_y) in the global upper troposphere. These observations are compared with simulations from the state-of-the-science GEOS-Chem model to identify the largest knowledge gaps. Addressing these gaps is essential for improving assessments of climate, the nitrogen cycle, and air pollution. The chapter is organized into three parts, each presenting results followed by corresponding discussions. The first part examines NO_y seasonality and budget closure in the upper troposphere, presenting total NO_y seasonality from both aircraft observations and GEOS-Chem simulations, as well as budget closure analysis using DC-8 individual NO_y components. The second part focuses on upper-tropospheric NO_y composition, highlighting regional variations in the absolute concentrations of individual NO_y components and their relative contributions. The third part reviews the contemporary understanding of upper-tropospheric NO_y, identifying knowledge gaps in our understanding of the concentrations and contributions of individual NO_y species through comparisons with model simulations. These gaps are critical targets for future research on the nitrogen cycle, air pollution, and climate.

3.1 DC-8 Campaign NO_y Seasonality and Budget Closure

Figure 3.1 compares seasonality in UT NO_y from IAGOS and DC-8. Most of the overlap is with ATom along the North Atlantic flight corridor in all seasons, ARCTAS over the Canadian Arctic and Greenland in March-May (MAM) and June-August (JJA), and SEAC^{4}RS over the Southeast US in September-November (SON). Similar to DC-8, IAGOS NO_y exhibits peaks in spring (563 pptv) and summer (565 pptv), due to intensive seasonal lightning in the northern hemisphere (Stratmann et al., 2016). Decline in this source decreases NO_y in autumn to 365 pptv and NO_y further decreases in winter to an annual minimum of 284 pptv.

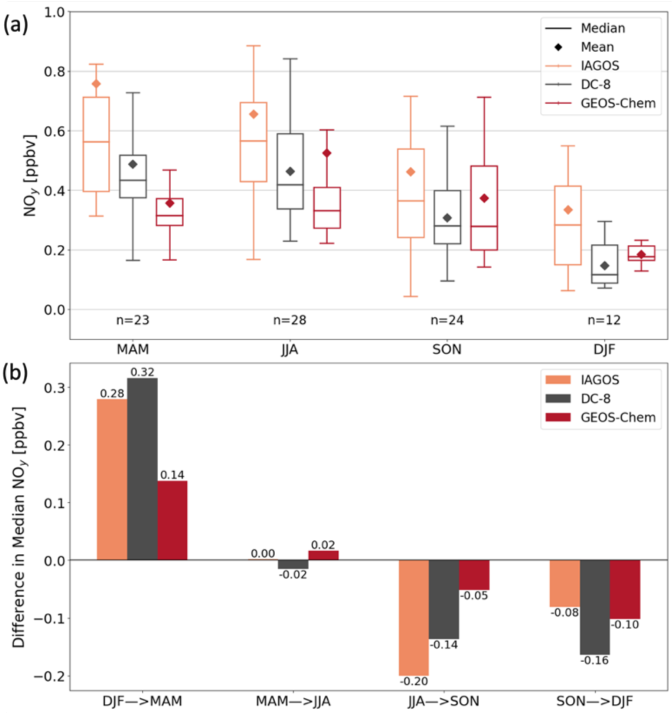

Figure 3. 1: Seasonality of Northern Hemisphere upper tropospheric NO_y. Panels show seasonal means and medians (a) and seasonal transitions (b) of collocated gridded 2° × 2.5° NO_y from IAGOS (orange), DC-8 (grey), and GEOS-Chem (red). Data in (a) are medians (lines), 25th and 75th percentiles (boxes) and means (diamonds). Inset text in (a) gives the number (n) of overlapping grid cells. Seasonality in (b) is the change in median NO_y in (a) from one season to the next.

DC-8 NO_y seasonality is similar to that of IAGOS, though the magnitude of DC-8 NO_y is consistently on average, ~130 pptv (range of 80 pptv in SON to 170 pptv in DJF) less than IAGOS NO_y in all seasons. The ~130 pptv greater IAGOS NO_y likely results from differences in sampling altitudes. Figure 3.2 shows that the two campaigns sampled different altitude ranges within the upper troposphere: IAGOS measurements were centred around ~240 hPa (~10 km), representing the upper portion of the upper troposphere, while DC-8 measurements covered a broader vertical extent cantered near ~360 hPa (~1.5 km below IAGOS). A general pattern of steeply increasing NO_y with altitude is evident, except for IAGOS layers near 300 hPa during March–May and September–November. For the limited instances when both DC-8 and IAGOS sampled the same pressure layers, average NO_y values were similar.

Another minor factor may be IAGOS NO_y instrument interference from HCN. The IAGOS chemiluminescence instruments use a hydrogen (H_2) reagent to convert oxygenated nitrogen compounds to NO, whereas DC-8 uses CO, a compound not permitted on commercial aircraft (Bradshaw et al., 1998; Volz-Thomas et al., 2005; Thomas et al., 2015). The H_2 reagent converts anywhere from 2 to 20% of HCN to NO_y (Weinheimer, 2006). HCN ambient concentrations typically seasonally vary from ~200 to 300 pptv in the upper troposphere, amounting to an interference of 4-60 pptv (Li et al., 2003; Le Breton et al., 2013).

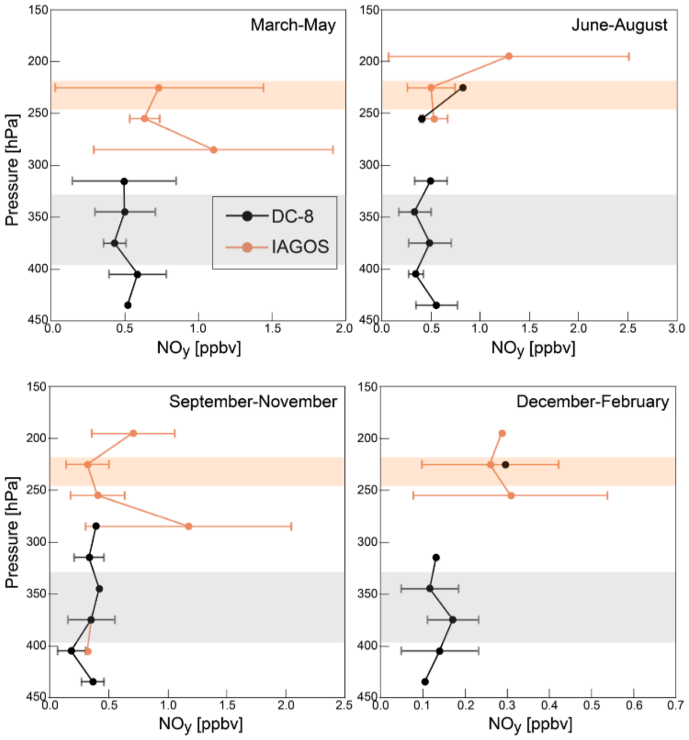

Figure 3. 2: Comparison of seasonal mean vertical profiles of NO$_y$ from collocated DC-8 and IAGOS aircraft observations. Symbols are means from averaging upper troposphere (450-180 hPa) observations into 30 hPa bins. Lines are standard deviations. Shading indicates the typical vertical sampling range (pressure standard deviation) of DC8 (grey) and IAGOS (orange).

Figure 3.3 shows the relationship between the sum of individual NO$_y$ components and total NO$_y$ for each DC-8 campaign. I use these scatterplots to determine whether most NO$_y$ components are measured in each campaign, given my intention to use DC-8 to assess contemporary understanding of UT NO$_y$. Table 3.1 listed the instruments and individual components of NO$_y$ summed for comparison with total NO$_y$. The measured components include NO; PSS NO$_2$ (calculated using Equation (1)); HNO$_3$; PAN measured as PAN for all ATom sub-campaigns and as part of total PNs for ARCTAS, SEAC^{4}RS and KORUS-AQ; HNO$_4$ measured as HNO$_4$ for ATom-1 and -2 and as part of total PNs for ARCTAS, SEAC^{4}RS and KORUS-AQ; C1-C5 ALKNs for all AToms; total ALKNs for SEAC^{4}RS, KORUS-AQ, and ARCTAS; PPN and other PANs for all except ATom-1 and -2; and MPN as part of total PNs for ARCTAS, SEAC^{4}RS and KORUS-AQ. The evaluation in Figure 3.3 is biased toward the northern hemisphere, as the low time resolution sampling of ALKNs during

ATom leads to loss of data in the southern hemisphere (Figure 2.1) to achieve coincidence of DC-8 total and individual components of NO_y.

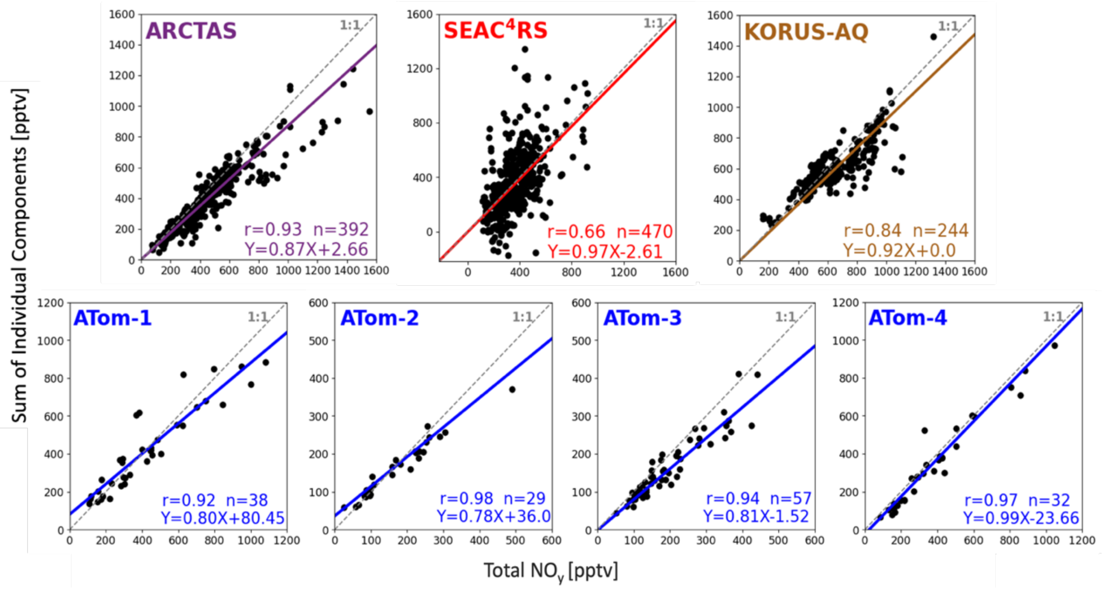

Figure 3. 3: Proportion of oxidized reactive nitrogen components measured during each campaign. Individual points compare the coincident sum of individual NO_y components to measured total NO_y during NASA DC-8 campaigns. Individual NO_y components used in the figure are detailed in the text. Dashed grey lines are the 1:1 relationship. Coloured lines and inset equations are the Theil-Sen regression fit to the observations. Other inset values are the Pearson's correlation coefficient (r) and number of points (n). Axis ranges differ in each panel.

Table 3.1: Observations of individual NO_y components summed to assess budget closure in figure 3.3.

Component	NASA DC-8 aircraft campaign		
	ARCTAS, SEAC^{4}RS, KORUS-AQ	ATom1-2	ATom3-4
NO_2	PSS	PSS	PSS
NO	Chemiluminescence (CL)	CL	CL
HNO_3	CIMS	CIMS	CIMS
HNO_4	TD-LIF PNs	CIMS	–
PAN	TD-LIF PNs	PANTHER	PANTHER
PPN	TD-LIF PNs	–	CIMS
other PANs	TD-LIF PNs	–	CIMS
ALKNs	TD-LIF ALKNs	WAS C1–C5	WAS C1–C5
MPN	TD-LIF PNs	–	–

Total measured NO_y and the sum of individual NO_y components are strongly correlated ($r > 0.8$) for all campaigns, except SEAC^{4}RS ($r = 0.66$). The weaker correlation for SEAC^{4}RS is due to the large contribution of MPN to total PNs measured by the TD-LIF instrument, leading to a large contribution of MPN to total NO_y for many of the points that stray most from the 1:1 line (Figure 3.4). If instead I replace TD-LIF PNs with the sum of CIMS PANs and HNO_4, the correlation with total measured NO_y increases to $r=0.91$, but the regression slope decreases from 0.97 in Figure 3.3 to 0.82, as MPN is ~ 20 % of SEAC^{4}RS NO_y. The large contribution of MPN to total NO_y during SEAC^{4}RS (Figure 3.4) results from aged air initially influenced by lightning, biomass burning, and deep convective uplift of surface pollution with large quantities of VOCs and NO_x. These large quantities of VOCs and NO_x cause very active photochemistry that enhances the abundance of the MPN precursor, CH_3O_2 (Nault et al., 2015; Browne et al., 2011).

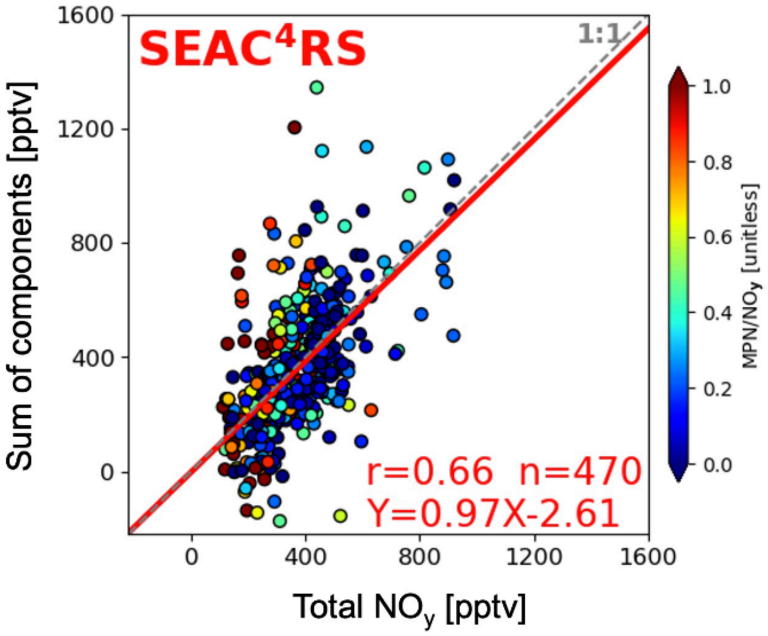

Figure 3. 4: Proportion of reactive oxidized nitrogen components measured during SEAC^{4}RS. Figure format and inset values are as in Figure 3.3, but for SEAC^{4}RS only and points are coloured by the relative proportion of methyl peroxy nitrate (MPN).

The regression slopes in Figure 3.3 indicate that most NO_y components are measured during each campaign, ranging from 0.78 for ATom-2 (78 % of individual NO_y components measured) to 0.99 for ATom-4 (99 % measured). The slopes suggest that between 1 % and 22 % of NO_y originates from factors such as unmeasured components, positive interference in the NO_y instrument, or a low bias in the TD-LIF PNs. Bradshaw et al. (1998) estimated a temperature-dependent interference from HCN of 8-15% for chemiluminescence instruments that, like those deployed on DC-8 campaigns, use a CO reagent. I estimate a lower-end (8%) interference for mean ambient UT temperatures measured along the flight paths in Figure 2.1. Using DC-8 HCN observations, this amounts to ~ 53 ppt or 12 % of NO_y for ARCTAS, ~ 19 pptv or 5 % of NO_y for SEAC^{4}RS, ~ 40 pptv or 6 % of NO_y for KORUS-AQ, and ~ 17 pptv or 6 % of NO_y for ATom 1-4. These lower-end interference estimates are similar in size to the percent of unaccounted NO_y (13 % for ARCTAS, 3 % for SEAC^{4}RS, 8 % for KORUS-AQ, 1 %–22 % for ATom).

Chemiluminescence NO_y instruments also detect pNO_3, though with uncertain sampling efficiencies (Bourgeois et al., 2022). Assuming 100 % sampling efficiency, I use aerosol mass spectrometer (AMS) measurements of submicron (< 1 μm) pNO_3 to estimate its contribution to NO_y. This contribution is at most ~1 % during ARCTAS (median $pNO_3 \approx 0.01$ μg m^{-3}, ~4 pptv), ~4 % during SEAC^{4}RS (≈ 0.04 μg m^{-3}, ~14 pptv), ~4 % during KORUS-AQ (≈ 0.07 μg m^{-3}, ~25 pptv), and < 2 % during ATom (< 0.01 μg m^{-3}, ~4 pptv).

TD-LIF measurements of PNs are calculated from the difference in NO_2 detected with the NO_2 channel and with the PNs channel set to a temperature at which all PNs decompose (Wooldridge et al., 2010; Nault et al., 2015) (Section 1.2). A bias in NO_2 could therefore impart a bias in PNs. The largest source of TD-LIF interference is the 100 % thermal decomposition of MPN (Reed et al., 2016b), and MPN during SEAC^{4}RS far exceeds that of any of the other campaigns. If I use the higher-end MPN interference of 21 % from

Shah et al. (2023) for SEAC^{4}RS, this equates to ~ 5 pptv of SEAC^{4}RS PSS NO_2. This is only ~ 3 % of the 190 pptv SEAC^{4}RS PNs.

3.2 Upper Tropospheric NO_y Composition

Figure 3.5 provides a breakdown of the absolute and relative contributions of individual NO_y components to total NO_y. ATom-1 and -4 are combined, as these sub-campaigns have a very similar range in NO_y (Figure 3.3) and in median total and individual components of NO_y, as the sampled seasons (spring and summer) have very comparable NO_y (Figure 3.1). Similarly, ATom-2 and -3 (autumn and winter) are combined. Campaigns are further grouped into remote (ARCTAS, ATom) and continental (SEAC^{4}RS, KORUS-AQ), as local influence from continental sources like anthropogenic emissions and intense lightning promoted very active deep convection over land leads to a greater relative contribution of NO_x and lesser contribution of PAN for the continental upper troposphere and vice versa for the remote upper troposphere.

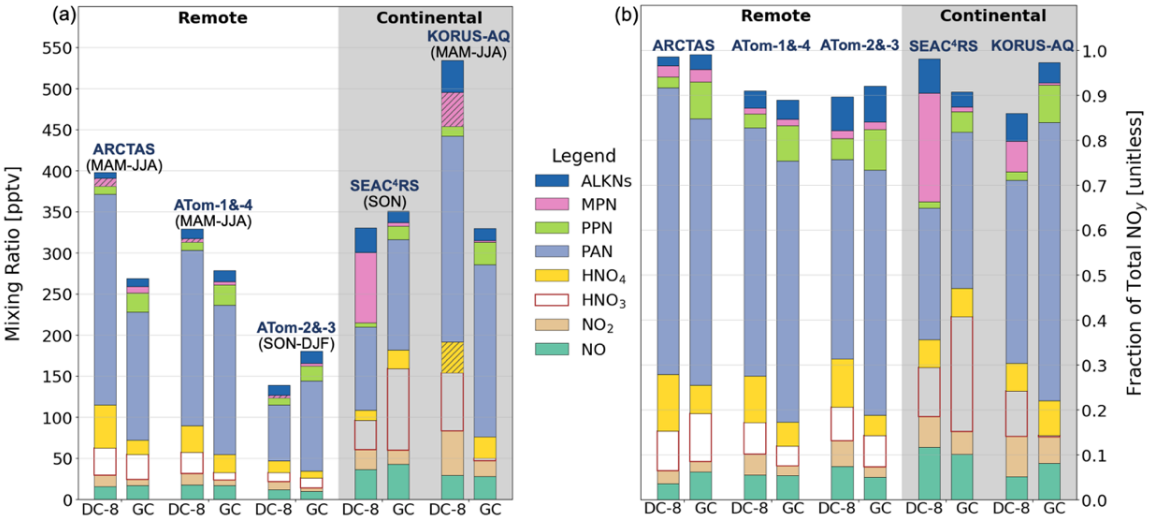

Figure 3. 5: NO_y composition in the upper troposphere along DC-8 flight tracks. Bars are median values of absolute (a) and relative (b) individual NO_y components observed and inferred from the observations during DC-8 campaigns and simulated by GEOS-Chem (GC). Seasons sampled are given below each bar and the grey

shading distinguishes sampling in the remote (no shading) and continental (shaded) UT. Hatchings in (a) indicate inferred concentrations (see text for details).

Inferred DC-8 HNO_4 and PPN in Figure 3.5 use ATom-1 HNO_4 and ATom-4 PPN for combined ATom-1 and -4 components and, similarly, ATom-2 HNO_4 and ATom-3 PPN for combined ATom-2 and -3. KORUS-AQ HNO_4 is estimated to be 37 pptv by multiplying the SEAC^{4}RS median fraction of HNO_4 (HNO_4/NO_y = 0.06) by the KORUS-AQ median NO_y. SEAC^{4}RS is used because HNO_4 is thermally unstable (Ryerson et al., 2000) and so varies with temperature. Mean upper troposphere ambient temperatures for KORUS-AQ (252 K) are more consistent with SEAC^{4}RS (246 K) than the other campaigns (238 K for ARCTAS, 238–241 K for ATom).

The inferred ~ 10 pptv ARCTAS MPN is from the estimate by Browne et al. (2011). KORUS-AQ MPN is estimated by bounding a potential range from two approaches. The first is the median value of the difference between TD-LIF total PNs and the sum of all individual CIMS PANs and our inferred HNO_4 of 37 pptv, yielding MPN = 75 pptv. This likely overestimates MPN, as the CIMS instrument does not measure an exhaustive suite of PANs. Lee et al. (2022) estimated with a box model and KORUS-AQ measurements that unmeasured PANs account for ~ 20 % of total PNs during KORUS-AQ, though this applies to air masses impacted by petrochemical and other anthropogenic VOCs and NO_x emissions. Accounting for these unmeasured PANs yields a lower-bound KORUS-AQ MPN of 8 pptv. The MPN thus inferred for KORUS-AQ is 42 pptv, taken as the midpoint between 8 and 75 pptv, and it accounts for 7 % of KORUS-AQ NO_y. As the GEOS-Chem model MPN is consistent with DC-8 inferred MPN during ARCTAS, I multiply the GEOS-Chem ATom MPN fractions (~ 0.01 for ATom-1 and -4 and ~ 0.02 for ATom-2 and -3) by ATom DC-8 NO_y to infer ATom MPN of < 6 pptv.

Only the C1–C5 ALKNs are shown in Figure 3.5 for ATom. The remote measurements of total ALKNs available from ARCTAS that would be most suitable to assess the likely contribution of longer chain (> C5) ALKNs are on median 5 pptv less than the ATom C1–C5 ALKNs measurements. The ARCTAS total ALKNs measurements are also very noisy, as indicated by a range of −113 pptv to ~ 333 pptv. The range in ARCTAS WAS C1–C5 measurements, by comparison, is 8–29 pptv. Contributions of > C5 ALKNs to total ALKNs for SEAC^{4}RS (~ 50 %) and KORUS-AQ (~ 60 %), representative of the continental upper troposphere, suggest that > C5 ALKNs in remote regions are < 50 % of total ALKNs or < 12 pptv (median of C1–C5 ALKNs for ATom1-4). According to the measurements, remote region C1–C5 ALKNs are dominated by methyl nitrate (C1 ALKN), accounting for 40 % of ATom C1–C5 ALKNs and 49 % for ARCTAS. Second is isopropyl nitrate (C3 ALKN), making up 17 % of ATom C1–C5 ALKNs and 25 % for ARCTAS. The > C3 ALKNs dominate ALKNs in the continental upper troposphere, accounting for 92 % of total ALKNs for SEAC^{4}RS and 71 % for KORUS-AQ. I estimate these as the difference between TD-LIF total ALKNs and the sum of WAS C1-C3 ALKNs.

The sum of KORUS-AQ NO_y components totals 531 pptv, > 130 pptv higher than SEAC^{4}RS, ARCTAS, and ATom-1 and -4, all of which are within a narrow range of 330–400 pptv. Minimum NO_y values are for the remote autumn and winter measurements from ATom-2 and -3 at 141 pptv. Despite the wide range in absolute total and components of NO_y, the relative contribution of many individual NO_y components is consistent across all campaigns. These include NO (7 ± 3 %; mean ± 1σ standard deviation), NO_2 (6 ± 2 %), HNO_3 (9 ± 2 %), HNO_4 (9 ± 3 %), PPN (3 ± 1 %), and ALKNs (5 ± 3 %). PAN, the dominant NO_y component in all campaigns, is least consistent, ranging from 30 %–41 % for the continental upper troposphere to 44 %–64 % for the remote upper troposphere. The HNO_4 fraction (10 %–13 %) in the remote upper troposphere is higher than in the continental upper troposphere (~ 6 %), due to colder temperatures for ATom and ARCTAS. MPN is typically negligible near the surface due to its high thermal instability but can become significant in the colder upper troposphere. During SEAC^{4}RS, MPN accounted for 24% of NO_y, substantially higher than the 2–7% observed in other campaigns. This enhancement is attributed to increased availability of its precursor, CH_3O_2. Unlike other campaigns, the aged air SEAC^{4}RS sampled influenced by lightning, biomass burning, and deep convective transport of surface pollution are enriched with VOCs and NO_x, leading to vigorous photochemistry that enhanced CH_3O_2 production and thus MPN abundance. Aerosol nitrate, pNO_3, absent in Figure 3.5 due to the uncertain sampling efficiency of the chemiluminescence instrument, is at most 4 % for SEAC^{4}RS and KORUS-AQ (Section 3.1), comparable to the contribution from PPN.

The far larger fraction of MPN to total NO_y during SEAC^{4}RS (Figure 3.5b) warrants further investigation, as the relative proportion of MPN to total NO_y ranges from negligible to 100 % (Figure 3.4). If I instead estimate MPN by subtracting the sum of HNO_4 and all PANs measured with the CIMS instrument from the TD-LIF PNs, making the assumption that CIMS measures most PANs, MPN is 49 pptv and the SEAC^{4}RS median contribution to NO_y declines from 24 % to 14 %. This is still at least double the contribution for any other campaign. A small proportion of HNO_4 is measured in the MPN channel of the TD-LIF instrument. This represents about 11 %, according to Nault et al. (2015). For the CIMS median HNO_4 of 12.6 pptv during SEAC^{4}RS, the HNO_4 interference is only 1.4 pptv, so it does not affect the 14 %–24 % contribution.

The NO_y composition information in Figure 3.5 has a Northern Hemisphere sampling bias to achieve coincidence. ATom observations south of the Equator exhibit a similar seasonal pattern to the Northern Hemisphere: summer > spring > autumn > winter NO_y, except that the Southern Hemisphere spring and summer NO_y differ by ~ 90 pptv, whereas there is a near-negligible difference for the Northern Hemisphere (Figure 3.1). As with the Northern Hemisphere, PAN accounts for most Southern Hemisphere NO_y, ranging from ~ 32 % for ATom-1 (July–August) to ~ 42 % for ATom-2 (January–February).

Nighttime-dominant NO_y compounds N_2O_5, NO_3, and HONO are not included in Figure 3.5, as these have near-negligible daytime abundances. Of these, there are only measurements of N_2O_5, limited to ATom-3 and -4, that represent ~ 0.1 % of upper tropospheric NO_y along the daytime ATom flight tracks in Figure 2.1 (Section 2.1.1). NO_3 has a lifetime of a few seconds during the day, due to efficient photolysis (Brown& Stutz, 2012). HONO also rapidly photolyses with a near-surface lifetime of 15 min (Sörgel et al., 2011). Photolysis of HONO would be further enhanced (by ~ 50 % at 390 nm) in the upper troposphere where photolysis frequencies are enhanced (Hofzumahaus et al., 2002; Reed et al., 2016a).

3.3 Contemporary Understanding of UT NO_y

GEOS-Chem Northern Hemisphere upper troposphere NO_y is compared to the observations in Figures 3.1 and 3.5. In Figure 3.1, GEOS-Chem median NO_y is less than DC-8 in summer and spring by ~103 pptv, similar to DC-8 in autumn, and greater than DC-8 in winter by ~60 pptv. As a result of these differences in absolute NO_y, the model underestimates the IAGOS and DC-8 seasonal shifts in NO_y from winter to spring and from summer to autumn.

The sum of the GEOS-Chem fractional contributions of NO_y components in Figure 3.5(b) that does not equal to 1 are because the model NO_y budget also includes components not measured during DC-8, such as MPAN and halogenated ALKNs. Consistent across all campaigns is model underestimate in NO_2 and overestimate in PPN. The model version I use does not include photolysis of PPN, even though this is known to occur (Harwood et al., 2003). PPN photolysis rather than thermal decomposition is the dominant loss pathway of PPN in the cold UT. PPN photolysis is scheduled for inclusion in a later model version (version 14.5) than is used here (Horner et al., 2024), prompted by my findings that it is systematically overestimated in the UT. Inclusion of PPN photolysis would liberate up to ~16 pptv NO_2, resolving the 10-16 pptv model underestimate in NO_2. Other studies have addressed model biases in NO_2 by including photolysis of pNO_3 forming HONO that rapidly photolyzes to NO_x (Shah et al., 2023). Aerosol Nitrate concentrations are too small in the UT for this to be a substantial NO_2 source. Aerosol Mass Spectrometer (AMS) measurements of pNO_3 are on median ~0.01 $\mu g\ m^{-3}$

during ARCTAS, ~0.07 μg m^{-3} during KOUS-AQ, ~0.04 μg m^{-3} during SEAC^{4}RS and <0.01 μg m^{-3} during ATom.

The model exhibits significant campaign-specific biases in total NO_y for ARCTAS (129 pptv underestimate), KORUS-AQ (205 pptv underestimate), ATom-1 and -4 (51 pptv underestimate) and ATom-2 and -3 (42 pptv overestimate). The model underestimate in ARCTAS NO_y is due mostly to a ~100 pptv low bias in PAN and, to a lesser extent, a 35 pptv underestimate in HNO_4. The model bias for ATom-2 and -3 is due almost entirely to PAN. For KORUS-AQ, all NO_y components except PPN are underestimated, indicative of an overall underestimate in reactive nitrogen sources to the UT over this region. The ATom-1 and -4 underestimate in NO_y is due mostly to a low model bias in PAN and HNO_3. Overall, the model underestimates the contrast between remote and continental UT NO_y.

GEOS-Chem simulates individual C1-C3 ALKNs, but most >C3 ALKNs are included as a lumped species. There are other >C3 ALKNs represented individually in the model, such as those formed from isoprene oxidation (Fisher et al., 2016), but abundances of these are near-negligible in the UT. DC-8 C1 ALKN is only 4% of ALKNs for SEAC^{4}RS and 11% for KORUS-AQ, whereas in the model these are a much greater component of ALKNs: 40% for SEAC^{4}RS and 29% for KORUS-AQ. Modelled >C3 ALKNs are a far smaller portion of total ALKNs (29% for SEAC^{4}RS and 23% for KORUS-AQ) than the observations (Section 3.2). Modelled C1 ALKN concentrations are consistently less than the observed values by ~2 pptv for ARCTAS and ~1 pptv for ATom. Modelled C3 ALKN is ~1 pptv less than the observations for ARCTAS, but ~1 pptv more than the observations for ATom.

The sum of measured and modelled individual NO_y components are not significantly different for SEAC^{4}RS, though the model overestimates HNO_3 by 64 pptv and underestimates MPN by 81 pptv. The model low bias in MPN suggests that the model underestimates influence of NO_x and reactive VOCs sources on aged air over source regions with a mix of emissions from fires and lightning, and deep convective injection of surface pollution. The model high bias in HNO_3 could be because of a factor of 2 model overestimate in H_2O_2 compared to observed H_2O_2 for SEAC^{4}RS. An overestimate in H_2O_2 indicates a model overestimate in HO_2 that promotes formation of HNO_3 and that would also account for the ~10 pptv overestimate in modelled HNO_4. Modelled HO_2 is used to calculate PSS NO_2 for SEAC^{4}RS (Equation (1), Section 2.1), but this only imparts a small high bias (~1.7 pptv) in SEAC^{4}RS PSS NO_2. Model bias in H_2O_2 over ARCTAS (>100 pptv) may also be the cause for the model underestimate in ARCTAS HNO_4 of ~35 pptv.

Modelled KORUS-AQ HNO_3, ALKNs, and MPN are all biased low. The low biases in these NO_y components may be because of a general underestimate in NO_y sources over South Korea. The region has large anthropogenic NO_x and VOCs sources that are represented in the model with a global inventory (CEDS) that may not suitably account for local emissions (Travis et al., 2024). Lightning NO_x emissions could also be underestimated in the heavily parameterized inventory in GEOS-Chem (Murray et al., 2012; Marais et al., 2018). But this is a challenging NO_x source to evaluate over locations that include other prominent sources of NO_x.

The model biases identified in this study hinder accurate assessments in several key areas. These include the radiative effect of tropospheric ozone for short-term climate impact evaluations; the oxidative capacity of the troposphere, which constrains estimates of methane lifetime and persistence; retrievals of tropospheric NO_2 column densities from space-based UV–visible instruments that rely on modelled vertical NO_2 profiles; estimates of NO_x emissions derived from comparisons between modelled and observed oxidized nitrate wet deposition fluxes, which depend on soluble HNO_3 abundance; and evaluations of nitrogen deposition impacts on vulnerable ecosystems.

4: Top-down Estimates of NO_x Emissions for Hotspots across Sub-Saharan Africa

This chapter is organised into three main parts. It begins by presenting the top-down estimates of NO_x emissions and lifetimes for isolated hotspots in Sub-Saharan Africa, derived using the wind rotation and EMG fit approach. The second part assesses these estimates by comparing them with the global CEDSv2 emission inventory (Section 2.2.2), including a scaling of CEDSv2 to match the top-down results and subsequent evaluation of tropospheric NO_2 columns from the GEOS-Chem model against TROPOMI observations. The chapter ends by further evaluating the top-down NO_x emissions through comparisons with a regional African inventory and an inventory developed to support air quality priority areas in South Africa.

4.1 Top-down NO_x Emissions and Lifetimes

Figure 4.1 shows number of successful fittings for targeted 28 hotspots. Of the 28 hotspots selected in Figure 2.2, 20 yielded successful EMG fits and 12 out of 20 have more than 10 successful fits. The number of successful EMG fits in Sub-Saharan Africa is lower than the number in high-concentration Asia hotspots. According to Lu et al. (2025), success of deriving NO_x emissions increased from about half of all potential hotspots using a single sampling area to all hotspots using 54 sampling areas for hotspots in Asia. The success rate is lower in Sub-Sharan Africa, due to the much smaller enhancements in NO_2. 8 out of 28 hotspots in low-concentration Sub-Saharan Africa failed to produce EMG fits, due to insufficient distinction between the plume and background NO_2.

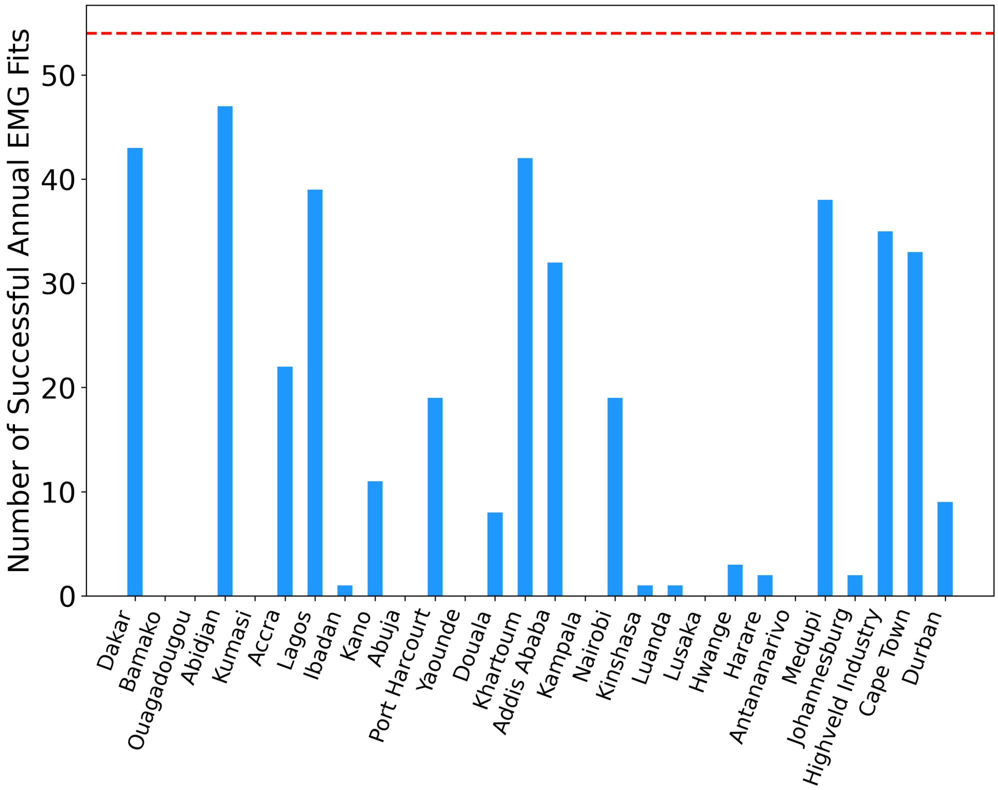

Figure 4. 1: Number of Successful EMG fits for the targeted 28 hotspots. The red dashed line shows the maximum number of fits that can be achieved (54).

Figure 4.2 shows NO_x emissions and effective lifetimes for hotspots in Sub-Saharan Africa estimated using wind rotation and the EMG fit. The 20 hotspots that yielded successful EMG fits include 18 cities, the Medupi-Matimba combined power plants hotspot, and the industrial Highveld. NO_x emissions in South African hotspots (28–130 mol/s) are significantly greater than those in the rest of Sub-Saharan Africa (<28 mol/s). Emissions range from ~2 mol/s for Ibadan (Nigeria), to 75 mol/s for Johannesburg, and up to 130 mol/s for the Highveld industrial area in South Africa. Effective lifetimes that are dominated by dispersion and include some loss due to chemical processing in the plume are within 1 to 10 hours for all hotspots. The longest lifetime is 10 hours for the Highveld region that has the largest plume size, followed by Medupi and Johannesburg (Jhb). The shortest lifetime of ~1 h is for the small Hwange (Zimbabwe) plume. Durban also exhibits a short lifetime, though it is a mid-sized plume. This is likely because it is a coastal city with greater wind speeds than other locations.

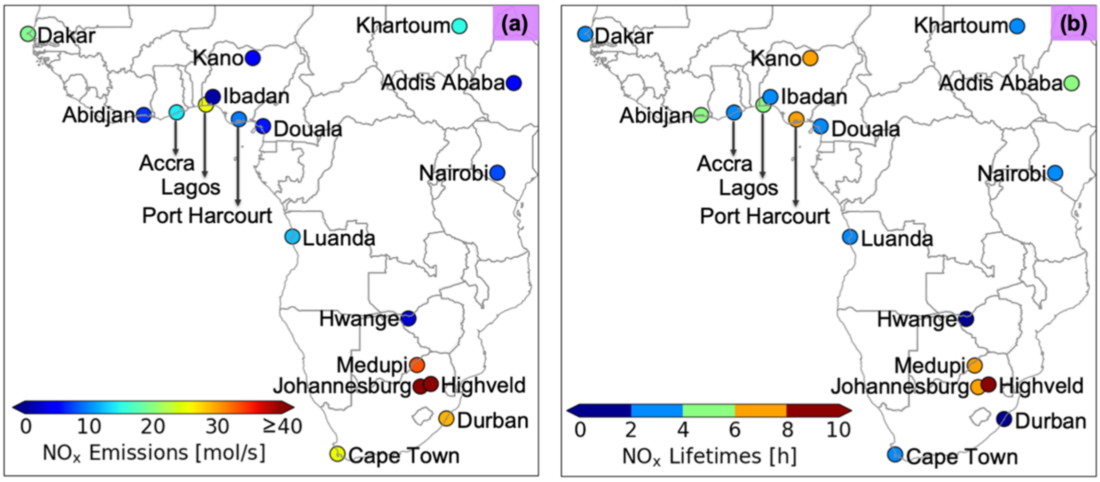

Figure 4. 2: Top-down NO_x emissions (a) and effective lifetimes (b) for the 18 hotspots in Sub-Saharan Africa with successful EMG fits.

Figure 4.3 compares the annual NO_x emissions from this study with values from previous studies that used similar sampling periods and a single sampling area. These include emissions from Lange et al. (2022) based on select days of TROPOMI data (2018–2020) and multiyear (2017–2019) mean emissions from Goldberg et al. (2021b), derived from OMI data. As shown in Figure 4.3

(a), Lange et al. (2022) reported NO_x emissions for five of the 18 cities of this study: 5.0 mol/s (equivalent to 7.3 gigagram per year (Gg/y)) for Hwange, 5.1 mol/s (7.4 Gg/y) for Kano, 16.9 mol/s (24.5 Gg/y) for Khartoum, 30.9 mol/s (44.8 Gg/y) for Lagos and 55.5 mol/s (80.5 Gg/y) for Medupi. From Goldberg et al. (2021b), NO_x emissions (in Gg/y) were extracted from their figures and the midday NO_x emissions were calculated via dividing by 0.77, their midday to 24h scaling factor. Goldberg et al. (2021b) reported NO_2 emissions for four of the 18 cities: 14 Gg/y for Abidjan, 18 Gg/y for Dakar, 18 Gg/y for Khartoum and 35 Gg/y for Cape Town. These reported NO_2 emissions in Gg/y are converted to NO_x emissions in mol/s to compare with emissions estimated in this study, as shown in Figure 4.3 (b). The estimated NO_x emissions derived in this study for the same cities are equivalent to 4 Gg/y for Hwange, 6 Gg/y for Kano, 20 Gg/y for Khartoum, 34 Gg/y for Lagos, and 44 Gg/y for Medupi (Figure 4.3 (a)), and 9 Gg/y for Abidjan, 26 Gg/y for Dakar, and 34 Gg/y for Cape Town (Figure 4.3 (b)).

On average, the estimated emissions are ~28% less than those reported by Lange et al. (2022) and ~14% less than those by Goldberg et al. (2021b) . The smaller error estimates in Lange et al. (2022) reflect their limited propagation of uncertainties, which include only wind speed and EMG fit contributions. For these comparisons, the largest difference is for Medupi, where my annual mean NO_x emissions represent the combined Medupi and Matimba power plant region. This difference could be due to differences in sampling days for a power plant that operates intermittently. Differences in sampling periods and NO_2 column products used may also contribute. Goldberg et al. (2021b) used OMI data, while Lange et al. (2022) relied on an earlier TROPOMI product with a known low bias in NO_2 VCDs over polluted areas (van Geffen et al., 2020). Overall, the absence of significant discrepancies beyond the 1.5:1 to 0.5:1 range indicates that the multiple area sampling approach I use is consistent with the traditional approach of using a single sampling area.

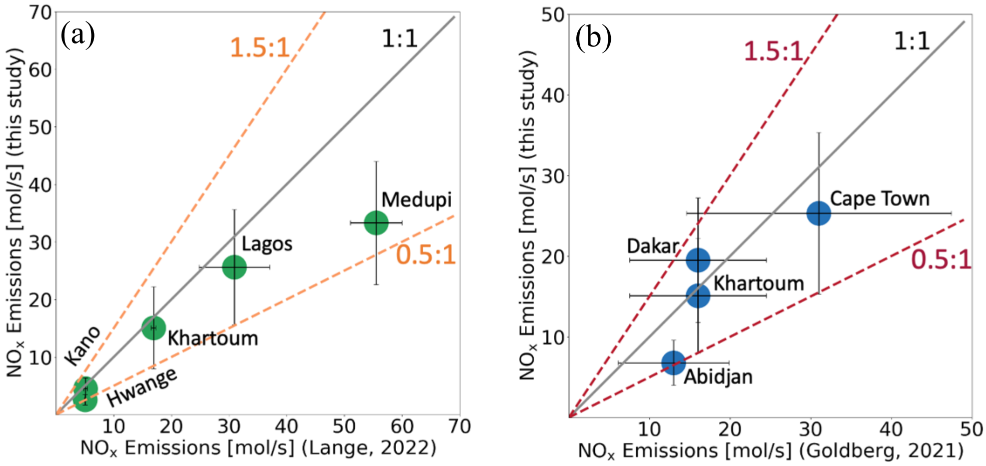

Figure 4. 3: Comparison of my and past top-down NO$_x$ emissions. Symbols compare the estimated emissions in this study to those from Lange et al. (2022) (green) and Goldberg et al. (2021b) (blue). Error bars are overall uncertainties for my study (Section 2.2.1), the same 53% uncertainty applied to all cities by Goldberg et al. (2021b) and the city-specific uncertainties for Lange et al. (2022).

4.2 Assessment of Top-down Emissions with GEOS-Chem and TROPOMI

I scale the CEDSv2 NO$_x$ emissions in GEOS-Chem to match estimated top-down emissions in Figure 4.2 (a) for 18 of the 28 hotspots shown in Figure 2.2. This decreases the total NO$_x$ emissions for these hotspots from ~21 kilograms/s in the default CEDSv2 to ~9 kilograms/s in the scaled CEDSv2. The major change results from a substantial decrease in the largest hotspots, Johannesburg, and the Highveld, from ~6.3 kilograms/s to ~1.9 kilograms/s for Johannesburg and from ~9.4 kilograms/s to ~3.2 kilograms/s for the Highveld. The major emission hotspot that increases is the hotspot encompassing the Medupi and Matimba power plants. Medupi is a recently constructed power plant. It is the largest global dry-cooled coal-fired power plant in the world and is also funded by the World Bank (Rafey& Sovacool, 2011). This source is missing in the CEDSv2 emission inventory. Adding it increases emissions for this hotspot from 0.03 kilograms/s to 0.7 kilograms/s.

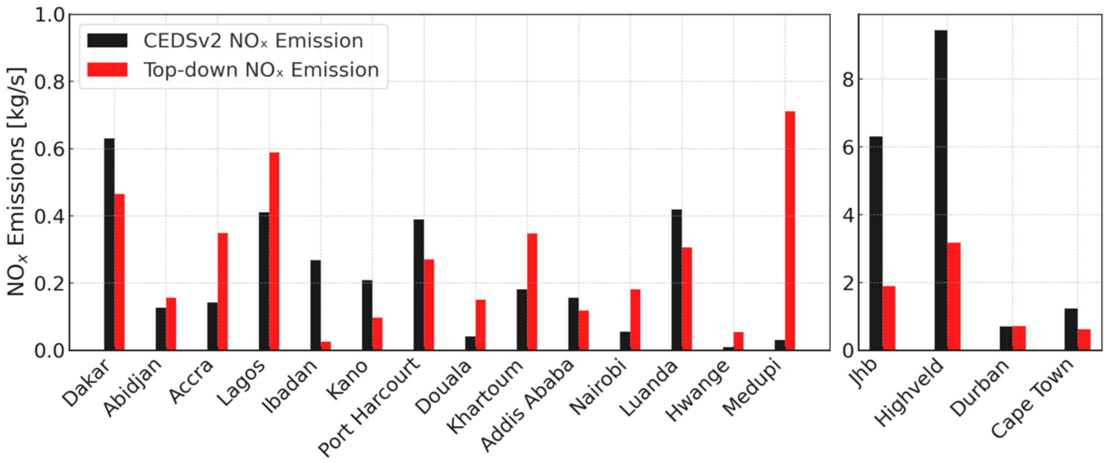

Figure 4. 4: Top-down total NO_x emissions scaling of the CEDSv2 bottom-up inventory. Bars are the original (black) and scaled (red) CEDSv2 emissions for target hotspots in 2019.

There are also emission hotspots in CEDSv2 that TROPOMI does not observe, suggesting a spatial misattribution of emissions. There is a hotspot in the model that occurs on the western edge of the Sudan nested domain (domain (c) in Figure 2.4) that does not exist in TROPOMI and that totals ~0.58 kg/s in CEDSv2. Another is an NO_2 enhancement in the model that in CEDSv2 totals ~0.27 kg/s that appears to have been allocated to Hwange National Park (hotspot south of the TROPOMI hotspot in nested domain (g) in Figure 2.4) rather than the Hwange urban centre north of the park in Zimbabwe. Another stray hotspot in CEDSv2 totalling 0.014 kg/s occurs due north of the Medupi/Matimba hotspot on the Botswana side of the border with South Africa (domain (h) in Figure 2.4). This hotspot is further north than Gaborone, the capital city of Botswana. I instead set the western Sudan, Hwange Park, and southern Botswana stray hotspots to typical anthropogenic NO_x emissions for rural areas of 0.002 kg/s. These are updated and the scaled CEDSv2 inventory emissions are then fed to the GEOS-Chem model.

Figure 4.5 compares tropospheric NO_2 vertical column densities obtained from TROPOMI and GEOS-Chem driven with the default and scaled CEDSv2 anthropogenic NO_x emissions. The comparison is of data sampled 200 km × 250 km around the centre of each hotspot and with background NO_2 removed

(Section 2.2.2). The NO_2 column densities simulated by the scaled model are on average 5 × 10^{15} molecules cm^{-2} less than those of the original GEOS-Chem model, due mostly to the decrease in emissions in northeast South Africa. For the Johannesburg and Highveld hotspots, there is significant improvement in the agreement of modelled and observed NO_2 column densities after scaling CEDSv2 down by ~65%.

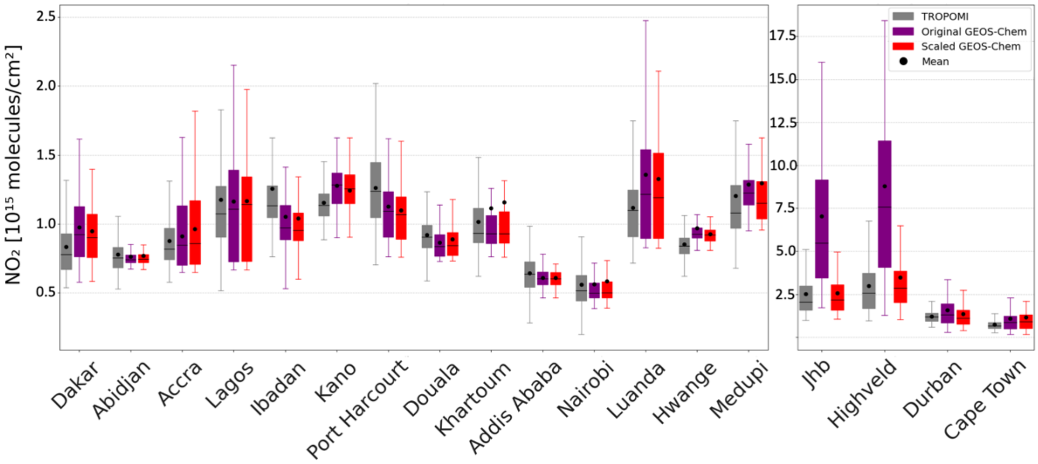

Figure 4. 5: Comparison of tropospheric NO_2 vertical column densities from TROPOMI, the original GEOS-Chem, and the scaled anthropogenic NO_x emissions informed GEOS-Chem. Data are averages obtained $2^0 \times 2.5^0$ around each of the 18 hotspots and with background NO_2 contribution removed (see Section 2.2.2).

4.3 Assessment of Bottom-up Emission Inventories

Figure 4.6 compares NO_x emissions for hotspots in Northeast South Africa from top-down estimates of this study and from a regional bottom-up inventory. The distribution of NO_x emissions in tonnes per year per cell ($0.06^0 \times 0.06^0$) for 2019 from the bottom-up inventory are in Figure 4.6 (a). It covers the Medupi, Jhb, Highveld and Durban hotspots. The total NO_x emissions in Gg/y for each hotspot are the sum of emissions within 50 km radius of the centre of each hotspot. The bottom-up emissions of Medupi and the Highveld exceed the estimated top-down emissions by more than 260 Gg. A few cells with extremely high NO_x emissions (>100 Gg/cell) within the Highveld area in the bottom-up inventory are main contributors to the large difference between the top-down and bottom-up estimates. The exact cause for these very large emissions is unclear and challenging to resolve. The majority of the sources are large industrial stacks, and the bottom-up inventory is informed by CEMS measurements of emissions (also observationally derived), so such a large difference is a surprise, but is consistent with my comparison of the top-down estimates to the global CEDSv2 inventory in Figure 4.4.

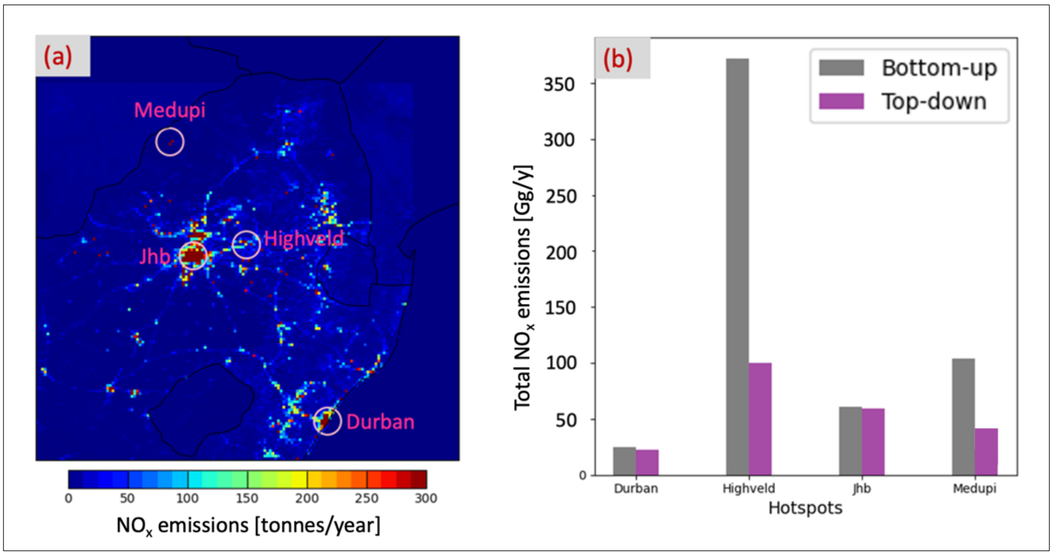

Figure 4. 6: Comparison of total NO_x emissions for 2019 between top-down estimates and the northeast South Africa bottom-up inventory. (a) is bottom-up total NO_x emissions distribution with pink circled four hotspots and each is within 0.5°. (b) is paired bars of total NO_x emissions of top-down and bottom-up for each hotspot in (a).

Figure 4.7 compares bottom-up DACCIWA NO_x emissions for 2018 and the estimated top-down 2019 NO_x emissions for 18 hotspots. Like the comparison in Figure 4.4 and 4.6, the South Africa large hotspot emissions are much greater in the bottom-up inventory than my top-down estimates. These differ by ~14 kg/s for the Highveld and ~13 kg/s for Johannesburg. These differences are larger than the maximum ~14% variation that could result from annual growth at the fastest rates estimated by Vohra et al. (2022).

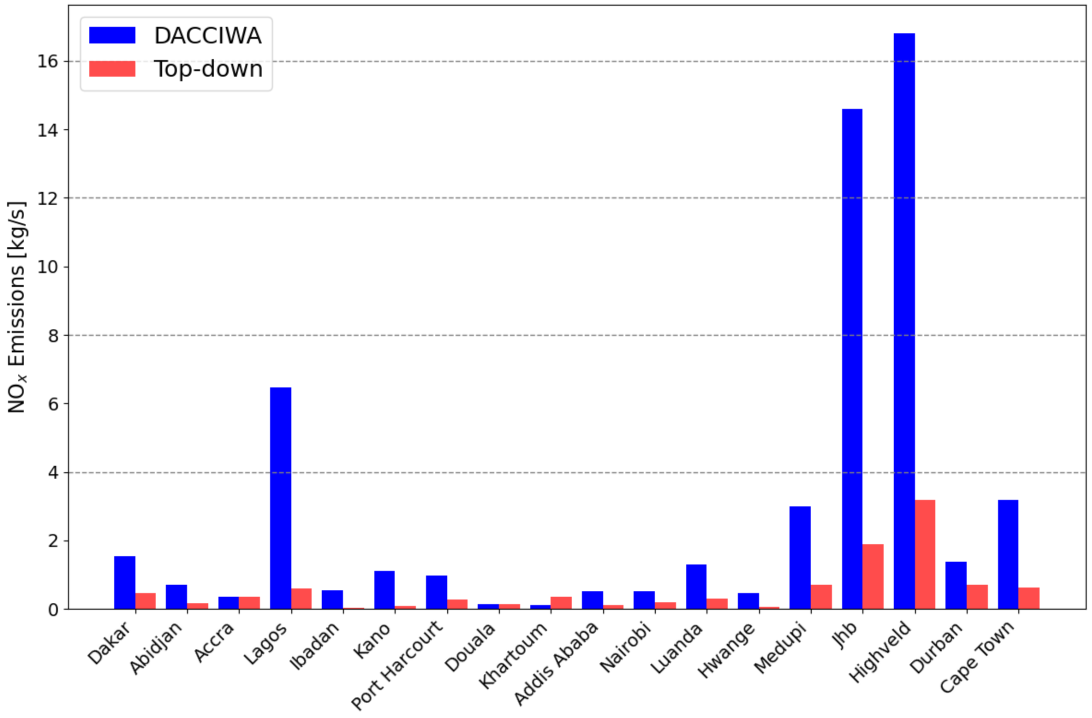

Figure 4. 7: Comparison of my and the regional DACCIWA emission inventory hotspot NO_x emissions. Bars are top-down (red) for 2019 and bottom-up (blue) for the most recent year available, 2018.

The bottom-up inventories with high bias of NO_x emissions would result in high bias in model estimates of tropospheric ozone, aerosol nitrates, surface pollution of $PM_{2.5}$ and ozone, and nitrogen deposition to sensitive habitats. The top-down NO_x estimates here help scale bottom-up inventories and improve projections of future emissions of NO_x for these hotspots. This is especially pertinent for the region of focus, as many target hotspots are amongst the fastest growing urban areas in the world (Yuen& Kumssa, 2011).

The assessment of top-down NO_x emissions also provides insights into potential errors in our understanding of both anthropogenic and natural sources of NO_x emissions and abundances in the under-sampled Africa, as represented in the model. Furthermore, the evaluation against regional and updated emission inventories highlights discrepancies that should be addressed in future research.

5: Conclusions

5.1 Summary and Key Findings

To achieve my first PhD research aim, I used NASA DC-8 aircraft measurement data from the ARCTAS, SEAC^{4}RS, KORUS-AQ, and ATom campaigns to characterize reactive nitrogen (NO_y) in the global upper troposphere. This followed confirmation from comparison to routine reactive nitrogen measurements from the IAGOS commercial aircraft campaign that DC-8 has the same seasonality of peak NO_y in summer and spring and minimum NO_y in winter in the northern hemisphere along the heavily sampled North Atlantic flight corridor. Consistency supports use of DC-8 campaign data to characterise NO_y under standard daytime conditions.

I also confirmed that most (78-99%) NO_y components were measured during DC-8 campaigns. These include nitrogen oxides (NO_x), and inorganic (HNO_3 and HNO_4), and organic (PANs, MPN, and alkyl nitrates) reservoirs of NO_x. PAN is the dominant NO_y component for all campaigns (30-64%), followed by NO_x (6-18%). The relative contribution of most other components is similar across all campaigns, except for MPN that is ~24% of NO_y for SEAC^{4}RS over the southeast US and much less (2-7%) for all other campaigns, though the latter range is from inferred concentrations of MPN.

Then to meet the **second research aim**, I used the GEOS-Chem model sampled along the DC-8 flight tracks to assess the state of knowledge of upper tropospheric NO_y. Consistent model biases for all campaigns include an overestimate in PPN and underestimate in NO_2. The model lacks PPN photolysis that would address the PPN model bias and mostly resolve the NO_2 bias. In the continental upper troposphere, the model underestimates total NO_y for KORUS-AQ, but reproduces total NO_y for SEAC^{4}RS, though with too much HNO_3 and too little MPN. Over remote regions, the model biases are less severe, and are likely related to the weak seasonal variability in total NO_y in comparison to DC-8 and IAGOS. A possible cause of this is errors in model representation of maritime lightning NO_x emissions that influence NO_y abundance in spring and summer.

My results underscore the need for sustained measurements of upper tropospheric reactive nitrogen for further refinement of knowledge of upper tropospheric NO_y sources, dispersion, and chemical processing. This is crucial for advancing our understanding of the global nitrogen cycle and its broader environmental implications.

My **third research aim** was achieved by successfully deriving top-down annual NO_x emissions for 20 hotspots in Sub-Saharan Africa for 2019 by applying a recently developed, near-automated, multi-sampling-areas EMG method and wind rotation to TROPOMI NO_2 vertical column densities. These top-down NO_x emissions I then used to evaluate a local bottom-up emissions inventory of northeast South Africa covering four hotspots, including the two greatest in Sub-Saharan Africa. The hotspots of the industrial Highveld and of the combined power plants Medupi and Matimba are very different from the top-down estimates and are consistently much greater in other regional and global bottom-up emission inventories than the top-down approach. Further research is needed to determine the exact cause, as such large differences impede the development of effective air quality policies.

My **fourth and final research aim** was completed by validating my top-down NO_x emissions estimates by comparing TROPOMI NO_2 columns densities to two GEOS-Chem simulations that include one with default CEDSv2 emissions and the other scaled to match the top-down emissions. This quasi-independent approach (so named, because TROPOMI NO_2 is also used to derive top-down hotspot emissions) offers the option to assess top-down estimates in the absence of reliable bottom-up emission inventories that are available in regions like the US, Europe, and China.

My results ensure credibility of the top-down estimates by validation using both observations and model simulations. The large differences between top-down and bottom-up emission inventories in data deficit region Sub-Saharan Africa highlight the need for future research in addressing the discrepancies, advancing emission inventories used in modelling surface air pollutants and assessing air pollution exposures. This is crucial for regulations suggestions in fast developing urban areas in Sub-Saharan Africa.

My results strengthen the credibility of top-down emission estimates by applying a quasi-independent validation approach. The substantial discrepancies between top-down and bottom-up emission inventories in a data-deficit region like Sub-Saharan Africa highlight the need for further research to reconcile these differences and update emission inventories for air quality modelling. This is crucial for shaping effective regulatory strategies in the rapidly developing urban areas of Sub-Saharan Africa.

5.2 Significance and Implications

The findings of this thesis are significant in several ways. First, they advance the fundamental understanding of reactive nitrogen speciation and distribution in the global upper troposphere, a region that plays a critical role in controlling ozone formation, methane lifetime, and the radiative balance of the atmosphere. A more complete representation of NO_y, including previously under-considered species such as MPN, helps to capture the full chemical speciation, provides observational constraints on abundances, and reduces model biases. This in turn can enhance chemical transport modelling and strengthen climate assessments that depend on accurate simulations of ozone and atmospheric oxidising capacity. Importantly, this work highlights the role of MPN, a compound that has received little attention in the past due to its thermal instability. Here, I present the first observational and estimated evidence of MPN abundance in the global upper troposphere and its contribution to the total reactive oxidised nitrogen budget. MPN levels can account for up to 24% of NO_y (albeit with high uncertainty), substantially higher than current model simulations suggest. This discrepancy implies that our understanding of NO_x redistribution, as influenced by the composition of NO_y, requires further attention. These results emphasise the need for continued investigation of organic nitrates to improve our understanding of nitrogen cycling in the atmosphere.

Second, the top-down NO_x emissions derived for Sub-Saharan Africa provide some of the first robust, observation-based estimates for a region where air quality concerns are rising rapidly alongside urbanisation and industrialisation. The discrepancies revealed between top-down and bottom-up inventories highlight weaknesses in current emission estimates and demonstrate the risks of relying solely on bottom-up emission inventory-based modelling in regions with sparse ground-based data. This matters because such inventories are often used to guide regulatory decisions, assess health burdens, and shape climate policy.

By bridging observational data and modelling frameworks, this work provides a methodological template for other under-sampled regions. In doing so, it helps close the knowledge gap between well-monitored regions such as North America and Europe, and those where emissions data remain limited despite growing environmental and health concerns.

5.3 Limitations Motivating Future Work

This work has characterised reactive nitrogen sources and abundances in under-sampled regions of the world, specifically the global upper troposphere and sub-Saharan Africa. Several limitations constrain the interpretation of the findings. These limitations define clear priorities for future research that are essential to improving the representation of NO_y and its role in atmospheric composition.

1. Limitations in DC-8 Observational Coverage

Most NASA DC-8 aircraft campaigns are concentrated in the Northern Hemisphere, and even the pole-to-pole, multi-season ATom campaigns provided limited sampling in the Southern Hemisphere. This restricts interhemispheric comparisons, despite the stronger influence of remote background conditions in the Southern Hemisphere and anthropogenic emissions in the Northern Hemisphere. Future work needs to expand observational coverage in the Southern Hemisphere to build a more balanced global picture of NO_y.

2. DC-8 Campaigns Measurement Limitations

The KORUS-AQ campaign revealed a large model underestimate of NO_y, but the absence of HNO_4 measurements and limited coverage of peroxyacyl nitrates (only a subset of PAN species measured) prevented robust diagnosis. Since PANs and other organic nitrates are important reservoirs of NO_x, future aircraft campaigns are suggested to include more comprehensive suites of these compounds. The DC-8 flight ceiling of 12 km limited sampling in the tropics, where the upper troposphere extends to ~16 km. This likely underestimated contributions from lightning NO_x, which are particularly important in tropical regions. Higher-altitude platforms are needed to capture the full vertical distribution.

3. Model–observation Discrepancies

Discrepancies between DC-8 aircraft observations and GEOS-Chem simulations highlight important gaps in our current representation of upper-tropospheric reactive nitrogen. In particular, methyl peroxynitrate (MPN) was consistently observed at much higher abundances than simulated, pointing to incomplete or missing treatment of organic nitrate chemistry in the model. This mismatch has direct implications for estimating tropospheric ozone, as accurate representation of NO_y is essential for constraining ozone formation and oxidising capacity. However, with the observations available in this study, it was not possible to diagnose the mechanisms underlying these discrepancies in detail. Addressing them will require a combination of approaches. Laboratory experiments are needed to quantify the kinetics and reaction pathways controlling the formation and decomposition of MPN and other organic nitrates. Dedicated ambient measurement campaigns need to be designed to capture a more comprehensive suite of volatile organic compounds (VOCs) and the peroxy radicals generated from their oxidation, both of which are key precursors to MPN. Linking such laboratory and field evidence would allow models like GEOS-Chem to incorporate more realistic pathways for MPN production and loss. With this improved mechanistic understanding, it would then be possible to assess where, beyond the southeast U.S. upper troposphere, MPN contributes significantly to the reactive nitrogen budget and how it shapes the long-range transport of NO_x and the methyl peroxy radical. Ultimately, reducing these discrepancies is critical for improving estimates of upper-tropospheric ozone and better constraining the role of reactive nitrogen in atmospheric chemistry.

4. Limitations of NO_x Emissions Inventories

Biomass burning emissions in Sub-Saharan Africa represent a major source of uncertainty in regional and global modelling. In GEOS-Chem, simulations based on GFED4s attribute a large contribution of tropospheric NO_2 columns to open biomass burning, but these emissions are far greater than those observed by the TROPOMI instrument. This discrepancy inflates the simulated background contribution to hotspots, making it difficult to evaluate whether updates to inventories such as CEDSv2 that scaled to match top-down hotspot emissions have genuinely improved model performance. The problem is particularly acute when evaluating very small hotspots, where the overestimated background dominates the signal. A more promising way forward is to adopt the Global Fire Assimilation System (GFAS; (Kaiser et al., 2009; Kaiser et al., 2012) that reports approximately three times lower NO_x emissions than GFED4s and is more consistent with satellite observations. Regional inventories introduce additional challenges: for example, the South African inventory currently lacks peer-reviewed documentation or a detailed methodological report, making it difficult to identify the specific factors such as activity data, emission factors, or mapping of mobile sources that drive discrepancies with observations. Although I worked directly with the inventory developer to resolve these issues, we were unable to isolate the causes of the differences. This highlights the need for inventories to be more systematically documented and supported with methodological detail so that discrepancies can be diagnosed and addressed in future work.

5. Methodological Constraints

The exponentially modified Gaussian (EMG) method provided a useful near-automated approach for deriving hotspot emissions from satellite observations, but it is currently limited by its inability to account for the seasonality of NO_x photochemistry. As a result, the method can only provide reliable estimates of annual emissions. This constrains the analysis to total yearly emissions, rather than capturing how emissions vary from month to month. If detailed temporal information were incorporated, the EMG method could enable monthly estimates of NO_x emissions, which would allow variability to be linked directly to human activities (e.g., agricultural burning, fuel use, or waste disposal) and environmental factors (e.g., seasonal vegetation cycles or meteorology). Such an advance would significantly improve the ability of inventories to reflect the dynamics of NO_x emissions.

Beyond NO_x, the EMG method has potential to be extended to other trace gases observable from space, such as formaldehyde (HCHO) and ammonia (NH_3). However, each presents specific challenges. HCHO is partly a primary emission but is also formed secondarily from the oxidation of reactive volatile organic compounds (VOCs), so top-down constraints on HCHO would reflect a mix of direct emissions and VOC precursors. NH_3, by contrast, is a primary emission but partitions reversibly between the gas and aerosol phases, meaning that the current simple EMG framework would require modification to capture this behaviour.

Despite these challenges, extending EMG analysis to HCHO and NH_3 would be particularly valuable for Sub-Saharan Africa, HCHO in this region is emitted from biogenic sources such as isoprene as well as anthropogenic sources including gas flaring and inefficient combustion of solid and liquid fuels. NH_3, on the other hand, is less dominated by agricultural fertiliser use than in other regions, due to relatively low usage of synthetic nitrogen fertilisers, and instead is strongly influenced by inefficient combustion processes such as open waste burning, charcoal production, and other small-scale sources (Keita et al., 2021; Marais& Wiedinmyer, 2016). Satellite observations already available from the IASI instruments (NH_3, morning overpass) and TROPOMI (HCHO) provide an opportunity to apply the EMG framework in this region. With appropriate adaptation, these data could offer much-needed top-down constraints on emissions, helping to reduce uncertainties in inventories.

6. Summary of Future Work Priorities

Future work is therefore suggested to focus on expanding aircraft observations, particularly in the Southern Hemisphere and the tropical upper troposphere, and on including more comprehensive measurement suites in campaigns, such as PANs, HNO_4, VOCs, and peroxy radicals. In parallel, laboratory and field studies are needed to better constrain the chemistry of MPN. while the adoption of more proper biomass burning inventories such as GFAS, together with greater information in recently updated regional inventories, would help reduce uncertainties in emissions estimates. Methodological improvements are also required, particularly refining the EMG approach to incorporate seasonality, and extending its application to additional trace gases. Addressing these limitations will enhance the representation of reactive nitrogen in models, thereby enabling more accurate assessments of ozone, methane lifetime, and the broader role of reactive nitrogen in climate and air quality.

Bibliography

Adedini, S. A. (2022). Population Dynamics, Urbanisation and Climate Change in Africa's Intermediate Cities: What Can Family Planning Contribute? *The Journal of Population and Sustainability*. doi:10.3197/jps.63799953906860

Aghedo, A. M., Bowman, K. W., Worden, H. M., Kulawik, S. S., Shindell, D. T., Lamarque, J. F., Faluvegi, G., Parrington, M., Jones, D. B. A., & Rast, S. (2011). The vertical distribution of ozone instantaneous radiative forcing from satellite and chemistry climate models. *Journal of Geophysical Research, 116*(D1). doi:10.1029/2010jd014243

Akimoto, H., & Tanimoto, H. (2021). Review of Comprehensive Measurements of Speciated NOy and its Chemistry: Need for Quantifying the Role of Heterogeneous Processes of HNO3 and HONO. *Aerosol and Air Quality Research, 21*(2), 200395. doi:10.4209/aaqr.2020.07.0395

Allen, H. M., Crounse, J. D., Kim, M. J., Teng, A. P., Xu, L., & Wennberg, P. O. (2021). ATom: In Situ Data from Caltech Chemical Ionization Mass Spectrometer (CIT-CIMS), V2. In: ORNL Distributed Active Archive Center.

Amos, H. M., Jacob, D. J., Holmes, C., Fisher, J. A., Wang, Q., Yantosca, R. M., Corbitt, E. S., Galarneau, E., Rutter, A., & Gustin, M. (2012). Gas-particle partitioning of atmospheric Hg (II) and its effect on global mercury deposition. *Atmos. Chem. Phys., 12*(1), 591-603.

Barth, M. C., Cantrell, C. A., Brune, W. H., Rutledge, S. A., Crawford, J. H., Huntrieser, H., Carey, L. D., MacGorman, D., Weisman, M., Pickering, K. E., Bruning, E., Anderson, B., Apel, E., Biggerstaff, M., Campos, T., Campuzano-Jost, P., Cohen, R., Crounse, J., Day, D. A., Diskin, G., Flocke, F., Fried, A., Garland, C., Heikes, B., Honomichl, S., Hornbrook, R., Huey, L. G., Jimenez, J. L., Lang, T., Lichtenstern, M., Mikoviny, T., Nault, B., O’Sullivan, D., Pan, L. L., Peischl, J., Pollack, I., Richter, D., Riemer, D., Ryerson, T., Schlager, H., St. Clair, J., Walega, J., Weibring, P., Weinheimer, A., Wennberg, P., Wisthaler, A., Wooldridge, P. J., & Ziegler, C. (2015). The Deep Convective Clouds and Chemistry (DC3) Field Campaign. *B. Am. Meteorol. Soc., 96*(8), 1281-1309. doi:10.1175/bams-d-13-00290.1

Bates, K. H., Evans, M. J., Henderson, B. H., & Jacob, D. J. (2024). Impacts of updated reaction kinetics on the global GEOS-Chem simulation of atmospheric chemistry. *Geoscientific Model Development, 17*(4), 1511-1524.

Beirle, S., Boersma, K. F., Platt, U., Lawrence, M. G., & Wagner, T. (2011). Megacity Emissions and Lifetimes of Nitrogen Oxides Probed from Space. *Science, 333*(6050), 1737-1739. doi:10.1126/science.1207824

Bertram, T. H., Perring, A. E., Wooldridge, P. J., Crounse, J. D., Kwan, A. J., Wennberg, P. O., Scheuer, E., Dibb, J., Avery, M., Sachse, G., Vay, S. A., Crawford, J. H., McNaughton, C. S., Clarke, A., Pickering, K. E., Fuelberg, H., Huey, G., Blake, D. R., Singh, H. B., Hall, S. R., Shetter, R. E., Fried, A., Heikes, B. G., & Cohen, R. C. (2007). Direct Measurements of the Convective Recycling of the Upper Troposphere. *Science, 315*(5813), 816-820. doi:doi:10.1126/science.1134548

Bertram, T. H., Thornton, J. A., Riedel, T. P., Middlebrook, A. M., Bahreini, R., Bates, T. S., Quinn, P. K., & Coffman, D. J. (2009). Direct observations of N2O5 reactivity on ambient aerosol particles. *Geophysical Research Letters, 36*(19). doi:https://doi.org/10.1029/2009GL040248

Bey, I., Jacob, D. J., Yantosca, R. M., Logan, J. A., Field, B. D., Fiore, A. M., Li, Q., Liu, H. Y., Mickley, L. J., & Schultz, M. G. (2001). Global modeling of tropospheric chemistry with assimilated meteorology: Model description and evaluation. *Journal of Geophysical Research: Atmospheres, 106*(D19), 23073-23095.

Blake, N. J., Blake, D. R., Swanson, A. L., Atlas, E., Flocke, F., & Rowland, F. S. (2003). Latitudinal, vertical, and seasonal variations of C1-C4 alkyl nitrates in the troposphere over the Pacific Ocean during PEM-Tropics A and B: Oceanic and continental sources. *Journal of Geophysical Research-Atmospheres, 108*(D2). doi:https://doi.org/10.1029/2001JD001444

Blakeslee, R. J., Mach, D. M., Bateman, M. G., & Bailey, J. C. (2014). Seasonal variations in the lightning diurnal cycle and implications for the global electric circuit. *Atmos. Res., 135-136*, 228-243. doi:https://doi.org/10.1016/j.atmosres.2012.09.023

Bockarie, A. S., Marais, E. A., & MacKenzie, A. (2020). Air pollution and climate forcing of the charcoal industry in Africa. *Environmental Science & Technology, 54*(21), 13429-13438.

Boersma, K. F., Eskes, H. J., Dirksen, R. J., van der A, R. J., Veefkind, J. P., Stammes, P., Huijnen, V., Kleipool, Q. L., Sneep, M., Claas, J., Leitão, J., Richter, A., Zhou, Y., & Brunner, D. (2011). An improved tropospheric NO_2 column retrieval algorithm for the Ozone Monitoring Instrument. *Atmos. Meas. Tech., 4*(9), 1905-1928. doi:10.5194/amt-4-1905-2011

Bofa, A. (2024). Optimizing Spatio-Temporal Correlation Structures for Modeling Food Security in Africa: A Simulation-Based Investigation. *BMC Bioinformatics, 25*(1). doi:10.1186/s12859-024-05791-w

Bourgeois, I., Peischl, J., Neuman, J. A., Brown, S. S., Allen, H. M., Campuzano-Jost, P., Coggon, M. M., DiGangi, J. P., Diskin, G. S., Gilman, J. B., Gkatzelis, G. I., Guo, H., Halliday, H. A., Hanisco, T. F., Holmes, C. D., Huey, L. G., Jimenez, J. L., Lamplugh, A. D., Lee, Y. R., Lindaas, J., Moore, R. H., Nault, B. A., Nowak, J. B., Pagonis, D., Rickly, P. S., Robinson, M. A., Rollins, A. W., Selimovic, V., St. Clair, J. M., Tanner, D., Vasquez, K. T., Veres, P. R., Warneke, C., Wennberg, P. O., Washenfelder, R. A., Wiggins, E. B., Womack, C. C., Xu, L., Zarzana, K. J., & Ryerson, T. B. (2022). Comparison of airborne measurements of NO, NO_2, HONO, NO_y, and CO during FIREX-AQ. *Atmos. Meas. Tech., 15*(16), 4901-4930. doi:10.5194/amt-15-4901-2022

Bradshaw, J., Davis, D., Grodzinsky, G., Smyth, S., Newell, R., Sandholm, S., & Liu, S. (2000). Observed distributions of nitrogen oxides in the remote free troposphere from the Nasa Global Tropospheric Experiment Programs. *Rev. Geophys., 38*(1), 61-116. doi:10.1029/1999rg900015

Bradshaw, J., Sandholm, S., & Talbot, R. (1998). An update on reactive odd-nitrogen measurements made during recent NASA Global Tropospheric Experiment programs. *Journal of Geophysical Research-Atmospheres, 103*(D15), 19129-19148. doi:https://doi.org/10.1029/98JD00621

Brasseur, G. P., & Jacob, D. J. (2017). *Modeling of atmospheric chemistry*: Cambridge University Press.

Brasseur, G. P., Müller, J.-F., & Granier, C. (1996). Atmospheric impact of NO_x emissions by subsonic aircraft: A three dimensional model study. *Journal of Geophysical Research-Atmospheres, 101*(D1), 1423-1428. doi:10.1029/95jd02363

Brenninkmeijer, C. A. M., Crutzen, P., Boumard, F., Dauer, T., Dix, B., Ebinghaus, R., Filippi, D., Fischer, H., Franke, H., Frieβ, U., Heintzenberg, J., Helleis, F., Hermann, M., Kock, H. H., Koeppel, C., Lelieveld, J., Leuenberger, M., Martinsson, B. G., Miemczyk, S., Moret, H. P., Nguyen, H. N., Nyfeler, P., Oram, D., O'Sullivan, D., Penkett, S., Platt, U., Pupek, M., Ramonet, M., Randa, B., Reichelt, M., Rhee, T. S., Rohwer, J., Rosenfeld, K., Scharffe, D., Schlager, H., Schumann, U., Slemr, F., Sprung, D., Stock, P., Thaler, R., Valentino, F., van Velthoven, P., Waibel, A., Wandel, A., Waschitschek, K., Wiedensohler, A., Xueref-Remy, I., Zahn, A., Zech, U., & Ziereis, H. (2007). Civil Aircraft for the regular investigation of the atmosphere based on an instrumented container: The new CARIBIC system. *Atmos. Chem. Phys., 7*(18), 4953-4976. doi:10.5194/acp-7-4953-2007

Brown, S. S., & Stutz, J. (2012). Nighttime radical observations and chemistry. *Chem. Soc. Rev., 41*(19), 6405-6447. doi:10.1039/C2CS35181A

Browne, E. C., Perring, A. E., Wooldridge, P. J., Apel, E., Hall, S. R., Huey, L. G., Mao, J., Spencer, K. M., Clair, J. M. S., Weinheimer, A. J., Wisthaler, A., & Cohen, R. C. (2011). Global and regional effects of the photochemistry of $CH_3O_2NO_2$: evidence from ARCTAS. *Atmos. Chem. Phys., 11*(9), 4209-4219. doi:10.5194/acp-11-4209-2011

Burkholder, J. B., Sander, S. P., Abbatt, J., Barker, J. R., Cappa, C., Crounse, J. D., Dibble, T. S., Huie, R. E., Kolb, C. E., Kurylo, M. J., Orkin, V. L., Percival, C. J., Wilmouth, D. M., and Wine, P. H. (2020). *Chemical kinetics and photochemical data for use in atmospheric studies, evaluation No. 19*.

Butler, T., Lupaşcu, A., & Nalam, A. (2020). Attribution of Ground-Level Ozone to Anthropogenic and Natural Sources of Nitrogen Oxides and Reactive Carbon in a Global Chemical Transport Model. *Atmospheric Chemistry and Physics, 20*(17), 10707-10731. doi:10.5194/acp-20-10707-2020

Cifuentes, F., González, C., Trejos, E. M., López, L. D., Sandoval, F. J., Cuellar, O. A., Mangones, S. C., Rojas, N. Y., & Aristizábal, B. H. (2021). Comparison of Top-Down and Bottom-Up Road Transport Emissions Through High-Resolution Air Quality Modeling in a City of Complex Orography. *Atmosphere, 12*(11), 1372. doi:10.3390/atmos12111372

Cohen, Y., Hauglustaine, D., Sauvage, B., Rohs, S., Konjari, P., Bundke, U., Petzold, A., Thouret, V., Zahn, A., & Ziereis, H. (2023). Evaluation of modelled climatologies of O3, CO, water vapour and NOy in the upper troposphere–lower stratosphere using regular in situ observations by passenger aircraft. *Atmos. Chem. Phys., 23*(23), 14973-15009. doi:10.5194/acp-23-14973-2023

Crawford, J. H., Ahn, J.-Y., Al-Saadi, J., Chang, L., Emmons, L. K., Kim, J., Lee, G., Park, J.-H., Park, R. J., Woo, J. H., Song, C.-K., Hong, J.-H., Hong, Y.-D., Lefer, B. L., Lee, M., Lee, T., Kim, S., Min, K.-E., Yum, S. S., Shin, H. J., Kim, Y.-W., Choi, J.-S., Park, J.-S., Szykman, J. J., Long, R. W., Jordan, C. E., Simpson, I. J., Fried, A., Dibb, J. E., Cho, S., & Kim, Y. P. (2021). The Korea–United States Air Quality (KORUS-AQ) field study. *Elementa: Science of the Anthropocene, 9*(1). doi:10.1525/elementa.2020.00163

Crippa, M., Guizzardi, D., Butler, T., Keating, T., Wu, R., Kaminski, J., Kuenen, J., Kurokawa, J., Chatani, S., Morikawa, T., Pouliot, G., Racine, J., Moran, M. D., Klimont, Z., Manseau, P. M., Mashayekhi, R., Henderson, B. H., Smith, S. J., Suchyta, H., Muntean, M., Solazzo, E., Banja, M., Schaaf, E., Pagani, F., Woo, J.-H., Kim, J., Monforti-Ferrario, F., Pisoni, E., Zhang, J., Niemi, D., Sassi, M., Ansari, T., & Foley, K. (2023). The HTAP_v3 emission mosaic: merging regional and global monthly emissions (2000–2018) to support air quality modelling and policies. *Earth System Science Data, 15*(6), 2667-2694. doi:10.5194/essd-15-2667-2023

Crippa, M., Solazzo, E., Huang, G., Guizzardi, D., Koffi, E., Muntean, M., Schieberle, C., Friedrich, R., & Janssens-Maenhout, G. (2020). High resolution temporal profiles in the Emissions Database for Global Atmospheric Research. *Scientific Data, 7*(1), 121. doi:10.1038/s41597-020-0462-2

Crounse, J. D., McKinney, K. A., Kwan, A. J., & Wennberg, P. O. (2006). Measurement of Gas-Phase Hydroperoxides by Chemical Ionization Mass Spectrometry. *Anal. Chem., 78*(19), 6726-6732. doi:10.1021/ac0604235

Culter, F. (2009). *NASA DC-8 Flying Laboratory Aircraft*. Retrieved from https://ghrc.nsstc.nasa.gov/home/sites/default/files/cutler_dc8.pdf

Dahlmann, K., Grewe, V., Ponater, M., & Matthes, S. (2011). Quantifying the contributions of individual NO_x sources to the trend in ozone radiative forcing. *Atmos. Environ., 45*(17), 2860-2868. doi:10.1016/j.atmosenv.2011.02.071

Dameris, M. (2015). Stratosphere/Troposphere exchange and structure | Tropopause. In G. R. North, J. Pyle, & F. Zhang (Eds.), *Encyclopedia of Atmospheric Sciences (Second Edition)* (pp. 269-272). Oxford: Academic Press.

Daniels, W., Wang, J. L., Ravikumar, A. P., Harrison, M. T., Roman-White, S., George, F., & Hammerling, D. (2023). Toward Multiscale Measurement-Informed Methane Inventories: Reconciling Bottom-Up Site-Level Inventories With Top-Down Measurements Using Continuous Monitoring Systems. *Environmental Science & Technology, 57*(32), 11823-11833. doi:10.1021/acs.est.3c01121

Davidson, J., Fehsenfeld, F., & Howard, C. J. (1977). The heats of formation of NO3− and NO3− association complexes with HNO3 and HBr. *International Journal of Chemical Kinetics, 9*(1), 17-29.

de Foy, B., Wilkins, J. L., Lu, Z., Streets, D. G., & Duncan, B. N. (2014). Model evaluation of methods for estimating surface emissions and chemical lifetimes from satellite data. *Atmospheric Environment, 98*, 66-77. doi:https://doi.org/10.1016/j.atmosenv.2014.08.051

Ehhalt, D. H., Rohrer, F., & Wahner, A. (1992). Sources and distribution of NO_x in the upper troposphere at northern mid-latitudes. *Journal of Geophysical Research-Atmospheres, 97*(D4), 3725-3738. doi:https://doi.org/10.1029/91JD03081

Elguindi, N., Granier, C., Stavrakou, T., Darras, S., Bauwens, M., Cao, H., Chen, C., Hugo Denier van der, G., Dubovik, O., Fu, T. M., Henze, D. K., Jiang, Z., Keita, S., Kuenen, J., Kurokawa, J., Liousse, C., Miyazaki, K., Müller, J.-F., Qu, Z., Solmon, F., & Zheng, B. (2020). Intercomparison of Magnitudes and Trends in Anthropogenic Surface Emissions From Bottom-Up Inventories, Top-Down Estimates, and Emission Scenarios. *Earth's Future, 8*(8). doi:10.1029/2020ef001520

Fioletov, V. E., McLinden, C. A., Krotkov, N., & Li, C. (2015). Lifetimes and emissions of SO2 from point sources estimated from OMI. *Geophysical Research Letters, 42*(6), 1969-1976. doi:https://doi.org/10.1002/2015GL063148

Fisher, J. A., Atlas, E. L., Barletta, B., Meinardi, S., Blake, D. R., Thompson, C. R., Ryerson, T. B., Peischl, J., Tzompa-Sosa, Z. A., & Murray, L. T. (2018). Methyl, Ethyl, and Propyl Nitrates: Global Distribution and Impacts on Reactive Nitrogen in Remote Marine Environments. *Journal of Geophysical Research-Atmospheres, 123*(21). doi:10.1029/2018jd029046

Fisher, J. A., Jacob, D. J., Travis, K. R., Kim, P. S., Marais, E. A., Chan Miller, C., Yu, K., Zhu, L., Yantosca, R. M., Sulprizio, M. P., Mao, J., Wennberg, P. O., Crounse, J. D., Teng, A. P., Nguyen, T. B., St. Clair, J. M., Cohen, R. C., Romer, P., Nault, B. A., Wooldridge, P. J., Jimenez, J. L., Campuzano-Jost, P., Day, D. A., Hu, W., Shepson, P. B., Xiong, F., Blake, D. R., Goldstein, A. H., Misztal, P. K., Hanisco, T. F., Wolfe, G. M., Ryerson, T. B., Wisthaler, A., & Mikoviny, T. (2016). Organic nitrate chemistry and its implications for nitrogen budgets in an isoprene- and monoterpene-rich atmosphere: constraints from aircraft (SEAC4RS) and ground-based (SOAS) observations in the Southeast US. *Atmos. Chem. Phys., 16*(9), 5969-5991. doi:10.5194/acp-16-5969-2016

Flocke, F. M., Weinheimer, A. J., Swanson, A. L., Roberts, J. M., Schmitt, R., & Shertz, S. (2005). On the measurement of PANs by gas chromatography and electron capture detection. *Journal of Atmospheric Chemistry, 52*, 19-43.

Fowler, D., Coyle, M., Skiba, U., Sutton, M. A., Cape, J. N., Reis, S., Sheppard, L. J., Jenkins, A., Grizzetti, B., Galloway, J. N., Vitousek, P. M., Leach, A. M., Bouwman, A. F., Butterbach-Bahl, K., Dentener, F., Stevenson, D. S., Amann, M. C., & Voß, M. (2013). The Global Nitrogen Cycle in the Twenty-First Century. *Philosophical Transactions of the Royal Society B Biological Sciences, 368*(1621), 20130164. doi:10.1098/rstb.2013.0164

Fuelberg, H. E., Hannan, J. R., van Velthoven, P. F. J., Browell, E. V., Bieberbach Jr., G., Knabb, R. D., Gregory, G. L., Pickering, K. E., & Selkirk, H. B. (2000). A meteorological overview of the Subsonic Assessment Ozone and Nitrogen Oxide Experiment (SONEX) period. *Journal of Geophysical Research-Atmospheres, 105*(D3), 3633-3651. doi:https://doi.org/10.1029/1999JD900917

Fuglestvedt, J. S., Berntsen, T. K., Isaksen, I. S., Mao, H., Liang, X. Z., & Wang, W. C. (1999). Climatic forcing of nitrogen oxides through changes in tropospheric ozone and methane; global 3D model studies. *Atmospheric Environment, 33*(6), 961-977. doi:https://doi.org/10.1016/S1352-2310(98)00217-9

Fung, P. L., Al-Jaghbeer, O., Pirjola, L., Aaltonen, H., & Järvi, L. (2023). Exploring the discrepancy between top-down and bottom-up approaches of fine spatio-temporal vehicular CO2 emission in an urban road network. *Science of The Total Environment, 901*, 165827. doi:https://doi.org/10.1016/j.scitotenv.2023.165827

Garland, R. M., Naidoo, M., Sibiya, B., & Oosthuizen, R. (2017). Air quality indicators from the Environmental Performance Index: potential use and limitations in South Africa. *Clean Air Journal, 27*(1), 33-33.

Geddes, J. A., & Martin, R. V. (2017). Global Deposition of Total Reactive Nitrogen Oxides From 1996 to 2014 Constrained With Satellite Observations of NO&lt;sub&gt;2&lt;/sub&gt; Columns. *Atmospheric Chemistry and Physics, 17*(16), 10071-10091. doi:10.5194/acp-17-10071-2017

Giglio, L., Randerson, J. T., & van der Werf, G. R. (2013). Analysis of daily, monthly, and annual burned area using the fourth-generation global fire emissions database (GFED4). *J. Geophys. Res.-Biogeo., 118*(1), 317-328. doi:https://doi.org/10.1002/jgrg.20042

Goldberg, D. L., Anenberg, S. C., Kerr, G. H., Lu, Z., & Streets, D. G. (2021a). TROPOMI: A Revolutionary New Satellite Instrument Measuring NO2 Air Pollution. *EM Magazine-A&WMA*.

Goldberg, D. L., Anenberg, S. C., Lu, Z., Streets, D. G., Lamsal, L. N., E McDuffie, E., & Smith, S. J. (2021b). Urban NOx emissions around the world declined faster than anticipated between 2005 and 2019. *Environmental Research Letters, 16*(11), 115004. doi:10.1088/1748-9326/ac2c34

Goldberg, D. L., Lu, Z., Oda, T., Lamsal, L. N., Liu, F., Griffin, D., McLinden, C. A., Krotkov, N. A., Duncan, B. N., & Streets, D. G. (2019a). Exploiting OMI NO2 satellite observations to infer fossil-fuel CO2 emissions from U.S. megacities. *Science of The Total Environment, 695*, 133805. doi:https://doi.org/10.1016/j.scitotenv.2019.133805

Goldberg, D. L., Lu, Z., Streets, D. G., de Foy, B., Griffin, D., McLinden, C. A., Lamsal, L. N., Krotkov, N. A., & Eskes, H. (2019b). Enhanced Capabilities of TROPOMI NO2: Estimating NOX from North American Cities and Power Plants. *Environmental Science & Technology, 53*(21), 12594-12601. doi:10.1021/acs.est.9b04488

Gressent, A., Sauvage, B., Cariolle, D., Evans, M., Leriche, M., Mari, C., & Thouret, V. (2016). Modeling lightning-NO_x chemistry on a sub-grid scale in a global chemical transport model. *Atmos. Chem. Phys., 16*(9), 5867-5889. doi:10.5194/acp-16-5867-2016

Gressent, A., Sauvage, B., Defer, E., Pätz, H. W., Thomas, K., Holle, R., Cammas, J.-P., Nédélec, P., Boulanger, D., Thouret, V., & Volz-Thomas, A. (2014). Lightning NO_x influence on large-scale NO_y and O_3 plumes observed over the northern mid-latitudes. *Tellus B, 66*(1). doi:10.3402/tellusb.v66.25544

Griffin, D., Zhao, X., McLinden, C. A., Boersma, K. F., Bourassa, A., Dammers, E., Degenstein, D. A., Eskes, H., Fehr, L., Fioletov, V., Hayden, K., Kharol, S. K., Li, S. M., Makar, P. A., Martin, R. V., Mihele, C., Mittermeier, R. L., Krotkov, N. A., Sneep, M., Lamsal, L. N., Linden, M. t., Geffen, J. v., Veefkind, P., & Wolde, M. (2019). High-Resolution Mapping of Nitrogen Dioxide With TROPOMI: First Results and Validation Over the Canadian Oil Sands. *Geophysical Research Letters, 46*(2), 1049-1060. doi:10.1029/2018gl081095

Guenther, A. B., Jiang, X., Heald, C. L., Sakulyanontvittaya, T., Duhl, T., Emmons, L. K., & Wang, X. (2012). The Model of Emissions of Gases and Aerosols from Nature version 2.1 (MEGAN2.1): an extended and updated framework for modeling biogenic emissions. *Geosci. Model Dev., 5*(6), 1471-1492. doi:10.5194/gmd-5-1471-2012

Hakkarainen, J., Kuhlmann, G., Koene, E., Santaren, D., Meier, S., Krol, M. C., van Stratum, B. J. H., Ialongo, I., Chevallier, F., Tamminen, J., Brunner, D., & Broquet, G. (2024). Analyzing nitrogen dioxide to nitrogen oxide scaling factors for data-driven satellite-based emission estimation methods: A case study of Matimba/Medupi power stations in South Africa. *Atmospheric Pollution Research, 15*(7), 102171. doi:https://doi.org/10.1016/j.apr.2024.102171

Harwood, M. H., Roberts, J. M., Frost, G. J., Ravishankara, A. R., & Burkholder, J. B. (2003). Photochemical Studies of $CH_3C(O)OONO_2$ (PAN) and $CH_3CH_2C(O)OONO_2$ (PPN): NO_3 Quantum Yields. *J. Phys. Chem. A, 107*(8), 1148-1154. doi:10.1021/jp0264230

Hoesly, R. M., Smith, S. J., Feng, L., Klimont, Z., Janssens-Maenhout, G., Pitkanen, T., Seibert, J. J., Vu, L., Andres, R. J., Bolt, R. M., Bond, T. C., Dawidowski, L., Kholod, N., Kurokawa, J. I., Li, M., Liu, L., Lu, Z., Moura, M. C. P., O'Rourke, P. R., & Zhang, Q. (2018). Historical (1750–2014) anthropogenic emissions of reactive gases and aerosols from the Community Emissions Data System (CEDS). *Geosci. Model Dev., 11*(1), 369-408. doi:10.5194/gmd-11-369-2018

Hofzumahaus, A., Kraus, A., Kylling, A., & Zerefos, C. S. (2002). Solar actinic radiation (280–420 nm) in the cloud-free troposphere between ground and 12 km altitude: Measurements and model results. *Journal of Geophysical Research: Atmospheres, 107*(D18), PAU 6-1-PAU 6-11. doi:https://doi.org/10.1029/2001JD900142

Hong, H., Lee, H., Kim, J., Jeong, U., Ryu, J.-Y., & Lee, D. H. (2017). Investigation of Simultaneous Effects of Aerosol Properties and Aerosol Peak Height on the Air Mass Factors for Space-Borne NO2 Retrievals. *Remote Sensing, 9*(3), 208. doi:10.3390/rs9030208

Horner, R. P., Marais, E. A., Wei, N., Ryan, R. G., & Shah, V. (2024). Vertical profiles of global tropospheric nitrogen dioxide (NO2) obtained by cloud slicing the TROPOspheric Monitoring Instrument (TROPOMI). *Atmos. Chem. Phys., 24*(22), 13047-13064. doi:10.5194/acp-24-13047-2024

Houghton, J. T. (2002). *The physics of atmospheres*: Cambridge University Press.

Hudman, R. C., Jacob, D. J., Turquety, S., Leibensperger, E. M., Murray, L. T., Wu, S., Gilliland, A. B., Avery, M., Bertram, T. H., Brune, W., Cohen, R. C., Dibb, J. E., Flocke, F. M., Fried, A., Holloway, J., Neuman, J. A., Orville, R., Perring, A., Ren, X., Sachse, G. W., Singh, H. B., Swanson, A., & Wooldridge, P. J. (2007). Surface and lightning sources of nitrogen oxides over the United States: Magnitudes, chemical evolution, and outflow. *J. Geophys. Res., 112*(D12). doi:10.1029/2006jd007912

Hudman, R. C., Moore, N. E., Mebust, A. K., Martin, R. V., Russell, A. R., Valin, L. C., & Cohen, R. C. (2012). Steps towards a mechanistic model of global soil nitric oxide emissions: implementation and space based-constraints. *Atmos. Chem. Phys., 12*(16), 7779-7795. doi:10.5194/acp-12-7779-2012

Huey, L. G. (2007). Measurement of trace atmospheric species by chemical ionization mass spectrometry: Speciation of reactive nitrogen and future directions. *Mass Spectrometry Reviews, 26*(2), 166-184. doi:https://doi.org/10.1002/mas.20118

Huey, L. G., Hanson, D. R., & Howard, C. J. (1995). Reactions of SF6-and I- with atmospheric trace gases. *The Journal of Physical Chemistry, 99*(14), 5001-5008.

Huntrieser, H., Lichtenstern, M., Scheibe, M., Aufmhoff, H., Schlager, H., Pucik, T., Minikin, A., Weinzierl, B., Heimerl, K., Pollack, I. B., Peischl, J., Ryerson, T. B., Weinheimer, A. J., Honomichl, S., Ridley, B. A., Biggerstaff, M. I., Betten, D. P., Hair, J. W., Butler, C. F., Schwartz, M. J., & Barth, M. C. (2016). Injection of lightning-produced NO_x, water vapor, wildfire emissions, and stratospheric air to the UT/LS as observed from DC3 measurements. *Journal of Geophysical Research-Atmospheres, 121*(11), 6638-6668. doi:https://doi.org/10.1002/2015JD024273

IPCC (2023). *Climate Change 2023: Synthesis Report. Contribution of Working Groups I, II and III to the Sixth Assessment Report of the Intergovernmental Panel on Climate Change [Core Writing Team, H. Lee and J. Romero (eds.)]. IPCC, Geneva, Switzerland*. doi:10.59327/ipcc/ar6-9789291691647

Isaxon, C., Abera, A., Asfaw, A., Bililign, S., Eriksson, A., Malmqvist, E., & Roba, K. T. (2022). A Call for Action: Air Pollution, a Serious Health and Economic Hazard Suffocating Africa. *Clean Air Journal, 32*(2). doi:10.17159/caj/2022/32/2.15116

Itahashi, S., Yumimoto, K., Kurokawa, J., Morino, Y., Nagashima, T., Miyazaki, K., Mäki, T., & Ohara, T. (2019). Inverse Estimation of NO_x Emissions Over China and India 2005–2016: Contrasting Recent Trends and Future Perspectives. *Environmental Research Letters, 14*(12), 124020. doi:10.1088/1748-9326/ab4d7f

Jacob, D. J., Crawford, J. H., Maring, H., Clarke, A. D., Dibb, J. E., Emmons, L. K., Ferrare, R. A., Hostetler, C. A., Russell, P. B., Singh, H. B., Thompson, A. M., Shaw, G. E., McCauley, E., Pederson, J. R., & Fisher, J. A. (2010). The Arctic Research of the Composition of the Troposphere from Aircraft and Satellites (ARCTAS) mission: design, execution, and first results. *Atmos. Chem. Phys., 10*(11), 5191-5212. doi:10.5194/acp-10-5191-2010

Jacob, D. J., Heikes, E. G., Fan, S. M., Logan, J. A., Mauzerall, D. L., Bradshaw, J. D., Singh, H. B., Gregory, G. L., Talbot, R. W., Blake, D. R., & Sachse, G. W. (1996). Origin of ozone and NO_x in the tropical troposphere: A photochemical analysis of aircraft observations over the South Atlantic basin. *Journal of Geophysical Research: Atmospheres, 101*(D19), 24235-24250. doi:10.1029/96jd00336

Jaeglé, L., Jacob, D. J., Wang, Y., Weinheimer, A. J., Ridley, B. A., Campos, T. L., Sachse, G. W., & Hagen, D. E. (1998). Sources and chemistry of NO_x in the upper troposphere over the United States. *Geophys. Res. Lett., 25*(10), 1705-1708. doi:10.1029/97gl03591

Jordan, N., Garner, N. M., Matchett, L. C., Tokarek, T. W., Osthoff, H. D., Odame-Ankrah, C. A., Grimm, C., Pickrell, K. N., Swainson, C., & Rosentreter, B. W. (2020). Potential Interferences in Photolytic Nitrogen Dioxide Converters for Ambient Air Monitoring: Evaluation of a Prototype. *Journal of the Air & Waste Management Association, 70*(8), 753-764. doi:10.1080/10962247.2020.1769770

Kaiser, J., Flemming, J., Schultz, M., Suttie, M., & Wooster, M. (2009). *The MACC global fire assimilation system: First emission products (GFASv0)*.

Kaiser, J. W., Heil, A., Andreae, M. O., Benedetti, A., Chubarova, N., Jones, L., Morcrette, J. J., Razinger, M., Schultz, M. G., Suttie, M., & van der Werf, G. R. (2012). Biomass burning emissions estimated with a global fire assimilation system based on observed fire radiative power. *Biogeosciences, 9*(1), 527-554. doi:10.5194/bg-9-527-2012

Kanakidou, M., Myriokefalitakis, S., Daskalakis, N., Fanourgakis, G. S., Nenes, A., Baker, A. R., Tsigaridis, K., & Mihalopoulos, N. (2016). Past, Present, and Future Atmospheric Nitrogen Deposition. *Journal of the Atmospheric Sciences, 73*(5), 2039-2047. doi:10.1175/jas-d-15-0278.1

Keita, S., Liousse, C., Assamoi, E.-M., Doumbia, T., N'Datchoh, E. T., Gnamien, S., Elguindi, N., Granier, C., & Yoboue, V. (2021). African Anthropogenic Emissions Inventory for Gases and Particles From 1990 to 2015. *Earth System Science Data, 13*(7), 3691-3705. doi:10.5194/essd-13-3691-2021

Keller, C. A., Long, M. S., Yantosca, R. M., Da Silva, A., Pawson, S., & Jacob, D. J. (2014). HEMCO v1. 0: a versatile, ESMF-compliant component for calculating emissions in atmospheric models. *Geoscientific Model Development, 7*(4), 1409-1417.

Kim, S., Huey, L. G., Stickel, R. E., Tanner, D. J., Crawford, J. H., Olson, J. R., Chen, G., Brune, W. H., Ren, X., Lesher, R., Wooldridge, P. J., Bertram, T. H., Perring, A., Cohen, R. C., Lefer, B. L., Shetter, R. E., Avery, M., Diskin, G., & Sokolik, I. (2007). Measurement of HO2NO2 in the free troposphere during the Intercontinental Chemical Transport Experiment–North America 2004. *Journal of Geophysical Research: Atmospheres, 112*(D12). doi:https://doi.org/10.1029/2006JD007676

Konovalov, I. B., Beekmann, M., Richter, A., & Burrows, J. P. (2006). Inverse modelling of the spatial distribution of NOx emissions on a continental scale using satellite data. *Atmos. Chem. Phys., 6*(7), 1747-1770. doi:10.5194/acp-6-1747-2006

Lacis, A. A., Wuebbles, D. J., & Logan, J. A. (1990). RADIATIVE FORCING OF CLIMATE BY CHANGES IN THE VERTICAL-DISTRIBUTION OF OZONE. *Journal of Geophysical Research-Atmospheres, 95*(D7), 9971-9981. doi:10.1029/JD095iD07p09971

Lamsal, L. N., Krotkov, N. A., Celarier, E. A., Swartz, W. H., Pickering, K. E., Bucsela, E. J., Gleason, J. F., Martin, R. V., Philip, S., Irie, H., Cede, A., Herman, J., Weinheimer, A., Szykman, J. J., & Knepp, T. N. (2014). Evaluation of OMI operational standard NO_2 column retrievals using in situ and surface-based NO_2 observations. *Atmospheric Chemistry and Physics, 14*(21), 11587-11609. doi:10.5194/acp-14-11587-2014

Lamsal, L. N., Krotkov, N. A., Vasilkov, A. P., Марченко, С. В., Qin, W., Yang, E. S., Fasnacht, Z., Joiner, J., Choi, S., Haffner, D. P., Swartz, W. H., Fisher, B. L., & Bucsela, E. J. (2021). Ozone Monitoring Instrument (OMI) Aura Nitrogen Dioxide Standard Product Version 4.0 With Improved Surface and Cloud Treatments. *Atmospheric Measurement Techniques, 14*(1), 455-479. doi:10.5194/amt-14-455-2021

Lamsal, L. N., Martin, R. V., Parrish, D. D., & Krotkov, N. A. (2013). Scaling Relationship for NO2 Pollution and Urban Population Size: A Satellite Perspective. *Environmental Science & Technology, 47*(14), 7855-7861. doi:10.1021/es400744g

Lange, K., Richter, A., & Burrows, J. P. (2022). Variability of nitrogen oxide emission fluxes and lifetimes estimated from Sentinel-5P TROPOMI observations. *Atmos. Chem. Phys., 22*(4), 2745-2767. doi:10.5194/acp-22-2745-2022

Laughner, J. L., & Cohen, R. C. (2019). Direct observation of changing NOx lifetime in North American cities. *Science, 366*(6466), 723-727. doi:doi:10.1126/science.aax6832

Le Breton, M., Bacak, A., Muller, J. B. A., O'Shea, S. J., Xiao, P., Ashfold, M. N. R., Cooke, M. C., Batt, R., Shallcross, D. E., Oram, D. E., Forster, G., Bauguitte, S. J. B., Palmer, P. I., Parrington, M., Lewis, A. C., Lee, J. D., & Percival, C. J. (2013). Airborne hydrogen cyanide measurements using a chemical ionisation mass spectrometer for the plume identification of biomass burning forest fires. *Atmos. Chem. Phys., 13*(18), 9217-9232. doi:10.5194/acp-13-9217-2013

Lee, Y. R., Huey, L. G., Tanner, D. J., Takeuchi, M., Qu, H., Liu, X., Ng, N. L., Crawford, J. H., Fried, A., Richter, D., Simpson, I. J., Blake, D. R., Blake, N. J., Meinardi, S., Kim, S., Diskin, G. S., Digangi, J. P., Choi, Y., Pusede, S. E., Wennberg, P. O., Kim, M. J., Crounse, J. D., Teng, A. P., Cohen, R. C., Romer, P. S., Brune, W., Wisthaler, A., Mikoviny, T., Jimenez, J. L., Campuzano-Jost, P., Nault, B. A., Weinheimer, A., Hall, S. R., & Ullmann, K. (2022). An investigation of petrochemical emissions during KORUS-AQ: Ozone production, reactive nitrogen evolution, and aerosol production. *Elementa: Science of the Anthropocene, 10*(1). doi:10.1525/elementa.2022.00079

Leue, C., Wenig, M., Wagner, T., Klimm, O., Platt, U., & Jähne, B. (2001). Quantitative analysis of NO emissions from Global Ozone Monitoring Experiment satellite image sequences. *Journal of Geophysical Research: Atmospheres, 106*(D6), 5493-5505. doi:https://doi.org/10.1029/2000JD900572

Levelt, P. F., Joiner, J., Tamminen, J., Veefkind, J. P., Bhartia, P. K., Stein Zweers, D. C., Duncan, B. N., Streets, D. G., Eskes, H., & van der A, R. (2018). The Ozone Monitoring Instrument: overview of 14 years in space. *Atmospheric Chemistry and Physics, 18*(8), 5699-5745.

Levelt, P. F., Van Den Oord, G. H., Dobber, M. R., Malkki, A., Visser, H., De Vries, J., Stammes, P., Lundell, J. O., & Saari, H. (2006). The ozone monitoring instrument. *IEEE Transactions on geoscience and remote sensing, 44*(5), 1093-1101.

Levy II, H., Mahlman, J. D., & Moxim, W. J. (1980). A stratospheric source of reactive nitrogen in the unpolluted troposphere. *Geophys. Res. Lett., 7*(6), 441-444. doi:https://doi.org/10.1029/GL007i006p00441

Levy II, H., Moxim, W. J., Klonecki, A. A., & Kasibhatla, P. S. (1999). Simulated tropospheric NO_x : Its evaluation, global distribution and individual source contributions. *J. Geophys Res.-Atmos., 104*(D21), 26279-26306. doi:https://doi.org/10.1029/1999JD900442

Li, M., Klimont, Z., Zhang, Q., Martin, R. V., Zheng, B., Heyes, C., Cofala, J., Zhang, Y., & He, K. (2018). Comparison and evaluation of anthropogenic emissions of SO2 and NOx over China. *Atmos. Chem. Phys., 18*(5), 3433-3456. doi:10.5194/acp-18-3433-2018

Li, Q., Jacob, D. J., Yantosca, R. M., Heald, C. L., Singh, H. B., Koike, M., Zhao, Y., Sachse, G. W., & Streets, D. G. (2003). A global three-dimensional model analysis of the atmospheric budgets of HCN and CH_3CN: Constraints from aircraft and ground measurements. *Journal of Geophysical Research-Atmospheres, 108*(D21). doi:https://doi.org/10.1029/2002JD003075

Liang, Q., Rodriguez, J. M., Douglass, A. R., Crawford, J. H., Olson, J. R., Apel, E., Bian, H., Blake, D. R., Brune, W., Chin, M., Colarco, P. R., da Silva, A., Diskin, G. S., Duncan, B. N., Huey, L. G., Knapp, D. J., Montzka, D. D., Nielsen, J. E., Pawson, S., Riemer, D. D., Weinheimer, A. J., & Wisthaler, A. (2011). Reactive nitrogen, ozone and ozone production in the Arctic troposphere and the impact of stratosphere-troposphere exchange. *Atmos. Chem. Phys., 11*(24), 13181-13199. doi:10.5194/acp-11-13181-2011

Lin, H., Long, M. S., Sander, R., Sandu, A., Yantosca, R. M., Estrada, L. A., Shen, L., & Jacob, D. J. (2023). An Adaptive Auto-Reduction Solver for Speeding Up Integration of Chemical Kinetics in Atmospheric Chemistry Models: Implementation and Evaluation in the Kinetic Pre-Processor (KPP) Version 3.0. 0. *Journal of Advances in Modeling Earth Systems, 15*(2), e2022MS003293.

Lin, J.-T., & McElroy, M. B. (2010). Impacts of boundary layer mixing on pollutant vertical profiles in the lower troposphere: Implications to satellite remote sensing. *Atmospheric Environment, 44*(14), 1726-1739.

Lin, S.-J., & Rood, R. B. (1996). Multidimensional flux-form semi-Lagrangian transport schemes. *Monthly Weather Review, 124*(9), 2046-2070.

Liousse, C., Assamoi, E., Criqui, P., Granier, C., & Rosset, R. (2014). Explosive Growth in African Combustion Emissions From 2005 to 2030. *Environmental Research Letters, 9*(3), 035003. doi:10.1088/1748-9326/9/3/035003

Liu, F., Tao, Z., Beirle, S., Joiner, J., Yoshida, Y., Smith, S. J., Knowland, K. E., & Wagner, T. (2022). A new method for inferring city emissions and lifetimes of nitrogen oxides from high-resolution nitrogen dioxide observations: a model study. *Atmos. Chem. Phys., 22*(2), 1333-1349. doi:10.5194/acp-22-1333-2022

Liu, H., Jacob, D. J., Bey, I., & Yantosca, R. M. (2001). Constraints from 210Pb and 7Be on wet deposition and transport in a global three-dimensional chemical tracer model driven by assimilated meteorological fields. *Journal of Geophysical Research: Atmospheres, 106*(D11), 12109-12128.

Liu, S., Valks, P., Pinardi, G., Xu, J., Chan, K. L., Argyrouli, A., Lutz, R., Beirle, S., Khorsandi, E., Baier, F., Huijnen, V., Bais, A., Donner, S., Dörner, S., Gratsea, M., Hendrick, F., Karagkiozidis, D., Lange, K., Piters, A. J. M., Remmers, J., Richter, A., Van Roozendael, M., Wagner, T., Wenig, M., & Loyola, D. G. (2021). An improved TROPOMI tropospheric NO2 research product over Europe. *Atmos. Meas. Tech., 14*(11), 7297-7327. doi:10.5194/amt-14-7297-2021

Logan, J. A. (1983). Nitrogen oxides in the troposphere: Global and regional budgets. *Journal of Geophysical Research-Oceans, 88*(C15), 10785-10807. doi:https://doi.org/10.1029/JC088iC15p10785

Lorente, A., Boersma, K. F., Eskes, H. J., Veefkind, J. P., van Geffen, J. H. G. M., de Zeeuw, M. B., Denier van der Gon, H. A. C., Beirle, S., & Krol, M. C. (2019). Quantification of nitrogen oxides emissions from build-up of pollution over Paris with TROPOMI. *Scientific Reports, 9*(1), 20033. doi:10.1038/s41598-019-56428-5

Lourens, A. S., Beukes, J. P., Van Zyl, P. G., Pienaar, J. J., Butler, T. M., Beirle, S., Wagner, T. K., Heue, K.-P., & Lawrence, M. G. (2012). Re-evaluating the NO_2 hotspot over the South African Highveld. *South African Journal of Science, 108*(11), 1-6.

Lourens, A. S. M., Butler, T., Beukes, J. P., Zyl, P. G. v., Fourie, G., & Lawrence, M. G. (2016). Investigating Atmospheric Photochemistry in the Johannesburg-Pretoria Megacity Using a Box Model. *South African Journal of Science, 112*(1/2), 11. doi:10.17159/sajs.2016/2015-0169

Lu, G., Marais, E. A., Vohra, K., Horner, R. P., Zhang, D., Martin, R. V., & Guttikunda, S. (2025). Near-automated estimate of city nitrogen oxides emissions applied to South and Southeast Asia. *Journal of Geophysical Research: Atmospheres, 130*(2), e2024JD041000.

Lu, X., Zhang, L., Wu, T., Long, M. S., Wang, J., Jacob, D. J., Zhang, F., Zhang, J., Eastham, S. D., Hu, L., Zhu, L., Liu, X., & Wei, M. (2020). Development of the global atmospheric chemistry general circulation model BCC-GEOS-Chem v1.0: model description and evaluation. *Geosci. Model Dev., 13*(9), 3817-3838. doi:10.5194/gmd-13-3817-2020

Lu, Z., Streets, D. G., de Foy, B., Lamsal, L. N., Duncan, B. N., & Xing, J. (2015). Emissions of nitrogen oxides from US urban areas: estimation from Ozone Monitoring Instrument retrievals for 2005–2014. *Atmos. Chem. Phys., 15*(18), 10367-10383. doi:10.5194/acp-15-10367-2015

Luo, G., Yu, F., & Moch, J. M. (2020). Further improvement of wet process treatments in GEOS-Chem v12.6.0: impact on global distributions of aerosols and aerosol precursors. *Geosci. Model Dev., 13*(6), 2879-2903. doi:10.5194/gmd-13-2879-2020

Marais, E. A., Jacob, D. J., Choi, S., Joiner, J., Belmonte-Rivas, M., Cohen, R. C., Beirle, S., Murray, L. T., Schiferl, L. D., Shah, V., & Jaeglé, L. (2018). Nitrogen oxides in the global upper troposphere: interpreting cloud-sliced NO_2 observations from the OMI satellite instrument. *Atmos. Chem. Phys., 18*(23), 17017-17027. doi:10.5194/acp-18-17017-2018

Marais, E. A., Roberts, J. F., Ryan, R. G., Eskes, H., Boersma, K. F., Choi, S., Joiner, J., Abuhassan, N., Redondas, A., Grutter, M., Cede, A., Gomez, L., & Navarro-Comas, M. (2021). New observations of NO_2 in the upper troposphere from TROPOMI. *Atmos. Meas. Tech., 14*(3), 2389-2408. doi:10.5194/amt-14-2389-2021

Marais, E. A., & Wiedinmyer, C. (2016). Air Quality Impact of Diffuse and Inefficient Combustion Emissions in Africa (DICE-Africa). *Environmental Science & Technology, 50*(19), 10739-10745. doi:10.1021/acs.est.6b02602

Marenco, A., Thouret, V., Nédélec, P., Smit, H., Helten, M., Kley, D., Karcher, F., Simon, P., Law, K., Pyle, J., Poschmann, G., Von Wrede, R., Hume, C., & Cook, T. (1998). Measurement of ozone and water vapor by Airbus in-service aircraft: The MOZAIC airborne program, an overview. *Journal of Geophysical Research-Atmospheres, 103*(D19), 25631-25642. doi:10.1029/98jd00977

Martin, M. V., Honrath, R. E., Owen, R. C., & Li, Q. B. (2008). Seasonal Variation of Nitrogen Oxides in the Central North Atlantic Lower Free Troposphere. *Journal of Geophysical Research Atmospheres, 113*(D17). doi:10.1029/2007jd009688

Martin, R. V., Jacob, D. J., Chance, K., Kurosu, T. P., Palmer, P. I., & Evans, M. J. (2003). Global inventory of nitrogen oxide emissions constrained by space-based observations of NO2 columns. *Journal of Geophysical Research: Atmospheres, 108*(D17). doi:https://doi.org/10.1029/2003JD003453

Martin, R. V., Parrish, D. D., Ryerson, T. B., Nicks, D. K., Chance, K., Kurosu, T. P., Jacob, D. J., Sturges, E. D., Fried, A., & Wert, B. P. (2004). Evaluation of GOME satellite measurements of tropospheric NO_2 and HCHO using regional data from aircraft campaigns in the southeastern United States. *Journal of Geophysical Research-Atmospheres, 109*(D24), 11. doi:10.1029/2004jd004869

Martínez-Alonso, S. (2023). S-5p/TROPOMI-Derived NO_x Emissions From Copper/Cobalt Mining and Other Industrial Activities in the Copperbelt (Democratic Republic of Congo and Zambia). *Geophysical Research Letters, 50*(19). doi:10.1029/2023gl104109

Matandirotya, N. R., & Burger, R. (2023). An assessment of NO2 atmospheric air pollution over three cities in South Africa during 2020 COVID-19 pandemic. *Air Quality, Atmosphere & Health, 16*(2), 263-276.

McDuffie, E. E., Smith, S. J., O'Rourke, P., Tibrewal, K., Venkataraman, C., Marais, E. A., Zheng, B., Crippa, M., Brauer, M., & Martin, R. V. (2020). A global anthropogenic emission inventory of atmospheric pollutants from sector- and fuel-specific sources (1970–2017): an application of the Community Emissions Data System (CEDS). *Earth Syst. Sci. Data, 12*(4), 3413-3442. doi:10.5194/essd-12-3413-2020

Mickley, L. J., Murti, P. P., Jacob, D. J., Logan, J. A., Koch, D. M., & Rind, D. (1999). Radiative forcing from tropospheric ozone calculated with a unified chemistry-climate model. *Journal of Geophysical Research-Atmospheres, 104*(D23), 30153-30172. doi:10.1029/1999jd900439

Miyazaki, Y., Kondo, Y., Koike, M., Fuelberg, H. E., Kiley, C. M., Kita, K., Takegawa, N., Sachse, G. W., Flocke, F., Weinheimer, A. J., Singh, H. B., Eisele, F. L., Zondlo, M. A., Talbot, R. W., Sandholm, S. T., Avery, M. A., & Blake, D. R. (2003). Synoptic-scale Transport of Reactive Nitrogen Over the Western Pacific in Spring. *Journal of Geophysical Research Atmospheres, 108*(D20). doi:10.1029/2002jd003248

Mukwevho, P. (2024). Identifying Critical Assumptions and Risks in Air Quality Management Planning Using Theory of Change Approach. *Clean Air Journal, 34*(1). doi:10.17159/caj/2024/34/1.16571

Murray, L. T., Fiore, A. M., Shindell, D. T., Naik, V., & Horowitz, L. W. (2021). Large uncertainties in global hydroxyl projections tied to fate of reactive nitrogen and carbon. *P. Natl. Acad. Sci. USA, 118*(43), e2115204118. doi:doi:10.1073/pnas.2115204118

Murray, L. T., Jacob, D. J., Logan, J. A., Hudman, R. C., & Koshak, W. J. (2012). Optimized regional and interannual variability of lightning in a global chemical transport model constrained by LIS/OTD satellite data. *Journal of Geophysical Research-Atmospheres, 117*(D20). doi:10.1029/2012jd017934

Murray, L. T., Logan, J. A., & Jacob, D. J. (2013). Interannual variability in tropical tropospheric ozone and OH: The role of lightning. *Journal of Geophysical Research-Atmospheres, 118*(19), 11,468-411,480. doi:10.1002/jgrd.50857

NASA. (2009). NASA: Airborne Science Data for Atmospheric Composition. Retrieved from https://www-air.larc.nasa.gov/cgi-bin/ArcView/arctas?DC8=1 (last access: 24 October 2024).

NASA. (2015). NASA: Airborne Science Data for Atmospheric Composition. Retrieved from https://www-air.larc.nasa.gov/cgi-bin/ArcView/seac4rs (last access: 24 October 2024).

NASA. (2017). NASA: EARTHDATA, Korea United States Air Quality Study. Retrieved from https://asdc.larc.nasa.gov/project/KORUS-AQ (last access: 24 October 2024).

NASA. (2021). NASA: EARTHDATA, ATom: Merged Atmospheric Chemistry, Trace Gases, and Aerosols, Version 2. Retrieved from https://daac.ornl.gov/cgi-bin/dsviewer.pl?ds_id=1925 (last access: 24 October 2024).

Nault, B. A., Garland, C., Pusede, S. E., Wooldridge, P. J., Ullmann, K., Hall, S. R., & Cohen, R. C. (2015). Measurements of $CH_3O_2NO_2$ in the upper troposphere. *Atmos. Meas. Tech., 8*(2), 987-997. doi:10.5194/amt-8-987-2015

Neuman, J., Gao, R., Schein, M., Ciciora, S., Holecek, J., Thompson, T., Winkler, R., McLaughlin, R., Northway, M., & Richard, E. (2000). A fast-response chemical ionization mass spectrometer for in situ measurements of HNO3 in the upper troposphere and lower stratosphere. *Review of Scientific Instruments, 71*(10), 3886-3894.

Neuman, J. A., Huey, L. G., Dissly, R. W., Fehsenfeld, F. C., Flocke, F., Holecek, J. C., Holloway, J. S., Hübler, G., Jakoubek, R., Nicks Jr., D. K., Parrish, D. D., Ryerson, T. B., Sueper, D. T., & Weinheimer, A. J. (2002). Fast-response airborne in situ measurements of HNO3 during the Texas 2000 Air Quality Study. *Journal of Geophysical Research: Atmospheres, 107*(D20), ACH 8-1-ACH 8-14. doi:https://doi.org/10.1029/2001JD001437

Neuman, J. A., Parrish, D. D., Trainer, M., Ryerson, T. B., Holloway, J. S., Nowak, J. B., Swanson, A. L., Flocke, F., Roberts, J. M., Brown, S. S., Stark, H., Sommariva, R., Stohl, A., Peltier, R. E., Weber, R. J., Wollny, A. G., Sueper, D., Hübler, G., & Fehsenfeld, F. C. (2006). Reactive Nitrogen Transport and Photochemistry in Urban Plumes Over the North Atlantic Ocean. *Journal of Geophysical Research Atmospheres, 111*(D23). doi:10.1029/2005jd007010

Palacios, M., Martín, F. L., & Cabal, H. (2001). Methodologies for Estimating Disaggregated Anthropogenic Emissions—Application to a Coastal Mediterranean Region of Spain. *Journal of the Air & Waste Management Association, 51*(5), 642-657. doi:10.1080/10473289.2001.10464305

Paulot, F., Jacob, D. J., & Henze, D. K. (2013). Sources and Processes Contributing to Nitrogen Deposition: An Adjoint Model Analysis Applied to

Biodiversity Hotspots Worldwide. *Environmental Science & Technology, 47*(7), 3226-3233. doi:10.1021/es3027727

Petzold, A., Thouret, V., Gerbig, C., Zahn, A., Brenninkmeijer, C. A. M., Gallagher, M., Hermann, M., Pontaud, M., Ziereis, H., Boulanger, D., Marshall, J., Nédélec, P., Smit, H. G. J., Friess, U., Flaud, J.-M., Wahner, A., Cammas, J.-P., & Volz-Thomas, A. (2015). Global-scale atmosphere monitoring by in-service aircraft – current achievements and future prospects of the European Research Infrastructure IAGOS. *Tellus B, 67*(1), 28452. doi:10.3402/tellusb.v67.28452

Pollack, I. B., Lerner, B. M., & Ryerson, T. B. (2010). Evaluation of ultraviolet light-emitting diodes for detection of atmospheric NO_2 by photolysis - chemiluminescence. *J. Atmos. Chem., 65*(2), 111-125. doi:10.1007/s10874-011-9184-3

Pope, R. J., Kelly, R., Marais, E. A., Graham, A. M., Wilson, C., Harrison, J. J., Moniz, S. J. A., Ghalaieny, M., Arnold, S. R., & Chipperfield, M. P. (2022). Exploiting satellite measurements to explore uncertainties in UK bottom-up NOx emission estimates. *Atmos. Chem. Phys., 22*(7), 4323-4338. doi:10.5194/acp-22-4323-2022

Prather, M. J., & Jacob, D. J. (1997). A persistent imbalance in HO_x and NO_x photochemistry of the upper troposphere driven by deep tropical convection. *Geophys. Res. Lett., 24*(24), 3189-3192. doi:https://doi.org/10.1029/97GL03027

Rafey, W., & Sovacool, B. K. (2011). Competing discourses of energy development: The implications of the Medupi coal-fired power plant in South Africa. *Global Environmental Change, 21*(3), 1141-1151.

Randerson, J., Chen, Y., Van Der Werf, G., Rogers, B., & Morton, D. (2012). Global burned area and biomass burning emissions from small fires. *Journal of Geophysical Research: Biogeosciences, 117*(G4).

Rap, A., Richards, N. A. D., Forster, P. M., Monks, S. A., Arnold, S. R., & Chipperfield, M. P. (2015). Satellite constraint on the tropospheric ozone radiative effect. *Geophys. Res. Lett., 42*(12), 5074-5081. doi:10.1002/2015gl064037

Reed, C., Brumby, C. A., Crilley, L. R., Kramer, L. J., Bloss, W. J., Seakins, P. W., Lee, J. D., & Carpenter, L. J. (2016a). HONO measurement by differential photolysis. *Atmos. Meas. Tech., 9*(6), 2483-2495. doi:10.5194/amt-9-2483-2016

Reed, C., Evans, M. J., Di Carlo, P., Lee, J. D., & Carpenter, L. J. (2016b). Interferences in photolytic NO_2 measurements: explanation for an apparent missing oxidant? *Atmos. Chem. Phys., 16*(7), 4707-4724. doi:10.5194/acp-16-4707-2016

Roberts, J. M. (1990). The atmospheric chemistry of organic nitrates. *Atmos. Environ. A-Gen., 24*(2), 243-287. doi:https://doi.org/10.1016/0960-1686(90)90108-Y

Roberts, J. M., Flocke, F., Stroud, C. A., Hereid, D., Williams, E., Fehsenfeld, F., Brune, W., Martinez, M., & Harder, H. (2002). Ground-based measurements of peroxycarboxylic nitric anhydrides (PANs) during the 1999 Southern Oxidants Study Nashville Intensive. *Journal of Geophysical Research-Atmospheres, 107*(D21), ACH 1-1-ACH 1-10. doi:https://doi.org/10.1029/2001JD000947

Roberts, J. M., Williams, J., Baumann, K., Buhr, M. P., Goldan, P. D., Holloway, J., Hübler, G., Kuster, W. C., McKeen, S. A., Ryerson, T. B., Trainer, M., Williams, E. J., Fehsenfeld, F. C., Bertman, S. B., Nouaime, G., Seaver, C., Grodzinsky, G., Rodgers, M., & Young, V. L. (1998). Measurements of PAN, PPN, and MPAN made during the 1994 and 1995 Nashville Intensives of the Southern Oxidant Study: Implications for regional ozone production from biogenic hydrocarbons. *Journal of Geophysical*

Research-Atmospheres, 103(D17), 22473-22490. doi:https://doi.org/10.1029/98JD01637

Ryerson, T. B., Williams, E. J., & Fehsenfeld, F. C. (2000). An efficient photolysis system for fast-response NO_2 measurements. *Journal of Geophysical Research-Atmospheres, 105*(D21), 26447-26461. doi:https://doi.org/10.1029/2000JD900389

Schneider, J., Mertes, S., van Pinxteren, D., Herrmann, H., & Borrmann, S. (2017). Uptake of nitric acid, ammonia, and organics in orographic clouds: mass spectrometric analyses of droplet residual and interstitial aerosol particles. *Atmos. Chem. Phys., 17*(2), 1571-1593. doi:10.5194/acp-17-1571-2017

Seinfeld, J. H., & Pandis, S. N. (2016). *Atmospheric chemistry and physics: from air pollution to climate change*: John Wiley & Sons.

Sekiya, T., Miyazaki, K., Eskes, H., Sudo, K., Takigawa, M., & Kanaya, Y. (2022). A comparison of the impact of TROPOMI and OMI tropospheric NO2 on global chemical data assimilation. *Atmos. Meas. Tech., 15*(6), 1703-1728. doi:10.5194/amt-15-1703-2022

Seltzer, K. M., Vizuete, W., & Henderson, B. H. (2015). Evaluation of updated nitric acid chemistry on ozone precursors and radiative effects. *Atmos. Chem. Phys., 15*(10), 5973-5986. doi:10.5194/acp-15-5973-2015

Shah, V., Jacob, D. J., Dang, R., Lamsal, L. N., Strode, S. A., Steenrod, S. D., Boersma, K. F., Eastham, S. D., Fritz, T. M., Thompson, C., Peischl, J., Bourgeois, I., Pollack, I. B., Nault, B. A., Cohen, R. C., Campuzano-Jost, P., Jimenez, J. L., Andersen, S. T., Carpenter, L. J., Sherwen, T., & Evans, M. J. (2023). Nitrogen oxides in the free troposphere: implications for tropospheric oxidants and the interpretation of satellite NO_2 measurements. *Atmos. Chem. Phys., 23*(2), 1227-1257. doi:10.5194/acp-23-1227-2023

Shah, V., Jacob, D. J., Li, K., Silvern, R. F., Zhai, S., Liu, M., Lin, J., & Zhang, Q. (2020). Effect of changing NOx lifetime on the seasonality and long-term trends of satellite-observed tropospheric NO2 columns over China. *Atmos. Chem. Phys., 20*(3), 1483-1495. doi:10.5194/acp-20-1483-2020

Silvern, R. F., Jacob, D. J., Travis, K. R., Sherwen, T., Evans, M. J., Cohen, R. C., Laughner, J. L., Hall, S. R., Ullmann, K., Crounse, J. D., Wennberg, P. O., Peischl, J., & Pollack, I. B. (2018). Observed NO/NO_2 Ratios in the Upper Troposphere Imply Errors in NO-NO_2-O_3 Cycling Kinetics or an Unaccounted NO_x Reservoir. *Geophys. Res. Lett., 45*(9), 4466-4474. doi:10.1029/2018gl077728

Singh, H. B. (1987). Reactive nitrogen in the troposphere. *Environ. Sci. Technol., 21*(4), 320-327. doi:10.1021/es00158a001

Singh, H. B., Brune, W. H., Crawford, J. H., Flocke, F., & Jacob, D. J. (2009). Chemistry and transport of pollution over the Gulf of Mexico and the Pacific: spring 2006 INTEX-B campaign overview and first results. *Atmos. Chem. Phys., 9*(7), 2301-2318. doi:10.5194/acp-9-2301-2009

Singh, H. B., Brune, W. H., Crawford, J. H., Jacob, D. J., & Russell, P. B. (2006). Overview of the summer 2004 Intercontinental Chemical Transport Experiment–North America (INTEX-A). *Journal of Geophysical Research-Atmospheres, 111*(D24). doi:https://doi.org/10.1029/2006JD007905

Singh, H. B., Salas, L. J., Herlth, D., Kolyer, R., Czech, E., Avery, M. A., Crawford, J. H., Pierce, R. B., Sachse, G. W., Blake, D. R., Cohen, R. C., Bertram, T. H., Perring, A. E., Wooldridge, P. J., Dibb, J. E., Huey, G., Hudman, R. C., Turquety, S., Emmons, L. K., Flocke, F., Tang, Y., Carmichael, G. R., & Horowitz, L. W. (2007). Reactive Nitrogen Distribution and Partitioning in the North American Troposphere and Lowermost Stratosphere. *Journal of Geophysical Research Atmospheres, 112*(D12). doi:10.1029/2006jd007664

Singh, H. B., Thompson, A. M., & Schlager, H. (1999). SONEX airborne mission and coordinated POLINAT-2 activity: Overview and accomplishments. *Geophys. Res. Lett., 26*(20), 3053-3056. doi:https://doi.org/10.1029/1999GL900588

Slusher, D. L., Huey, L. G., Tanner, D. J., Flocke, F. M., & Roberts, J. M. (2004). A thermal dissociation–chemical ionization mass spectrometry (TD-CIMS) technique for the simultaneous measurement of peroxyacyl nitrates and dinitrogen pentoxide. *Journal of Geophysical Research-Atmospheres, 109*(D19). doi:https://doi.org/10.1029/2004JD004670

Sörgel, M., Regelin, E., Bozem, H., Diesch, J. M., Drewnick, F., Fischer, H., Harder, H., Held, A., Hosaynali-Beygi, Z., Martinez, M., & Zetzsch, C. (2011). Quantification of the unknown HONO daytime source and its relation to NO_2. *Atmos. Chem. Phys., 11*(20), 10433-10447. doi:10.5194/acp-11-10433-2011

Spicer, C. W. (1982). Nitrogen oxide reactions in the urban plume of Boston. *Science, 215*(4536), 1095-1097.

Stettler, M. E. J., Eastham, S., & Barrett, S. R. H. (2011). Air quality and public health impacts of UK airports. Part I: Emissions. *Atmos. Environ., 45*(31), 5415-5424. doi:10.1016/j.atmosenv.2011.07.012

Storelvmo, T., Stenchikov, G., Soden, B., Shine, K. P., Naik, V., Myhre, G., Mahowald, N., Lean, J., Haywood, J., Collins, W., & Ramaswamy, V. (2019). Radiative Forcing of Climate: The Historical Evolution of the Radiative Forcing Concept, the Forcing Agents and their Quantification, and Applications. *Meteorological Monographs, 59*, 14.11-14.101. doi:10.1175/amsmonographs-d-19-0001.1

Stratmann, G., Ziereis, H., Stock, P., Brenninkmeijer, C. A. M., Zahn, A., Rauthe-Schöch, A., Velthoven, P. V., Schlager, H., & Volz-Thomas, A. (2016). NO and NO_y in the upper troposphere: Nine years of CARIBIC measurements onboard a passenger aircraft. *Atmos. Environ., 133*, 93-111. doi:https://doi.org/10.1016/j.atmosenv.2016.02.035

Sun, K., Zhu, L., Cady-Pereira, K., Chan Miller, C., Chance, K., Clarisse, L., Coheur, P. F., González Abad, G., Huang, G., Liu, X., Van Damme, M., Yang, K., & Zondlo, M. (2018). A physics-based approach to oversample multi-satellite, multispecies observations to a common grid. *Atmos. Meas. Tech., 11*(12), 6679-6701. doi:10.5194/amt-11-6679-2018

Talbot, R. W., Dibb, J. E., Scheuer, E. M., Kondo, Y., Koike, M., Singh, H. B., Salas, L. B., Fukui, Y., Ballenthin, J. O., Meads, R. F., Miller, T. M., Hunton, D. E., Viggiano, A. A., Blake, D. R., Blake, N. J., Atlas, E., Flocke, F., Jacob, D. J., & Jaegle, L. (1999). Reactive nitrogen budget during the NASA SONEX Mission. *Geophys. Res. Lett., 26*(20), 3057-3060. doi:https://doi.org/10.1029/1999GL900589

Talukdar, R., Burkholder, J., Gilles, M., & Roberts, J. (1997). Atmospheric fate of several alkyl nitrates Part 2UV absorption cross-sections and photodissociation quantum yields. *Journal of the Chemical Society, Faraday Transactions, 93*(16), 2797-2805.

Thomas, K., Berg, M., Boulanger, D., Houben, N., Gressent, A., Nédélec, P., Pätz, H.-W., Thouret, V., & Volz-Thomas, A. (2015). Climatology of NO_y in the troposphere and UT/LS from measurements made in MOZAIC. *Tellus B, 67*(1), 28793. doi:10.3402/tellusb.v67.28793

Thompson, C. R., Wofsy, S. C., Prather, M. J., Newman, P. A., Hanisco, T. F., Ryerson, T. B., Fahey, D. W., Apel, E. C., Brock, C. A., Brune, W. H., Froyd, K., Katich, J. M., Nicely, J. M., Peischl, J., Ray, E., Veres, P. R., Wang, S., Allen, H. M., Asher, E., Bian, H., Blake, D., Bourgeois, I., Budney, J., Bui, T. P., Butler, A., Campuzano-Jost, P., Chang, C., Chin, M., Commane, R., Correa, G., Crounse, J. D., Daube, B., Dibb, J. E., Digangi, J. P., Diskin, G. S., Dollner, M., Elkins, J. W., Fiore, A. M., Flynn, C. M., Guo, H., Hall, S. R., Hannun, R. A., Hills, A., Hintsa, E. J., Hodzic, A., Hornbrook,

R. S., Huey, L. G., Jimenez, J. L., Keeling, R. F., Kim, M. J., Kupc, A., Lacey, F., Lait, L. R., Lamarque, J.-F., Liu, J., Mckain, K., Meinardi, S., Miller, D. O., Montzka, S. A., Moore, F. L., Morgan, E. J., Murphy, D. M., Murray, L. T., Nault, B. A., Neuman, J. A., Nguyen, L., Gonzalez, Y., Rollins, A., Rosenlof, K., Sargent, M., Schill, G., Schwarz, J. P., St. Clair, J. M., Steenrod, S. D., Stephens, B. B., Strahan, S. E., Strode, S. A., Sweeney, C., Thames, A. B., Ullmann, K., Wagner, N., Weber, R., Weinzierl, B., Wennberg, P. O., Williamson, C. J., Wolfe, G. M., & Zeng, L. (2021). The NASA Atmospheric Tomography (ATom) Mission: Imaging the chemistry of the global atmosphere. *B. Am. Meteorol. Soc.*, 1-53. doi:10.1175/bams-d-20-0315.1

Toon, O. B., Maring, H., Dibb, J., Ferrare, R., Jacob, D. J., Jensen, E. J., Luo, Z. J., Mace, G. G., Pan, L. L., Pfister, L., Rosenlof, K. H., Redemann, J., Reid, J. S., Singh, H. B., Thompson, A. M., Yokelson, R., Minnis, P., Chen, G., Jucks, K. W., & Pszenny, A. (2016). Planning, implementation, and scientific goals of the Studies of Emissions and Atmospheric Composition, Clouds and Climate Coupling by Regional Surveys (SEAC^{4}RS) field mission. *J. Geophys. Res.- Atmos., 121*(9), 4967-5009. doi:10.1002/2015jd024297

Trainer, M., Buhr, M. P., Curran, C. M., Fehsenfeld, F. C., Hsie, E. Y., Liu, S. C., Norton, R. B., Parrish, D. D., Williams, E. J., Gandrud, B. W., Ridley, B. A., Shetter, J. D., Allwine, E., & Westberg, H. (1991). Observations and Modeling of the Reactive Nitrogen Photochemistry at a Rural Site. *Journal of Geophysical Research Atmospheres, 96*(D2), 3045-3063. doi:10.1029/90jd02395

Travis, K. R., Heald, C. L., Allen, H. M., Apel, E. C., Arnold, S. R., Blake, D. R., Brune, W. H., Chen, X., Commane, R., Crounse, J. D., Daube, B. C., Diskin, G. S., Elkins, J. W., Evans, M. J., Hall, S. R., Hintsa, E. J., Hornbrook, R. S., Kasibhatla, P. S., Kim, M. J., Luo, G., McKain, K., Millet, D. B., Moore, F. L., Peischl, J., Ryerson, T. B., Sherwen, T., Thames, A. B., Ullmann, K., Wang, X., Wennberg, P. O., Wolfe, G. M., & Yu, F. (2020). Constraining remote oxidation capacity with ATom observations. *Atmos. Chem. Phys., 20*(13), 7753-7781. doi:10.5194/acp-20-7753-2020

Travis, K. R., Jacob, D. J., Fisher, J. A., Kim, P. S., Marais, E. A., Zhu, L., Yu, K., Miller, C. C., Yantosca, R. M., Sulprizio, M. P., Thompson, A. M., Wennberg, P. O., Crounse, J. D., St. Clair, J. M., Cohen, R. C., Laughner, J. L., Dibb, J. E., Hall, S. R., Ullmann, K., Wolfe, G. M., Pollack, I. B., Peischl, J., Neuman, J. A., & Zhou, X. (2016). Why do models overestimate surface ozone in the Southeast United States? *Atmos. Chem. Phys., 16*(21), 13561-13577. doi:10.5194/acp-16-13561-2016

Travis, K. R., Nault, B. A., Crawford, J. H., Bates, K. H., Blake, D. R., Cohen, R. C., Fried, A., Hall, S. R., Huey, L. G., Lee, Y. R., Meinardi, S., Min, K. E., Simpson, I. J., & Ullman, K. (2024). Impact of improved representation of VOC emissions and production of NO_x reservoirs on modeled urban ozone production. *Atmos. Chem. Phys., 2024*, 1-27. doi:10.5194/egusphere-2024-951

Tzortziou, M., Kwong, C. F., Goldberg, D., Schiferl, L., Commane, R., Abuhassan, N., Szykman, J. J., & Valin, L. C. (2022). Declines and peaks in NO2 pollution during the multiple waves of the COVID-19 pandemic in the New York metropolitan area. *Atmos. Chem. Phys., 22*(4), 2399-2417. doi:10.5194/acp-22-2399-2022

Valin, L. C., Russell, A. R., & Cohen, R. C. (2013). Variations of OH radical in an urban plume inferred from NO2 column measurements. *Geophysical Research Letters, 40*(9), 1856-1860. doi:https://doi.org/10.1002/grl.50267

Van Geffen, J., Boersma, K., Van Roozendael, M., Hendrick, F., Mahieu, E., De Smedt, I., Sneep, M., & Veefkind, J. (2015). Improved spectral fitting of nitrogen dioxide from OMI in the 405–465 nm window. *Atmospheric Measurement Techniques, 8*(4), 1685-1699.

van Geffen, J., Boersma, K. F., Eskes, H., Sneep, M., ter Linden, M., Zara, M., & Veefkind, J. P. (2020). S5P TROPOMI NO2 slant column retrieval: method, stability, uncertainties and comparisons with OMI. *Atmos. Meas. Tech., 13*(3), 1315-1335. doi:10.5194/amt-13-1315-2020

Verhoelst, T., Compernolle, S., Pinardi, G., Lambert, J.-C., Eskes, H., Eichmann, K., Fjæraa, A. M., Granville, J., Niemeijer, S., Cede, A., Tiefengraber, M., Hendrick, F., Pazmiño, A., Bais, A., Bazureau, A., Boersma, K. F., Bognar, K., Dehn, A., Donner, S., Елохов, А. С., Gebetsberger, M., Goutail, F., Michel Grutter de la, M., Груздев, А. Н., Gratsea, M., Hansen, G., Irie, H., Jepsen, N., Kanaya, Y., Karagkiozidis, D., Kivi, R., Kreher, K., Levelt, P. F., Liu, C., Müller, M., Navarro-Comas, M., Piters, A., Pommereau, J. P., Portafaix, T., Prados-Román, C., Puentedura, O., Querel, R., Remmers, J., Richter, A., Rimmer, J., Cárdenas, C. R., Miguel, L. S. d., Sinyakov, V. P., Stremme, W., Strong, K., Roozendaël, M. V., Veefkind, J. P., Wagner, T., Wittrock, F., Gonzalez, M. Y., & Zehner, C. (2021). Ground-Based Validation of the Copernicus Sentinel-5p TROPOMI NO_2 Measurements With the NDACC ZSL-DOAS, MAX-DOAS and Pandonia Global Networks. *Atmospheric Measurement Techniques, 14*(1), 481-510. doi:10.5194/amt-14-481-2021

Villalta, P. W., & Howard, C. J. (1996). Direct kinetics study of the $CH_3C(O)O_2$+ NO reaction using chemical ionization mass spectrometry. *The Journal of Physical Chemistry, 100*(32), 13624-13628.

Vohra, K., Marais, E. A., Bloss, W. J., Schwartz, J., Mickley, L. J., Van Damme, M., Clarisse, L., & Coheur, P.-F. (2022). Rapid rise in premature mortality due to anthropogenic air pollution in fast-growing tropical cities from 2005 to 2018. *Science Advances, 8*(14). doi:10.1126/sciadv.abm4435

Volz-Thomas, A., Berg, M., Heil, T., Houben, N., Lerner, A., Petrick, W., Raak, D., & Pätz, H. W. (2005). Measurements of total odd nitrogen (NO_y) aboard MOZAIC in-service aircraft: instrument design, operation and performance. *Atmos. Chem. Phys., 5*(3), 583-595. doi:10.5194/acp-5-583-2005

Wang, Y., Jacob, D. J., & Logan, J. A. (1998). Global simulation of tropospheric O3-NO x -hydrocarbon chemistry: 1. Model formulation. *Journal* *of Geophysical Research: Atmospheres, 103*(D9), 10713-10725. doi:https://doi.org/10.1029/98JD00158

Wei, N., Marais, E. A., Lu, G., Ryan, R. G., & Sauvage, B. (2024). Characterization of reactive nitrogen in the global upper troposphere using recent and historical commercial and research aircraft campaigns and GEOS-Chem. *EGUsphere, 2024*, 1-23. doi:10.5194/egusphere-2024-3388

Weinheimer, A. J. (2006). Chemical Methods: Chemiluminscence, Chemical Amplification, Electrochemistry, and Derivation. In *Analytical Techniques for Atmospheric Measurement* (pp. 311-360).

Weinheimer, A. J., Walega, J. G., Ridley, B. A., Gary, B. L., Blake, D. R., Blake, N. J., Rowland, F. S., Sachse, G. W., Anderson, B. E., & Collins, J. E. (1994). Meridional distributions of NO_x, NO_y, and other species in the lower stratosphere and upper troposphere during AASE II. *Geophys. Res. Lett., 21*(23), 2583-2586. doi:https://doi.org/10.1029/94GL01897

Wesely, M. L. (1989). Parameterization of surface resistances to gaseous dry deposition in regional-scale numerical models. *Atmospheric Environment (1967), 23*(6), 1293-1304. doi:https://doi.org/10.1016/0004-6981(89)90153-4

Wooldridge, P. J., Perring, A. E., Bertram, T. H., Flocke, F. M., Roberts, J. M., Singh, H. B., Huey, L. G., Thornton, J. A., Wolfe, G. M., Murphy, J. G., Fry, J. L., Rollins, A. W., LaFranchi, B. W., & Cohen, R. C. (2010). Total Peroxy Nitrates (PNs) in the atmosphere: the Thermal Dissociation-Laser Induced Fluorescence (TD-LIF) technique and comparisons to speciated PAN measurements. *Atmos. Meas. Tech., 3*(3), 593-607. doi:10.5194/amt-3-593-2010

Woollatt, G. (2015). Quality Assurance of Continuous Emission Monitoring Systems: A practitioner’s guide/technical report. *Clean Air Journal, 25*(2).

Worden, H. M., Bowman, K. W., Kulawik, S. S., & Aghedo, A. M. (2011). Sensitivity of outgoing longwave radiative flux to the global vertical distribution of ozone characterized by instantaneous radiative kernels from Aura-TES. *J. Geophys. Res., 116*(D14). doi:10.1029/2010jd015101

Worton, D. R., Reeves, C. E., Penkett, S. A., Sturges, W. T., Slemr, J., Oram, D. E., Bandy, B. J., Bloss, W. J., Carslaw, N., Davey, J., Emmerson, K. M., Gravestock, T. J., Hamilton, J. F., Heard, D. E., Hopkins, J. R., Hulse, A., Ingram, T., Jacob, M. J., Lee, J. D., Leigh, R. J., Lewis, A. C., Monks, P. S., & Smith, S. C. (2010). Alkyl nitrate photochemistry during the tropospheric organic chemistry experiment. *Atmospheric Environment, 44*(6), 773-785. doi:https://doi.org/10.1016/j.atmosenv.2009.11.038

Wu, N., Geng, G., Yan, L., Bi, J., Li, Y., Tong, D., Zheng, B., & Zhang, Q. (2021a). Improved spatial representation of a highly resolved emission inventory in China: evidence from TROPOMI measurements. *Environmental Research Letters, 16*(8), 084056. doi:10.1088/1748-9326/ac175f

Wu, S., Huang, B., Wang, J., He, L., Wang, Z., Yan, Z., Lao, X., Zhang, F., Liu, R., & Du, Z. (2021b). Spatiotemporal mapping and assessment of daily ground NO2 concentrations in China using high-resolution TROPOMI retrievals. *Environmental Pollution, 273*, 116456. doi:https://doi.org/10.1016/j.envpol.2021.116456

Wu, X., Deng, L., Song, X., & Zhang, G. J. (2007). Coupling of convective momentum transport with convective heating in global climate simulations. *Journal of the Atmospheric Sciences, 64*(4), 1334-1349.

Ye, C., Heard, D. E., & Whalley, L. K. (2017). Evaluation of Novel Routes for NO_x Formation in Remote Regions. *Environmental Science & Technology, 51*(13), 7442-7449. doi:10.1021/acs.est.6b06441

Yuen, B., & Kumssa, A. (2011). Africa and Asia: Two of the World's Fastest Growing Regions. *Climate change and sustainable urban development in Africa and Asia*, 3-18.

Zahn, A., Brenninkmeijer, C. A. M., Asman, W. A. H., Crutzen, P. J., Heinrich, G., Fischer, H., Cuijpers, J. W. M., & van Velthoven, P. F. J. (2002). Budgets of O_3 and CO in the upper troposphere: CARIBIC passenger aircraft results 1997–2001. *Journal of Geophysical Research-Atmospheres, 107*(D17), ACH 6-1-ACH 6-20. doi:https://doi.org/10.1029/2001JD001529

Zhai, S., Jacob, D. J., Franco, B., Clarisse, L., Coheur, P., Shah, V., Bates, K. H., Lin, H., Dang, R., Sulprizio, M. P., Huey, L. G., Moore, F. L., Jaffe, D. A., & Liao, H. (2024). Transpacific Transport of Asian Peroxyacetyl Nitrate (PAN) Observed from Satellite: Implications for Ozone. *Environmental Science & Technology, 58*(22), 9760-9769. doi:10.1021/acs.est.4c01980

Zhang, L., Chen, Y., Zhao, Y., Henze, D. K., Zhu, L., Song, Y., Paulot, F., Liu, X., Pan, Y., Lin, Y., & Huang, B. (2018). Agricultural Ammonia Emissions in China: Reconciling Bottom-Up and Top-Down Estimates. *Atmospheric Chemistry and Physics, 18*(1), 339-355. doi:10.5194/acp-18-339-2018

Zhang, L., Gong, S., Padro, J., & Barrie, L. (2001). A size-segregated particle dry deposition scheme for an atmospheric aerosol module. *Atmospheric Environment, 35*(3), 549-560. doi:https://doi.org/10.1016/S1352-2310(00)00326-5

Zhang, Q., Streets, D. G., He, K., Wang, Y., Richter, A., Burrows, J. P., Uno, I., Jang, C., Chen, D., Yao, Z., & Lei, Y. (2007). NO_x Emission Trends for China, 1995–2004: The View From the Ground and the View From Space. *Journal of Geophysical Research Atmospheres, 112*(D22). doi:10.1029/2007jd008684

Zheng, B., Chevallier, F., Ciais, P., Yin, Y., & Wang, Y. (2018). On the Role of the Flaming to Smoldering Transition in the Seasonal Cycle of African Fire Emissions. *Geophysical Research Letters, 45*(21), 11,998-912,007. doi:https://doi.org/10.1029/2018GL079092

Zheng, W., Flocke, F. M., Tyndall, G. S., Swanson, A., Orlando, J. J., Roberts, J. M., Huey, L. G., & Tanner, D. J. (2011). Characterization of a thermal decomposition chemical ionization mass spectrometer for the measurement of peroxy acyl nitrates (PANs) in the atmosphere. *Atmos. Chem. Phys., 11*(13), 6529-6547. doi:10.5194/acp-11-6529-2011

Appendix A: Published Paper

Wei, N., et al. (2025). Characterization of reactive oxidized nitrogen in the global upper troposphere using recent and historic commercial and research aircraft campaigns and GEOS-Chem. *Atmos. Chem. Phys.*, 25, 7925–7940. https://doi.org/10.5194/acp-25-7925-2025.

Atmos. Chem. Phys., 25, 7925–7940, 2025
https://doi.org/10.5194/acp-25-7925-2025

Atmospheric
Chemistry
and Physics
Open Access
EGU

Research article

Characterization of reactive oxidized nitrogen in the global upper troposphere using recent and historic commercial and research aircraft campaigns and GEOS-Chem

Nana Wei[1], **Eloise A. Marais**[1], **Gongda Lu**[1,a], **Robert G. Ryan**[1,b], **and Bastien Sauvage**[2]
[1]Department of Geography, University College London, London, UK
[2]Laboratoire d’Aérologie, Université de Toulouse, CNRS, Université Toulouse III Paul Sabatier, Toulouse, France
[a]now at: the Satellite Application Center for Ecology and Environment, Ministry of Ecology and Environment, Beijing, China
[b]now at: School of Geography, Earth and Atmospheric Science, University of Melbourne, Melbourne, Australia

Correspondence: Nana Wei (nana.wei.21@ucl.ac.uk) and Eloise A. Marais (e.marais@ucl.ac.uk)

Received: 30 October 2024 – Discussion started: 3 December 2024
Revised: 12 May 2025 – Accepted: 13 May 2025 – Published: 25 July 2025

Abstract. Reactive oxidized nitrogen (NO_y) in the upper troposphere (UT) influences global climate, air quality, and tropospheric oxidants, but this understanding is limited by knowledge of the relative contributions of individual NO_y components in this undersampled layer. Here, we use sporadic NASA DC-8 aircraft campaign observations, after screening for plumes and stratospheric influence, to characterize UT NO_y composition and to evaluate current knowledge of UT NO_y as simulated by the GEOS-Chem model. The use of DC-8 data follows confirmation that these intermittent data reproduce NO_y seasonality from routine commercial aircraft observations (2003–2019), supporting the use of DC-8 data to characterize UT NO_y. We find that peroxyacetyl nitrate (PAN) dominates UT NO_y (30 %–64 % of NO_y), followed by nitrogen oxides ($NO_x \equiv NO + NO_2$) (6 %–18 %), peroxynitric acid (HNO_4) (6 %–13 %), and nitric acid (HNO_3) (7 %–11 %). Methyl peroxy nitrate (MPN) makes an outsized contribution to NO_y (14 %–24 %) over the Southeast US relative to the other regions sampled (2 %–7 %). GEOS-Chem, sampled along DC-8 flights, exhibits much weaker seasonality than the DC-8, underestimating summer and spring NO_y and overestimating winter and autumn NO_y. The model consistently overestimates peroxypropionyl nitrate (PPN) by ∼ 10–16 pptv or 10 %–90 % and underestimates NO_2 by 6–36 pptv or 31 %–65 %, as the model is missing PPN photolysis. A model underestimate in MPN of at least ∼ 50 pptv (13-fold) over the Southeast US results from uncertainties in processes that sustain MPN production as air ages. Our findings highlight that a greater understanding of UT NO_y is critically needed to determine its role in the nitrogen cycle, air pollution, climate, and the abundance of oxidants.

1 Introduction

Reactive oxidized nitrogen (NO_y) in the upper troposphere impacts global climate, surface air quality, and the oxidizing capacity of the whole troposphere (Mickley et al., 1999; Bradshaw et al., 2000; Dahlmann et al., 2011; Worden et al., 2011). NO_y is an important climate driver because tropospheric ozone (O_3) production is limited by the availability of NO_y, particularly in the upper troposphere where the radiative forcing efficiency of O_3 peaks (Dahlmann et al., 2011; Worden et al., 2011; Rap et al., 2015). The influence on tropospheric O_3 production also affects the abundance of the main atmospheric oxidant, the hydroxyl radical (OH), thus altering the lifetimes of the longer-lived greenhouse gas

Published by Copernicus Publications on behalf of the European Geosciences Union.

methane and the air pollutants carbon monoxide (CO) and volatile organic compounds (VOCs) (Murray et al., 2013; Seltzer et al., 2015).

Knowledge of dominant daytime NO_y compounds, sources, chemistry, fate, and persistence in the upper troposphere has been largely informed by observations and models used as part of research and commercial aircraft campaigns (Boersma et al., 2011; Marais et al., 2018; Silvern et al., 2018; Travis et al., 2016, 2020). Instruments onboard research aircraft that sample the upper troposphere, in particular the recently retired NASA DC-8 platform, have undergone substantial development to directly measure and derive estimates of a large suite of upper tropospheric NO_y compounds. These include nitrogen oxides ($NO_x \equiv NO + NO_2$), peroxyacetyl nitrate (PAN), and other prominent PAN-type compounds, nitric acid (HNO_3), peroxynitric acid (HNO_4), alkylnitrates (ALKNs) and, more recently, methyl peroxy nitrate (MPN).

These aircraft campaigns have confirmed that sources of NO_y to the upper troposphere are dominated by lightning NO_x emissions (Levy et al., 1999; Gressent et al., 2014, 2016; Marais et al., 2018), causing a seasonal maximum in NO_y in the summer months and a minimum in the winter in parts of the world, such as the northern midlatitudes, where there is large seasonal variability in lightning activity (Blakeslee et al., 2014; Stratmann et al., 2016). Other NO_y source contributors include NO_x emissions from cruising altitude aircraft (Brasseur et al., 1996), stratospheric downwelling of air masses laden with HNO_3 and NO_2 that also promote prompt formation of PANs on mixing with cold upper tropospheric air (Levy et al., 1980; Jacob et al., 2010; Liang et al., 2011), deep convective uplift of surface pollution (Ehhalt et al., 1992; Jaeglé et al., 1998; Bertram et al., 2007), and aged air masses, initially very photochemically active, that accumulate MPN (Nault et al., 2015).

Chemical cycling of dominant daytime NO_y components, informed by past review and measurement compilation studies of the free troposphere (Emmons et al., 1997; Bradshaw et al., 2000), is illustrated in Fig. 1. During the day, NO and NO_2 are in a photostationary steady state, as NO oxidation, mostly by O_3, is balanced by NO_2 photolysis. NO_x also reacts to form reservoir compounds. For NO_2, these include HNO_3 from reaction with OH, PANs from reaction with peroxy acyl radicals (RC(O)OO), HNO_4 from reaction with the hydroperoxyl radical (HO_2), and MPN from reaction with the methyl peroxy radical (CH_3O_2). PANs in the upper troposphere are typically dominated by PAN, followed by peroxypropionyl nitrate (PPN) (Singh, 1987; Roberts, 1990; Roberts et al., 1998, 2002). For NO, reservoir compounds include ALKNs from reaction with non-acyl peroxy radicals (RO_2). Recycling of reservoir compounds back to NO_x is dominated by photolysis, as thermally labile peroxy nitrates (PNs) including PANs, HNO_4, and MPN are stable against decomposition in the cold upper troposphere (Huey, 2007). This recycling, along with NO_y sources to the upper troposphere, sustains upper tropospheric NO_x concentrations at ∼ 30 pptv over the remote ocean and ∼ 100 pptv over polluted landmasses (Marais et al., 2018, 2021; Shah et al., 2023). Stable NO_x reservoir compounds are transported long distances before subsiding and decomposing on warming, thus supplying other parts of the world with oxidants (HO_x) and O_3 precursors (NO_x and peroxy radicals) (Schultz et al., 1999). Loss processes in the dry upper troposphere are slow and dominated by subsidence, resulting in long NO_y lifetimes of 10–20 d (Logan, 1983; Prather and Jacob, 1997). Similarly, NO_x has a lifetime of about a week compared to less than a day in the boundary layer (< 2 km) (Jaeglé et al., 1998).

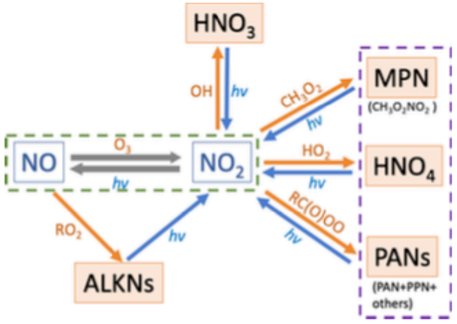

Figure 1. Dominant daytime reactive oxidized gas-phase nitrogen components and reaction pathways in the upper troposphere. Arrow colours distinguish formation (orange) and photolytic ($h\nu$) decomposition (blue) of reservoir compounds. Dashed boxes indicate compounds of the NO_x family (green) and those classed as peroxy nitrates (purple). "R" in RC(O)OO and RO_2 represents an alkyl group.

Nighttime NO_y chemistry is also important, but aircraft campaign measurements of the nocturnal upper troposphere mostly consist of total NO_y from commercial aircraft campaigns. The nighttime chemistry not shown in Fig. 1 includes NO reaction with OH, forming nitrous acid (HONO) that accumulates in the absence of photolysis as well as NO_2 reaction with O_3 to form the nitrate radical (NO_3), which further reacts with NO_2 to produce N_2O_5, a precursor of aerosol nitrate (pNO_3) (Bradshaw et al., 2000).

Modelling studies evaluating the best understanding of NO_y in the upper troposphere routinely identify stark discrepancies between observed and modelled total NO_y, NO_x, and the ratio of NO-to-NO_2 in the upper layers of the troposphere (Jaeglé et al., 1998; Talbot et al., 1999; Bertram et al., 2007; Hudman et al., 2007; Liang et al., 2011; Nault et al., 2015; Huntrieser et al., 2016; Travis et al., 2016; Fisher et al., 2018; Silvern et al., 2018; Lee et al., 2022; Cohen et al., 2023). These studies have either focused on a few NO_y components or a single aircraft campaign. A more holistic investigation of all NO_y components is needed, as advocated by Murray et al. (2021), to reduce uncertainties in knowledge of the current, past, and potential future abundances of tropospheric oxidants. Past studies have also documented the challenges of examining measurements made in the upper troposphere. These include screening for stratospheric influence, determining the height of the chemical tropopause, and selecting observations and campaigns that are climatologically representative of a standard atmosphere (Weinheimer et al., 1994; Fuelberg et al., 2000; Bertram et al., 2007; Barth et al., 2015; Huntrieser et al., 2016). Instruments measuring NO_2 are also susceptible to interference from decomposition of the least thermally stable NO_x reservoir compounds, HNO_4 and MPN, that are abundant in the cold upper troposphere (Ryerson et al., 2000; Shah et al., 2023). NO_y from these same instruments can also be biased by decomposition of non-NO_y fixed nitrogen compounds prevalent in the upper troposphere, such as hydrogen cyanide (HCN) (Bradshaw et al., 1998).

Here, we use NASA DC-8 research and In-service Aircraft for a Global Observing System (IAGOS) commercial aircraft campaign measurements, each spanning more than a decade, to characterize global NO_y seasonality and composition in the upper troposphere. This follows careful campaign and data selection to isolate observations sampling the upper troposphere under standard conditions for broad assessment of consistent NO_y seasonality between DC-8 and routine commercial aircraft campaign observations. We go on to use the DC-8 data to critique contemporary understanding of upper tropospheric NO_y as simulated by the GEOS-Chem model.

2 Materials and methods

2.1 Research aircraft observations of total and components of NO_y

The DC-8 research aircraft has sampled ambient air covering the near full extent of the troposphere since its maiden campaign in 1985 (Culter, 2009). Many of the initial campaigns included instruments that measured a subset of the NO_y components shown in Fig. 1, typically continuous measurements of total NO_y, NO, HNO_3, PAN and PPN, and whole air sampler (WAS) collection and laboratory detection of C1–C5 ALKNs (Singh et al., 1999). Since 2004, DC-8 campaigns have included continuous measurements of HNO_4, other PAN-type species, and total PNs (Singh et al., 2006). Given this, we only consider DC-8 campaigns with a relatively consistent suite of instruments that mostly sampled well-mixed air representative of a climatologically standard atmosphere. These criteria eliminate the summer 2004 Intercontinental Chemical Transport Experiment-North America (INTEX-NA) campaign (Singh et al., 2006; Singh et al., 2009), which is the only DC-8 campaign since 2004 not to include a NO_x and NO_y chemiluminescence analyser, and the summer 2012 Deep Convective Clouds and Chemistry (DC3) campaign, which targeted convective thunderstorms influenced by fresh surface pollution and lightning NO_x emissions (Barth et al., 2015).

The DC-8 campaigns we use are the Arctic Research of the Composition of the Troposphere from Aircraft and Satellites (ARCTAS) over the Arctic and sub-Arctic in spring and summer 2008 (Jacob et al., 2010), the Studies of Emissions and Atmospheric Composition, Clouds and Climate Coupling by Regional Surveys ($SEAC^4RS$) over the Southeast US in late summer and early autumn 2013 (Toon et al., 2016), the Korea-United States Air Quality (KORUS-AQ) over South Korea in late spring and early summer 2016 (Crawford et al., 2021), and the Atmospheric Tomography Mission (ATom), which included four sub-campaigns along the same flight path from pole to pole over the Atlantic and Pacific Oceans in all four seasons from 2016 to 2018 (Thompson et al., 2021). ATom sub-campaigns are ATom-1 in July–August, ATom-2 in January–February, ATom-3 in September–October, and ATom-4 in April–May. The data for these campaigns are from NASA data portals for each campaign, downloaded as merged 1 min files for ARCTAS (NASA, 2009), $SEAC^4RS$ (NASA, 2015), and KORUS-AQ (NASA, 2017) and as two separate merged files for ATom, with the WAS C1–C5 ALKNs data at variable time intervals of 40 s, 1, and 2 min and without the WAS C1–C5 ALKNs data at 1 min resolution (NASA, 2021).

Figure 2 shows the global sampling extent of the upper troposphere by NASA DC-8 after applying filtering criteria to the data to isolate observations representative of photochemical steady state (PSS) conditions. For this, we select daytime (08:30–15:30 local solar time or LST) observations within a wide pressure range from 180 hPa (~ 8 km) to the DC-8 ceiling of 450 hPa (~ 12 km). This captures the full vertical extent of the midlatitude upper troposphere but not the tropics. The tropical tropopause, according to NASA Modern-Era Retrospective analysis for Research and Applications version 2 (MERRA-2) meteorology, extends to ~ 16 km. We separate the stratosphere from the troposphere with a tropopause definition that can be applied to all datasets. We remove data with observed O_3 concentrations above thresholds that represent the location of the chemical tropopause (Zahn et al., 2002). The thresholds we use are a single year-round value for the tropics (20° N to 20° S) of 100 ppbv (Dameris, 2015) and seasonally varying values everywhere else calculated using the day-of-year dependent O_3 tropopause equation derived by Zahn et al. (2002) from the inverse relationship between O_3 and CO observations from commercial aircraft campaigns. These are 120 ppbv in spring, 103 ppbv in summer, 74 ppbv in autumn, and 91 ppbv in winter. We also screen for stratospheric intrusions (identified as observations with $O_3/CO > 1.25\,\mathrm{mol\,mol^{-1}}$) (Hudman et al., 2007), fresh NO_x emissions ($NO_y/NO < 3\,\mathrm{mol\,mol^{-1}}$), fresh convection (large (> 10 nm diameter) condensation nuclei $> 10^4\,\mathrm{cm^{-3}}$), biomass burning plumes (CO > 200 ppbv and acetonitrile > 200 pptv) (Shah et al., 2023) as well as instances where NO_2 photolysis frequencies are approximately

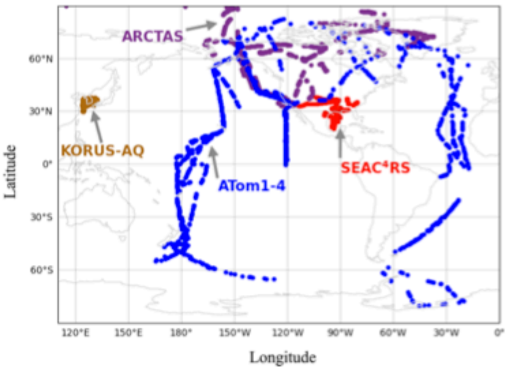

Figure 2. Extent of NASA DC-8 sampling of the upper troposphere under standard, steady state conditions. Colours distinguish ARCTAS (plum), SEAC^{4}RS (red), KORUS-AQ (brown), and ATom (blue). ATom points are 1 min resolution data.

zero. The latter removes high latitude ATom measurements obtained at 08:30–15:30 LST under dark conditions during polar twilight or polar night. The data that are retained correspond to solar zenith angles $\leq 80°$ in polar regions and $\leq 60°$ at other latitudes. The proportion of observations at 450–180 hPa is 42 %–50 % for ATom and 16 %–37 % for the other campaigns. After applying all other data screening, 20 % of all data are retained for ATom and 7 %–11 % for the other campaigns.

The DC-8 instruments measuring NO_y components (Fig. 1) that are common to all campaigns include a chemiluminescence instrument measuring NO, NO_2, and total NO_y (Ryerson et al., 2000; Pollack et al., 2010; Bourgeois et al., 2022), a chemical ionization mass spectrometer (CIMS) measuring HNO_3 (Crounse et al., 2006), a CIMS measuring HNO_4, PAN, PPN, and other PANs (Huey, 2007), and a Whole Air Sampler (WAS) collecting samples analysed in the laboratory using gas chromatography with flame ionization and atomic emission to detect C1–C5 ALKNs (Blake et al., 2003). The other PANs measured with the CIMS include peroxyacryloyl nitrate (APAN), peroxyisobutyryl nitrate (PiBN), peroxybutyryl nitrate (PBN), and peroxybenzoyl nitrate (PBZN). Other instruments deployed for select campaigns are Thermal-Dissociation Laser Induced Fluorescence (TD-LIF) measuring NO_2, total PNs, and total ALKNs (ARCTAS, KORUS-AQ, SEAC^{4}RS) (Day et al., 2002) and the PAN and Trace Hydrohalocarbon ExpeRiment (PANTHER) instrument measuring PAN (ATom). There are also TD-LIF methyl peroxy nitrate (MPN) measurements reported in the SEAC^{4}RS dataset and derived for ARCTAS by Browne et al. (2011).

Concentrations of NO_2 in the upper troposphere are close to chemiluminescence instrument uncertainty (Pollack et al., 2010; Bourgeois et al., 2022), and the measurements include interference from decomposition of NO_x reservoir compounds in the instrument inlet. The Reed et al. (2016b) temperature-dependent inlet temperature decomposition profiles of individual NO_x reservoir compounds for an instrument similar to that operated on the DC-8 suggest interference of 80 %–100 % MPN and 15 %–45 % HNO_4 for the typical inlet temperature range of the DC-8 chemiluminescence instrument of 20–30 °C (Bourgeois et al., 2022). For the campaigns that measured HNO_4 and derived or measured MPN, this amounts to 13–27 pptv for ARCTAS and 71–92 pptv for SEAC^{4}RS. Given this, we instead calculate NO_2 using the NO–NO_2 photochemical steady state (PSS) approximation, as is now standard (Travis et al., 2016; Shah et al., 2023; Horner et al., 2024). Conversion of NO to NO_2, mostly (75 %) due to oxidation by O_3 in the upper troposphere (Silvern et al., 2018), is balanced by NO_2 photolysis back to NO:

$$NO \xrightarrow{O_3/HO_2/BrO} NO_2 \tag{R1}$$

$$NO_2 \xrightarrow{h\nu} NO. \tag{R2}$$

As NO_x is in steady state for the daylight observations we isolate, NO_2 can be calculated as follows:

$$NO_2 = NO \times \left(\frac{k_1\,[O_3] + k_2\,[HO_2] + k_3\,[BrO]}{j_{NO_2}} \right). \tag{1}$$

Compounds in square brackets are in molecules cm^{-3}. NO and NO_2 are in pptv. Terms not introduced yet include the NO_2 photolysis frequency, j_{NO_2}, in s^{-1}; bromine monoxide (BrO); and rate constants of NO oxidation (Reaction R1) (k_{1-3}) in cm^3 molecule^{-1} s^{-1}. Temperature-dependent values of k_{1-3} are those recommended by the Jet Propulsion Laboratory (JPL) (Burkholder et al., 2020), calculated using DC-8 ambient temperature measurements. NO, [O_3], and j_{NO_2} are from the DC-8 measurements, and [HO_2] is from the DC-8 measurements for all campaigns except SEAC^{4}RS when it was not measured. We use GEOS-Chem (detailed in Sect. 2.3) simulated [HO_2] to estimate SEAC^{4}RS PSS NO_2. [BrO] is obtained from GEOS-Chem for all campaigns. NO is also converted to NO_2 by organic peroxy radicals (RO_2), but we ignore this reaction as it is relatively insignificant throughout the free troposphere (Shah et al., 2023).

The NO_y components not measured during specific campaigns are inferred. These include HNO_4 for KORUS-AQ and ATom-3-4, PPN for ATom-1-2, and MPN for ARCTAS, ATom-1-4, and KORUS-AQ. The approaches used to infer these values differ, informed by the results; therefore, a detailed description of this inference is provided in Sect. 3.2.

2.2 Commercial aircraft observations of total NO_y

We use routine observations of upper tropospheric total NO_y from instruments on commercial long-haul passenger aircraft to determine if the intermittency and brevity of DC-8 campaign observations are representative of climatological conditions. The In-service Aircraft for a Global Observing System (IAGOS) European research infrastructure (Boulanger et al., 2018) provides routine in situ measurements of NO_y (Petzold et al., 2015). These are available from two IAGOS programmes: the Measurement of Ozone and Water Vapor by Airbus In-Service Aircraft (MOZAIC) (Marenco et al., 1998) from 2001 to 2005 (Volz-Thomas et al., 2005) and the Civil Aircraft for the Regular Investigation of the Atmosphere Based on an Instrument Container (CARIBIC) since December 2004 (Brenninkmeijer et al., 2007; Stratmann et al., 2016).

We consider the MOZAIC and CARIBIC observations together (collectively named IAGOS), as both programmes employed a chemiluminescence instrument with the same NO_y detection technique (Volz-Thomas et al., 2005; Brenninkmeijer et al., 2007). Direct intercomparison of NO_y is not possible, as there is no overlap in MOZAIC and CARIBIC NO_y. Data from 2003 to 2019 are used: 2003–2005 for MOZAIC and 2005–2019 for CARIBIC. We isolate daytime, upper tropospheric observations by applying the same O_3 tropopause, stratospheric O_3 intrusion, and daytime filtering as is applied to DC-8 data (Sect. 2.1), using IAGOS O_3 and CO measurements. There are no NO_2 photolysis frequency measurements, but the requirement for spatial coincidence with ATom excludes polar twilight and night measurements at high latitudes. We do not screen for observations impacted by fresh emissions, vertical convection, or biomass burning plumes, due to unavailability of concurrent measurements of suitable chemical tracers in the IAGOS data. As we consider 17 years of IAGOS data, we assume that the influence of these is dampened in the long-term median of NO_y. Both the IAGOS and DC-8 data are gridded to the same 2° latitude × 2.5° longitude grid.

2.3 The GEOS-Chem model

We use the GEOS-Chem global 3D chemical transport model version 13.0.2 (https://doi.org/10.5281/zenodo.4681204, The International GEOS-Chem User Community, 2021) to represent contemporary understanding of upper tropospheric NO_y for comparison to DC-8. The model is driven with consistent MERRA-2 assimilated meteorology at $2^\circ \times 2.5^\circ$ (latitude × longitude) over 47 vertical layers from the surface of the Earth to 0.01 hPa. The model emissions local to the upper troposphere include cruising altitude aircraft from the Aviation Emissions Inventory Code (AEIC) (Stettler et al., 2011) and lightning emissions as described in Murray et al. (2012). Surface emissions of NO_x and VOC precursors of ALKNs and PNs are from the anthropogenic Community Emissions Data System (CEDS) inventory of Hoesly et al. (2018); the Model of Emissions of Gases and Aerosols from Nature (MEGAN) biogenic VOC inventory version 2.1 (Guenther et al., 2012); the soil NO_x emission inventory of Hudman et al. (2012); and the Global Fire Emissions Database version 4 with small fires (GFED4s) for open burning of biomass (Giglio et al., 2013). Wet deposition of gas-phase HNO_3, the terminal sink for NO_y subsiding from the upper troposphere, includes in-cloud (rainout) and below-cloud (washout) scavenging as detailed in Amos et al. (2012) and enhanced scavenging as described by Luo et al. (2020).

We sample the model at the same time and location as the DC-8 observations using the ObsPack diagnostic (https://www.esrl.noaa.gov/gmd/ccgg/obspack/, last access: 23 October 2021), following a minimum 10-month spin-up preceding each campaign to initialize chemistry and large-scale circulation throughout the troposphere. Modelled components of NO_y include NO, NO_2, HNO_3, HNO_4, PAN, PPN, peroxymethacroyl nitrate (MPAN), MPN, and ALKNs.

3 Results and discussion

3.1 DC-8 campaign NO_y seasonality and budget closure

Figure 3 compares seasonality in UT NO_y from IAGOS and DC-8. Most of the overlap is with ATom along the North Atlantic flight corridor in all seasons, ARCTAS over the Canadian Arctic and Greenland in March–May (MAM) and June–August (JJA), and $SEAC^4RS$ over the Southeast US in September–November (SON). IAGOS NO_y exhibits similar peaks in spring (563 pptv) and summer (565 pptv), due to intensive seasonal lightning in the Northern Hemisphere (Stratmann et al., 2016). The decline in this source decreases NO_y in autumn to 365 pptv, and NO_y further decreases in winter to an annual minimum of 284 pptv.

DC-8 NO_y seasonality is similar to that of IAGOS, though the magnitude of DC-8 NO_y is consistently, on average, ∼ 130 pptv (range of 80 pptv in SON to 170 pptv in DJF) less than IAGOS NO_y in all seasons. The ∼ 130 pptv greater IAGOS NO_y likely results from differences in sampling altitudes. The two campaigns sample distinct altitude ranges of the upper portion of the upper troposphere centred at ∼ 240 hPa (∼ 10 km) for IAGOS and a wider vertical extent of the lower portion of the upper troposphere centred at ∼ 360 hPa (∼ 1.5 km below IAGOS) for DC-8 (Fig. S1 in the Supplement). There is a general pattern of a steep increase in NO_y with altitude, with the exception of IAGOS layers located near 300 hPa in March–May and September–November (Fig. S1). Average NO_y is similar between the two campaigns for the rare instances that DC-8 and IAGOS sample the same pressure layers (Fig. S1). Another minor factor may be IAGOS NO_y instrument interference from HCN. The IAGOS chemiluminescence instruments use a hydrogen (H_2) reagent to convert oxygenated nitrogen compounds to NO, whereas DC-8 uses CO, a compound not permitted on commercial aircraft (Bradshaw et al., 1998; Volz-Thomas et al., 2005; Thomas et al., 2015). The H_2 reagent

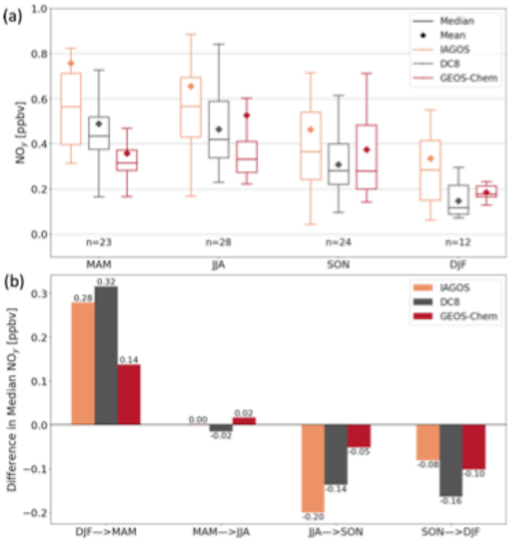

Figure 3. Seasonality of Northern Hemisphere upper tropospheric NO$_y$. Panels show seasonal means and medians **(a)** and seasonal transitions **(b)** of collocated gridded 2° × 2.5° NO$_y$ from IAGOS (orange), DC-8 (grey), and GEOS-Chem (red). Data in **(a)** are medians (lines), 25th and 75th percentiles (boxes), and means (diamonds). Inset text in **(a)** gives the number (n) of overlapping grid cells. Seasonality in **(b)** is the change in median NO$_y$ in **(a)** from one season to the next.

converts anywhere from 2 % to 20 % of HCN to NO$_y$ (Weinheimer, 2006). HCN ambient concentrations typically seasonally vary from ∼ 200 to 300 pptv in the upper troposphere, amounting to an interference of 4–60 pptv (Li et al., 2003; Le Breton et al., 2013).

Figure 4 shows the relationship between the sum of individual NO$_y$ components and total NO$_y$ for each DC-8 campaign. We use these scatterplots to determine whether most NO$_y$ components are measured in each campaign, given our intention to use DC-8 to assess contemporary understanding of upper tropospheric NO$_y$. The instruments and individual components of NO$_y$ summed for comparison with total NO$_y$ are listed in Table 1. The measured components include NO; PSS NO$_2$ (Eq. 1); HNO$_3$; PAN measured as PAN for all ATom sub-campaigns and as part of total PNs for ARCTAS, SEAC^{4}RS, and KORUS-AQ; HNO$_4$ measured as HNO$_4$ for ATom-1 and -2 and as part of total PNs for ARCTAS, SEAC^{4}RS, and KORUS-AQ; C1–C5 ALKNs for all ATom sub-campaigns; total ALKNs for SEAC^{4}RS, KORUS-AQ, and ARCTAS; PPN and other PANs for all except ATom-1 and -2; and MPN as part of total PNs for ARCTAS, SEAC^{4}RS, and KORUS-AQ. The evaluation in Fig. 4 is biased towards the Northern Hemisphere, as the low time resolution sampling of the WAS C1–C5 ALKNs during ATom leads to loss of data in the Southern Hemisphere (Fig. 2) to achieve coincidence of DC-8 total and individual components of NO$_y$.

Total measured NO$_y$ and the sum of individual NO$_y$ components are strongly correlated ($r > 0.8$) for all campaigns except SEAC^{4}RS ($r = 0.66$). The weaker correlation for SEAC^{4}RS is due to the large contribution of MPN to total PNs measured by the TD-LIF instrument, leading to a large contribution of MPN to total NO$_y$ for many of the points that stray most from the 1 : 1 line (Fig. S2). If instead we replace TD-LIF PNs with the sum of CIMS PANs and HNO$_4$, the correlation with total measured NO$_y$ increases to $r = 0.91$, but the regression slope decreases from 0.97 in Fig. 4 to 0.82, as MPN is ∼ 20 % of SEAC^{4}RS NO$_y$. The large contribution of MPN to total NO$_y$ during SEAC^{4}RS (Fig. S2) results from aged air initially influenced by lightning, biomass burning, and deep convective uplift of surface pollution with large quantities of VOCs and NO$_x$. These large quantities of VOCs and NO$_x$ cause very active photochemistry that enhances the abundance of the MPN precursor, CH$_3$O$_2$ (Browne et al., 2011; Nault et al., 2015).

The regression slopes in Fig. 4 indicate that most NO$_y$ components are measured during each campaign, ranging from 0.78 for ATom-2 (78 % of individual NO$_y$ components measured) to 0.99 for ATom-4 (99 % measured). The slopes suggest that between 1 % and 22 % of NO$_y$ originates from factors such as unmeasured components, positive interference in the NO$_y$ instrument, or a low bias in the TD-LIF PNs. Bradshaw et al. (1998) estimated a temperature-dependent interference from HCN of 8 %–15 % for chemiluminescence instruments that, like those deployed on DC-8 campaigns, use a CO reagent. We estimate a lower-end (8 %) interference for mean ambient upper troposphere temperatures measured along the flight paths in Fig. 2. Using DC-8 HCN observations, this amounts to ∼ 53 ppt or 12 % of NO$_y$ for ARCTAS, ∼ 19 pptv or 5 % of NO$_y$ for SEAC^{4}RS, ∼ 40 pptv or 6 % of NO$_y$ for KORUS-AQ, and ∼ 17 pptv or 6 % of NO$_y$ for ATom 1-4. These lower-end interference estimates are similar in size to the percent of unaccounted NO$_y$ (13 % for ARCTAS, 3 % for SEAC^{4}RS, 8 % for KORUS-AQ, 1 %–22 % for ATom).

Chemiluminescence NO$_y$ instruments also measure pNO$_3$ but with uncertain sampling efficiencies (Bourgeois et al., 2022). For 100 % sampling efficiency, we use the aerosol mass spectrometer (AMS) measurements of submicron (< 1 µm) pNO$_3$ to estimate a pNO$_3$ contribution that is at most 1 % of NO$_y$ for ARCTAS for a median pNO$_3$ of ∼ 0.01 µg m^{-3} (∼ 4 pptv), ∼ 4 % for SEAC^{4}RS for pNO$_3$ of ∼ 0.04 µg m^{-3} (∼ 14 pptv), ∼ 4 % for KORUS-AQ for pNO$_3$ ∼ 0.07 µg m^{-3} (∼ 25 pptv), and < 2 % for ATom for pNO$_3$ < 0.01 µg m^{-3} (∼ 4 pptv).

TD-LIF measurements of PNs are calculated from the difference in NO$_2$ detected with the NO$_2$ channel and with the PNs channel set to a temperature at which all PNs decompose

Table 1. Observations of individual NO_y components summed to assess budget closure in Fig. 4.

Component	NASA DC-8 aircraft campaign		
	ARCTAS, SEAC^{4}RS, KORUS-AQ	ATom1-2	ATom3-4
NO_2	PSS	PSS	PSS
NO	Chemiluminescence (CL)	CL	CL
HNO_3	CIMS	CIMS	CIMS
HNO_4	TD-LIF PNs	CIMS	–
PAN	TD-LIF PNs	PANTHER	PANTHER
PPN	TD-LIF PNs	–	CIMS
other PANs	TD-LIF PNs	–	CIMS
ALKNs	TD-LIF ALKNs	WAS C1–C5	WAS C1–C5
MPN	TD-LIF PNs	–	–

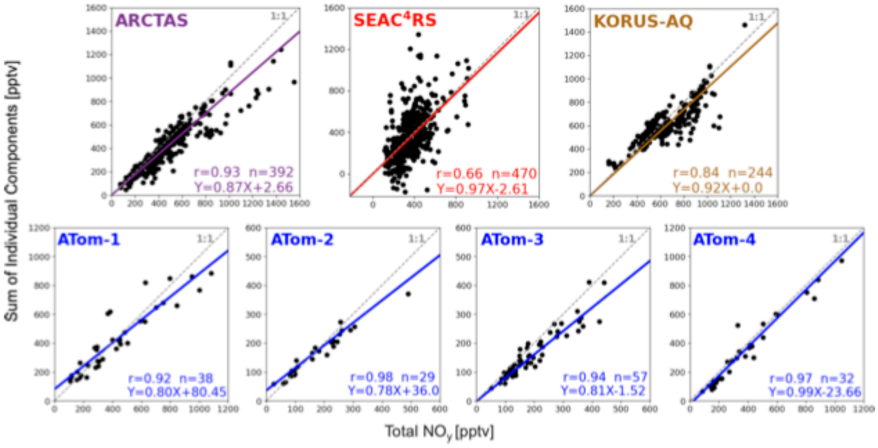

Figure 4. Proportion of reactive oxidized nitrogen components measured during each campaign. Individual points compare the coincident sum of individual NO_y components (Table 1) to measured total NO_y during NASA DC-8 campaigns. Individual NO_y components used in the figure are detailed in the text. Dashed grey lines represent the 1 : 1 relationship. Coloured lines and inset equations show the Theil–Sen regression fit to the observations. Other inset values are Pearson's correlation coefficients (r) and number of points (n). Axis ranges differ in each panel.

(Day et al., 2002). A bias in NO_2 could therefore impart a bias in PNs. The largest source of TD-LIF interference is the 100 % thermal decomposition of MPN (Reed et al., 2016b), and MPN during SEAC^{4}RS far exceeds that of any of the other campaigns. If we use the higher-end MPN interference of 21 % from Shah et al. (2023) for SEAC^{4}RS, this equates to ∼ 5 pptv of SEAC^{4}RS PSS NO_2. This is only ∼ 3 % of the 190 pptv SEAC^{4}RS PNs.

3.2 Upper tropospheric NO_y composition

Figure 5 provides a breakdown of the absolute and relative contributions of individual NO_y components to total NO_y. ATom-1 and -4 are combined, as these sub-campaigns have a very similar range in NO_y (Fig. 4) and in median total and individual components of NO_y, as the sampled seasons (spring and summer) have very similar NO_y (Fig. 3). Similarly, ATom-2 and -3 (autumn and winter) are combined. Campaigns are further grouped into remote (ARCTAS, ATom) and continental (SEAC^{4}RS, KORUS-AQ), as local influence from continental sources, like anthropogenic emissions and intense lightning, leads to a greater relative contribution of NO_x and lesser contribution of PAN for the continental upper troposphere and vice versa for the remote upper troposphere.

Inferred DC-8 HNO_4 and PPN in Fig. 5 use ATom-1 HNO_4 and ATom-4 PPN for combined ATom-1 and -4 components and, similarly, ATom-2 HNO_4 and ATom-3 PPN for combined ATom-2 and -3. KORUS-AQ HNO_4 is estimated to be 37 pptv by multiplying the SEAC^{4}RS median fraction of HNO_4 ($HNO_4/NO_y = 0.06$) by the KORUS-AQ median

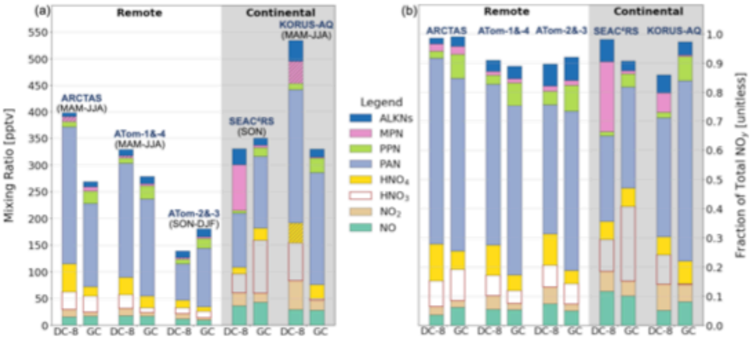

Figure 5. NO_y composition in the upper troposphere along DC-8 flight tracks. Bars represent the median values of absolute **(a)** and relative **(b)** individual NO_y components observed and inferred from observations during DC-8 campaigns and simulated by GEOS-Chem (GC). Seasons sampled are given above each bar **(a)**, and the grey shading distinguishes sampling in the remote (no shading) and continental (shaded) upper troposphere. Hatching in **(a)** indicates inferred concentrations (see text for details). Bar components from bottom to top are NO, NO_2, HNO_3, HNO_4, PAN, PPN, MPN, and ALKNs.

NO_y. SEAC^{4}RS is used because HNO_4 is thermally unstable (Ryerson et al., 2000) and so varies with temperature. Mean upper troposphere ambient temperatures for KORUS-AQ (252 K) are more consistent with SEAC^{4}RS (246 K) than the other campaigns (238 K for ARCTAS, 238–241 K for ATom).

The inferred ~ 10 pptv ARCTAS MPN is from the estimate by Browne et al. (2011). KORUS-AQ MPN is estimated by bounding a potential range from two approaches. The first is the median value of the difference between TD-LIF total PNs and the sum of all individual CIMS PANs and our inferred HNO_4 of 37 pptv, yielding MPN = 75 pptv. This likely overestimates MPN, as the CIMS instrument does not measure an exhaustive suite of PANs. Lee et al. (2022) estimated with a box model and KORUS-AQ measurements that unmeasured PANs account for ~ 20 % of total PNs during KORUS-AQ, though this applies to air masses impacted by petrochemical and other anthropogenic VOCs and NO_x emissions. Accounting for these unmeasured PANs yields a lower-bound KORUS-AQ MPN of 8 pptv. The MPN thus inferred for KORUS-AQ is 42 pptv, taken as the midpoint between 8 and 75 pptv, and it accounts for 7 % of KORUS-AQ NO_y. As the GEOS-Chem model MPN is consistent with DC-8 inferred MPN during ARCTAS, we multiply the GEOS-Chem ATom MPN fractions (MPN/NO_y ~ 0.01 for ATom-1 and -4 and ~ 0.02 for ATom-2 and -3) by ATom DC-8 NO_y to infer ATom MPN of < 6 pptv.

Only the C1–C5 ALKNs are shown in Fig. 5 for ATom. The remote measurements of total ALKNs available from ARCTAS that would be most suitable to assess the likely contribution of longer chain (> C5) ALKNs are on median 5 pptv less than the ATom C1–C5 ALKNs measurements. The ARCTAS total ALKNs measurements are also very noisy, as indicated by a range of −113 pptv to ~ 333 pptv. The range in ARCTAS WAS C1–C5 measurements, by comparison, is 8–29 pptv. Contributions of > C5 ALKNs to total ALKNs for SEAC^{4}RS (~ 50 %) and KORUS-AQ (~ 60 %), representative of the continental upper troposphere, suggest that > C5 ALKNs in remote regions are < 50 % of total ALKNs or < 12 pptv (median of C1–C5 ALKNs for ATom1-4). According to the measurements, remote region C1–C5 ALKNs are dominated by methyl nitrate (C1 ALKN), accounting for 40 % of ATom C1–C5 ALKNs and 49 % for ARCTAS. Second is isopropyl nitrate (C3 ALKN), making up 17 % of ATom C1–C5 ALKNs and 25 % for ARCTAS. The > C3 ALKNs dominate ALKNs in the continental upper troposphere, accounting for 92 % of total ALKNs for SEAC^{4}RS and 71 % for KORUS-AQ. We estimate these as the difference between TD-LIF total ALKNs and the sum of WAS C1-C3 ALKNs.

The sum of KORUS-AQ NO_y components totals 531 pptv, > 130 pptv higher than SEAC^{4}RS, ARCTAS, and ATom-1 and -4, all of which are within a narrow range of 330–400 pptv. Minimum NO_y values are for the remote autumn and winter measurements from ATom-2 and -3 at 141 pptv. Despite the wide range in absolute total and components of NO_y, the relative contribution of many individual NO_y components is consistent across all campaigns. These include NO (7 ± 3 %; mean $\pm 1\sigma$ standard deviation), NO_2 (6 ± 2 %), HNO_3 (9 ± 2 %), HNO_4 (9 ± 3 %), PPN (3 ± 1 %), and ALKNs (5 ± 3 %). PAN, the dominant NO_y component in all campaigns, is least consistent, ranging from 30 %–41 % for the continental upper troposphere to 44 %–64 % for the remote upper troposphere. The HNO_4 fraction (10 %–13 %) in the remote upper troposphere is higher than in the continental upper troposphere (~ 6 %), due to colder temperatures for ATom and ARCTAS. MPN is uniquely prominent during SEAC^{4}RS, accounting for 24 %

of NO_y compared to 2 %–7 % inferred for all other campaigns. pNO_3, absent in Fig. 5 due to the uncertain sampling efficiency of the chemiluminescence instrument, is at most 4 % for SEAC^{4}RS and KORUS-AQ (Sect. 3.1), comparable to the contribution from PPN.

The far larger fraction of MPN to total NO_y during SEAC^{4}RS (Fig. 5b) warrants further investigation, as the relative proportion of MPN to total NO_y ranges from negligible to 100 % (Fig. S2). If we instead estimate MPN by subtracting the sum of HNO_4 and all PANs measured with the CIMS instrument from the TD-LIF PNs, making the assumption that CIMS measures most PANs, MPN is 49 pptv and the SEAC^{4}RS median contribution to NO_y declines from 24 % to 14 %. This is still at least double the contribution for any other campaign. A small proportion of HNO_4 is measured in the MPN channel of the TD-LIF instrument. This represents about 11 %, according to Nault et al. (2015). For the CIMS median HNO_4 of 12.6 pptv during SEAC^{4}RS, the HNO_4 interference is only 1.4 pptv, so it does not affect the 14 %–24 % contribution.

The NO_y composition information in Fig. 5 has a Northern Hemisphere sampling bias to achieve coincidence. ATom observations south of the Equator exhibit a similar seasonal pattern to the Northern Hemisphere: summer > spring > autumn > winter NO_y, except that the Southern Hemisphere spring and summer NO_y differ by ~ 90 pptv, whereas there is a near-negligible difference for the Northern Hemisphere (Fig. 3). As with the Northern Hemisphere, PAN accounts for most Southern Hemisphere NO_y, ranging from ~ 32 % for ATom-1 (July–August) to ~ 42 % for ATom-2 (January–February).

Nighttime-dominant NO_y compounds N_2O_5, NO_3, and HONO are not included in Fig. 5, as these have near-negligible daytime abundances. Of these, there are only measurements of N_2O_5, limited to ATom-3 and -4, that represent ~ 0.1 % of upper tropospheric NO_y along the daytime ATom flight tracks in Fig. 2. NO_3 has a lifetime of a few seconds during the day, due to efficient photolysis (Brown and Stutz, 2012). HONO also rapidly photolyses with a near-surface lifetime of 15 min (Sörgel et al., 2011). Photolysis of HONO would be further enhanced (by ~ 50 % at 390 nm) in the upper troposphere where photolysis frequencies are enhanced (Hofzumahaus et al., 2002; Reed et al., 2016a).

3.3 Contemporary understanding of UT NO_y

GEOS-Chem Northern Hemisphere upper troposphere NO_y is compared to the observations in Figs. 3 and 5. In Fig. 3, the GEOS-Chem median NO_y is less than that of DC-8 in summer and spring by ~ 103 pptv, similar to that of DC-8 in autumn and greater than that of DC-8 in winter by ~ 60 pptv. As a result of these differences in absolute NO_y, the model underestimates the IAGOS and DC-8 seasonal shifts in NO_y from winter to spring and from summer to autumn.

The sum of the GEOS-Chem fractional contributions of NO_y components in Fig. 5b does not equal 1 because the model NO_y budget also includes components not measured during DC-8 campaigns, such as MPAN and halogenated ALKNs. Consistent across all campaigns is a model underestimate of NO_2 and an overestimate of PPN. The model version we use does not include photolysis of PPN, even though this is known to occur (Harwood et al., 2003). PPN photolysis rather than thermal decomposition is the dominant loss pathway of PPN in the cold upper troposphere. PPN photolysis is scheduled for inclusion in a later model version (version 14.5) than that used here (Horner et al., 2024). Inclusion of PPN photolysis would liberate up to ~ 16 pptv NO_2, resolving the 10–16 pptv model underestimate in NO_2. Other studies have addressed model biases in NO_2 by including photolysis of pNO_3 forming HONO that rapidly photolyses to NO_x (Shah et al., 2023; Horner et al., 2024). pNO_3 concentrations are too small in the upper troposphere for this to be a substantial NO_2 source. These are, on median, ~ 0.01 $\mu g\,m^{-3}$ during ARCTAS, ~ 0.07 $\mu g\,m^{-3}$ during KORUS-AQ, ~ 0.04 $\mu g\,m^{-3}$ during SEAC^{4}RS, and < 0.01 $\mu g\,m^{-3}$ during ATom (Sect. 3.1).

The model exhibits significant campaign-specific biases in total NO_y for ARCTAS (129 pptv underestimate), KORUS-AQ (205 pptv underestimate), ATom-1 and -4 (51 pptv underestimate), and ATom-2 and -3 (42 pptv overestimate). The model underestimate in ARCTAS NO_y is due mostly to a ~ 100 pptv low bias in PAN and, to a lesser extent, a 35 pptv underestimate in HNO_4. The model bias for ATom-2 and -3 is due almost entirely to PAN. For KORUS-AQ, all NO_y components except PPN are underestimated, indicative of an overall underestimate in NO_y sources to the upper troposphere over this region. The ATom-1 and -4 underestimation in NO_y is primarily due to a low model bias in PAN and HNO_3. Overall, the model underestimates the contrast in upper tropospheric NO_y between the remote and continental upper troposphere.

GEOS-Chem simulates individual C1-C3 ALKNs, but most > C3 ALKNs are included as a lumped species. There are other > C3 ALKNs represented individually in the model, such as those formed from isoprene oxidation (Fisher et al., 2016), but abundances of these are near negligible in the upper troposphere. DC-8 C1 ALKN is only 4 % of ALKNs for SEAC^{4}RS and 11 % for KORUS-AQ, whereas in the model these are a much greater component of ALKNs: 40 % for SEAC^{4}RS and 29 % for KORUS-AQ. Modelled > C3 ALKNs are a far smaller portion of total ALKNs (29 % for SEAC^{4}RS and 23 % for KORUS-AQ) than the observations (Sect. 3.2). Modelled C1 ALKN concentrations are consistently less than the observed values by ~ 2 pptv for ARCTAS and ~ 1 pptv for ATom. Modelled C3 ALKN is ~ 1 pptv lower than the observations for ARCTAS but ~ 1 pptv higher than the observations for ATom.

The sum of measured and modelled individual NO_y components is not significantly different for SEAC^{4}RS, though the model overestimates HNO_3 by 64 pptv and underestimates MPN by 81 pptv compared to the TD-LIF measurements and by 45 pptv compared to MPN inferred using TD-LIF PNs and CIMS measurements of HNO_4 and PANs (Sect. 3.2). The low bias in the model in MPN suggests that the model underestimates the influence of NO_x and reactive VOC sources on aged air over source regions with a mix of emissions from fires and lightning and deep convective injection of surface pollution. Chen et al. (2019) estimated that the GEOS-Chem underestimate in free-tropospheric VOCs during SEAC^{4}RS is on average $\sim 60\,\%$ but exceeds a factor of 2 for many of the VOCs assessed. The high bias in modelled HNO_3 during SEAC^{4}RS (Fig. 5) could be because of a factor of 2 overestimate in modelled H_2O_2 compared to observed H_2O_2 for SEAC^{4}RS. An overestimate in H_2O_2 indicates a model overestimate in HO_2 that promotes formation of HNO_3 and that would also account for the ~ 10 pptv overestimate in modelled HNO_4. Modelled HO_2 is used to calculate PSS NO_2 for SEAC^{4}RS (Eq. (1), Sect. 2.1), but this only imparts a small high bias (~ 1.7 pptv) in SEAC^{4}RS PSS NO_2. Model bias in H_2O_2 for ARCTAS (> 100 pptv) may also be responsible for the model underestimate in ARCTAS HNO_4 of ~ 35 pptv.

Modelled KORUS-AQ HNO_3, ALKNs, and MPN are all biased low. The low biases in these NO_y components may be because of a general underestimate in NO_y sources over South Korea where there are large anthropogenic NO_x and VOC sources that are represented in the model with a global inventory (CEDS) that may not suitably account for local emissions (Travis et al., 2024). Lightning NO_x emissions could also be underestimated in the heavily parameterized inventory in GEOS-Chem (Murray et al., 2012; Marais et al., 2018), but this is a challenging NO_x source to evaluate over locations that include other prominent sources of NO_x.

The model biases identified in this work hinder the accurate determination of the radiative effect of tropospheric ozone for short-term climate impact assessments, the oxidative capacity of the troposphere in quantifying the lifetime and persistence of the greenhouse gas methane, tropospheric column densities of NO_2 from space-based UV-visible instruments that are retrieved with modelled vertical profiles of NO_2, NO_x emissions by means of comparing modelled and observed oxidized nitrate wet deposition fluxes that depend on the abundance of soluble HNO_3, and harm from nitrogen deposition to vulnerable habitats.

4 Conclusions

We used NASA DC-8 aircraft measurement data from the ARCTAS, SEAC^{4}RS, KORUS-AQ, and ATom campaigns to characterize reactive oxidized nitrogen (NO_y) in the global upper troposphere. This followed confirmation from comparison to routine total NO_y measurements from the IAGOS commercial aircraft campaign that DC-8 has the same seasonality as peak NO_y in summer and spring and minimum NO_y in winter in the Northern Hemisphere. Consistency supports the use of DC-8 campaign data to characterize NO_y under standard daytime conditions.

We also confirm that most (78 %–99 %) NO_y components were measured during DC-8 campaigns. These include nitrogen oxides (NO_x) and inorganic (HNO_3 and HNO_4) and organic (PANs, MPN, and alkyl nitrates) reservoirs of NO_x. PAN is the dominant NO_y component for all campaigns (30 %–64 %), followed by NO_x (6 %–18 %), HNO_4 (6 %–13 %), and HNO_3 (7 %–11 %). The relative contribution of most other components is similar across all campaigns, except for MPN. MPN is 14 %–24 % of NO_y for SEAC^{4}RS over the Southeast US and much less (2 %–7 %) for all other campaigns, though MPN measurements are rare and susceptible to biases.

The GEOS-Chem model is sampled along the DC-8 flight tracks to assess the state of knowledge of upper tropospheric NO_y. Consistent model biases for all campaigns include an overestimate in PPN and underestimate in NO_2. The model lacks PPN photolysis that would address the PPN model bias and mostly resolve the NO_2 bias. In the continental upper troposphere, the model underestimates total NO_y for KORUS-AQ but reproduces total NO_y for SEAC^{4}RS, though with too much HNO_3 and too little MPN. Over remote regions, the model biases are less severe and are likely related to the weak seasonal variability in total NO_y in comparison to DC-8 and IAGOS. A possible cause of this is errors in model representation of maritime lightning NO_x emissions that influence NO_y abundance in spring and summer.

Our results underscore the need for sustained measurements of upper tropospheric reactive oxidized nitrogen for further refinement of knowledge of upper tropospheric NO_y sources, advection, and chemical processing. This is crucial for advancing our understanding of the global nitrogen cycle and its broader environmental impacts.

Code and data availability. All data and software used in this study are from publicly accessible repositories: Zenodo for GEOS-Chem (https://doi.org/10.5281/zenodo.4681204, The International GEOS-Chem User Community, 2021), the AERIS data service for IAGOS (Boulanger et al., 2018), and NASA data archives for ARCTAS (https://www-air.larc.nasa.gov/cgi-bin/ArcView/arctas?DC8=1, NASA, 2009), SEAC^{4}RS (https://www-air.larc.nasa.gov/cgi-bin/ArcView/seac4rs, NASA, 2015), KORUS-AQ (https://asdc.larc.nasa.gov/project/KORUS-AQ, NASA, 2017), and ATom (https://daac.ornl.gov/cgi-bin/dsviewer.pl?ds_id=1925, NASA, 2021).

Author contributions. The study concept was developed by EAM and NW. NW led the data analysis and simulated GEOS-Chem. The manuscript was initiated by NW and co-written by EAM. GL aided in data analysis, RGR in the use of ObsPack, and BS in the use of IAGOS NO_y observations. All authors reviewed and edited the manuscript.

Competing interests. The contact author has declared that none of the authors has any competing interests.

Acknowledgements. We are grateful for the provision of the NASA DC-8 aircraft observations by the instrument PIs Paul O. Wennberg, Ronald C. Cohen, Thomas B. Ryerson, Chelsea Thompson, Andrew Weinheimer, L. Gregory Huey, Jim Elkins, and Donald R. Blake, as well as for the IAGOS-Core data provided by Andreas Volz-Thomas and IAGOS-CARIBIC data by Helmut Ziereis. The authors acknowledge the strong support of the European Commission, Airbus, and the airlines (Lufthansa, Air France, Austrian Airlines, Air Namibia, Cathay Pacific, Iberia, and China Airlines to date) for carrying the IAGOS-Core equipment and performing its maintenance since 1994. IAGOS-CARIBIC NO_y measurement funding was provided by the German Aerospace Centre (DLR). In its last 10 years of operation, IAGOS-Core has been funded by INSU–CNRS (France), Météo-France, Université Paul Sabatier (Toulouse, France), and Forschungszentrum Jülich (FZJ, Jülich, Germany). IAGOS has been additionally funded by the EU projects IAGOSDS and IAGOS-ERI. The IAGOS-Core and the IAGOS-CARIBIC databases are supported by AERIS. IAGOS-CARIBIC data are also available from the IAGOS-CARIBIC team (see http://www.caribic-atmospheric.com, last access: 23 May 2023).

Financial support. This research has been supported by the European Research Council under the European Union's Horizon 2020 research and innovation programme, through a Starting Grant awarded to Eloise A. Marais, UpTrop (grant no. 851854).

Review statement. This paper was edited by Benjamin A. Nault and reviewed by two anonymous referees.

References

Amos, H. M., Jacob, D. J., Holmes, C. D., Fisher, J. A., Wang, Q., Yantosca, R. M., Corbitt, E. S., Galarneau, E., Rutter, A. P., Gustin, M. S., Steffen, A., Schauer, J. J., Graydon, J. A., Louis, V. L. St., Talbot, R. W., Edgerton, E. S., Zhang, Y., and Sunderland, E. M.: Gas-particle partitioning of atmospheric Hg(II) and its effect on global mercury deposition, Atmos. Chem. Phys., 12, 591–603, https://doi.org/10.5194/acp-12-591-2012, 2012.

Barth, M. C., Cantrell, C. A., Brune, W. H., Rutledge, S. A., Crawford, J. H., Huntrieser, H., Carey, L. D., MacGorman, D., Weisman, M., Pickering, K. E., Bruning, E., Anderson, B., Apel, E., Biggerstaff, M., Campos, T., Campuzano-Jost, P., Cohen, R., Crounse, J., Day, D. A., Diskin, G., Flocke, F., Fried, A., Garland, C., Heikes, B., Honomichl, S., Hornbrook, R., Huey, L. G., Jimenez, J. L., Lang, T., Lichtenstern, M., Mikoviny, T., Nault, B., O'Sullivan, D., Pan, L. L., Peischl, J., Pollack, I., Richter, D., Riemer, D., Ryerson, T., Schlager, H., St. Clair, J., Walega, J., Weibring, P., Weinheimer, A., Wennberg, P., Wisthaler, A., Wooldridge, P. J., and Ziegler, C.: The Deep Convective Clouds and Chemistry (DC3) Field Campaign, B. Am. Meteorol. Soc., 96, 1281–1309, https://doi.org/10.1175/bams-d-13-00290.1, 2015.

Bertram, T. H., Perring, A. E., Wooldridge, P. J., Crounse, J. D., Kwan, A. J., Wennberg, P. O., Scheuer, E., Dibb, J., Avery, M., Sachse, G., Vay, S. A., Crawford, J. H., McNaughton, C. S., Clarke, A., Pickering, K. E., Fuelberg, H., Huey, G., Blake, D. R., Singh, H. B., Hall, S. R., Shetter, R. E., Fried, A., Heikes, B. G., and Cohen, R. C.: Direct measurements of the convective recycling of the upper troposphere, Science, 315, 816–820, https://doi.org/10.1126/science.1134548, 2007.

Blake, N. J., Blake, D. R., Swanson, A. L., Atlas, E., Flocke, F., and Rowland, F. S.: Latitudinal, vertical, and seasonal variations of C1-C4 alkyl nitrates in the troposphere over the Pacific Ocean during PEM-Tropics A and B: Oceanic and continental sources, J. Geophys. Res.-Atmos., 108, 8242, https://doi.org/10.1029/2001JD001444, 2003.

Blakeslee, R. J., Mach, D. M., Bateman, M. G., and Bailey, J. C.: Seasonal variations in the lightning diurnal cycle and implications for the global electric circuit, Atmos. Res., 135–136, 228–243, https://doi.org/10.1016/j.atmosres.2012.09.023, 2014.

Boersma, K. F., Eskes, H. J., Dirksen, R. J., van der A, R. J., Veefkind, J. P., Stammes, P., Huijnen, V., Kleipool, Q. L., Sneep, M., Claas, J., Leitão, J., Richter, A., Zhou, Y., and Brunner, D.: An improved tropospheric NO_2 column retrieval algorithm for the Ozone Monitoring Instrument, Atmos. Meas. Tech., 4, 1905–1928, https://doi.org/10.5194/amt-4-1905-2011, 2011.

Boulanger, D., Blot, R., Bundke, U., Gerbig, C., Hermann, M., Nédélec, P., Rohs, S., and Ziereis, H., IAGOS final quality controlled Observational Data L2 – Vertical profiles, AERIS [data set], https://doi.org/10.25326/07, 2018.

Bourgeois, I., Peischl, J., Neuman, J. A., Brown, S. S., Allen, H. M., Campuzano-Jost, P., Coggon, M. M., DiGangi, J. P., Diskin, G. S., Gilman, J. B., Gkatzelis, G. I., Guo, H., Halliday, H. A., Hanisco, T. F., Holmes, C. D., Huey, L. G., Jimenez, J. L., Lamplugh, A. D., Lee, Y. R., Lindaas, J., Moore, R. H., Nault, B. A., Nowak, J. B., Pagonis, D., Rickly, P. S., Robinson, M. A., Rollins, A. W., Selimovic, V., St. Clair, J. M., Tanner, D., Vasquez, K. T., Veres, P. R., Warneke, C., Wennberg, P. O., Washenfelder, R. A., Wiggins, E. B., Womack, C. C., Xu, L., Zarzana, K. J., and Ryerson, T. B.: Comparison of airborne measurements of NO, NO_2, HONO, NO_y, and CO during FIREX-AQ, Atmos. Meas. Tech., 15, 4901–4930, https://doi.org/10.5194/amt-15-4901-2022, 2022.

Bradshaw, J., Sandholm, S., and Talbot, R.: An update on reactive odd-nitrogen measurements made during recent NASA Global Tropospheric Experiment programs, J. Geophys. Res.-Atmos., 103, 19129–19148, https://doi.org/10.1029/98JD00621, 1998.

Bradshaw, J., Davis, D., Grodzinsky, G., Smyth, S., Newell, R., Sandholm, S., and Liu, S.: Observed distributions of nitrogen oxides in the remote free troposphere from the NASA Global Tropospheric Experiment Programs, Rev. Geophys., 38, 61–116, https://doi.org/10.1029/1999rg900015, 2000.

Brasseur, G. P., Müller, J.-F., and Granier, C.: Atmospheric impact of NO_x emissions by subsonic aircraft: A three dimensional model study, J. Geophys. Res.-Atmos., 101, 1423–1428, https://doi.org/10.1029/95jd02363, 1996.

Brenninkmeijer, C. A. M., Crutzen, P., Boumard, F., Dauer, T., Dix, B., Ebinghaus, R., Filippi, D., Fischer, H., Franke, H., Frieβ, U., Heintzenberg, J., Helleis, F., Hermann, M., Kock, H. H., Koeppel, C., Lelieveld, J., Leuenberger, M., Martinsson, B. G., Miemczyk, S., Moret, H. P., Nguyen, H. N., Nyfeler, P., Oram, D., O'Sullivan, D., Penkett, S., Platt, U., Pupek, M., Ramonet, M., Randa, B., Reichelt, M., Rhee, T. S., Rohwer, J., Rosenfeld, K., Scharffe, D., Schlager, H., Schumann, U., Slemr, F., Sprung, D., Stock, P., Thaler, R., Valentino, F., van Velthoven, P., Waibel, A., Wandel, A., Waschitschek, K., Wiedensohler, A., Xueref-Remy, I., Zahn, A., Zech, U., and Ziereis, H.: Civil Aircraft for the regular investigation of the atmosphere based on an instrumented container: The new CARIBIC system, Atmos. Chem. Phys., 7, 4953–4976, https://doi.org/10.5194/acp-7-4953-2007, 2007.

Brown, S. S. and Stutz, J.: Nighttime radical observations and chemistry, Chem. Soc. Rev., 41, 6405–6447, https://doi.org/10.1039/C2CS35181A, 2012.

Browne, E. C., Perring, A. E., Wooldridge, P. J., Apel, E., Hall, S. R., Huey, L. G., Mao, J., Spencer, K. M., Clair, J. M. St., Weinheimer, A. J., Wisthaler, A., and Cohen, R. C.: Global and regional effects of the photochemistry of CH3O2NO2: evidence from ARCTAS, Atmos. Chem. Phys., 11, 4209–4219, https://doi.org/10.5194/acp-11-4209-2011, 2011.

Burkholder, J. B., Sander, S. P., Abbatt, J., Barker, J. R., Cappa, C., Crounse, J. D., Dibble, T. S., Huie, R. E., Kolb, C. E., Kurylo, M. J., Orkin, V. L., Percival, C. J., Wilmouth, D. M., and Wine, P. H.: Chemical kinetics and photochemical data for use in atmospheric studies, evaluation No. 19, JPL Publication 19-5, https://jpldataeval.jpl.nasa.gov/pdf/NASA-JPL%20Evaluation%2019-5.pdf (last access: 20 May 2024), 2020.

Chen, X., Millet, D. B., Singh, H. B., Wisthaler, A., Apel, E. C., Atlas, E. L., Blake, D. R., Bourgeois, I., Brown, S. S., Crounse, J. D., de Gouw, J. A., Flocke, F. M., Fried, A., Heikes, B. G., Hornbrook, R. S., Mikoviny, T., Min, K.-E., Müller, M., Neuman, J. A., O'Sullivan, D. W., Peischl, J., Pfister, G. G., Richter, D., Roberts, J. M., Ryerson, T. B., Shertz, S. R., Thompson, C. R., Treadaway, V., Veres, P. R., Walega, J., Warneke, C., Washenfelder, R. A., Weibring, P., and Yuan, B.: On the sources and sinks of atmospheric VOCs: an integrated analysis of recent aircraft campaigns over North America, Atmos. Chem. Phys., 19, 9097–9123, https://doi.org/10.5194/acp-19-9097-2019, 2019.

Cohen, Y., Hauglustaine, D., Sauvage, B., Rohs, S., Konjari, P., Bundke, U., Petzold, A., Thouret, V., Zahn, A., and Ziereis, H.: Evaluation of modelled climatologies of O_3, CO, water vapour and NOy in the upper troposphere–lower stratosphere using regular in situ observations by passenger aircraft, Atmos. Chem. Phys., 23, 14973–15009, https://doi.org/10.5194/acp-23-14973-2023, 2023.

Crawford, J. H., Ahn, J.-Y., Al-Saadi, J., Chang, L., Emmons, L. K., Kim, J., Lee, G., Park, J.-H., Park, R. J., Woo, J. H., Song, C.-K., Hong, J.-H., Hong, Y.-D., Lefer, B. L., Lee, M., Lee, T., Kim, S., Min, K.-E., Yum, S. S., Shin, H. J., Kim, Y.-W., Choi, J.-S., Park, J.-S., Szykman, J. J., Long, R. W., Jordan, C. E., Simpson, I. J., Fried, A., Dibb, J. E., Cho, S., and Kim, Y. P.: The Korea–United States Air Quality (KORUS-AQ) field study, Elementa, 9, 00163, https://doi.org/10.1525/elementa.2020.00163, 2021.

Crounse, J. D., McKinney, K. A., Kwan, A. J., and Wennberg, P. O.: Measurement of gas-phase yydroperoxides by Chemical Ionization Mass Spectrometry, Anal. Chem., 78, 6726–6732, https://doi.org/10.1021/ac0604235, 2006.

Culter, F.: NASA DC-8 Flying Laboratory Aircraft, https://ghrc.nsstc.nasa.gov/home/sites/default/files/cutler_dc8.pdf, (last access: 3 October 2024), 2009.

Dahlmann, K., Grewe, V., Ponater, M., and Matthes, S.: Quantifying the contributions of individual NO_x sources to the trend in ozone radiative forcing, Atmos. Environ., 45, 2860–2868, https://doi.org/10.1016/j.atmosenv.2011.02.071, 2011.

Dameris, M.: Stratosphere/Troposphere exchange and structure | Tropopause, in: Encyclopedia of Atmospheric Sciences, 2nd Edn., edited by: North, G. R., Pyle, J., and Zhang, F., Academic Press, Oxford, 269–272, https://doi.org/10.1016/B978-0-12-382225-3.00418-7, 2015.

Day, D. A., Wooldridge, P. J., Dillon, M. B., Thornton, J. A., and Cohen, R. C.: A thermal dissociation laser-induced fluorescence instrument for in situ detection of NO_2, peroxy nitrates, alkyl nitrates, and HNO_3, J. Geophys. Res.-Atmos., 107, 4046, https://doi.org/10.1029/2001jd000779, 2002.

Ehhalt, D. H., Rohrer, F., and Wahner, A.: Sources and distribution of NO_x in the upper troposphere at northern mid-latitudes, J. Geophys. Res.-Atmos., 97, 3725–3738, https://doi.org/10.1029/91JD03081, 1992.

Emmons, L. K., Carroll, M. A., Hauglustaine, D. A., Brasseur, G. P., Atherton, C., Penner, J., Sillman, S., Levy, H., Rohrer, F., Wauben, W. M. F., Van Velthoven, P. F. J., Wang, Y., Jacob, D., Bakwin, P., Dickerson, R., Doddridge, B., Gerbig, C., Honrath, R., Hübler, G., Jaffe, D., Kondo, Y., Munger, J. W., Torres, A., and Volz-Thomas, A.: Climatologies of NO_x and NO_y: A comparison of data and models, Atmos. Environ., 31, 1851–1904, https://doi.org/10.1016/s1352-2310(96)00334-2, 1997.

Fisher, J. A., Jacob, D. J., Travis, K. R., Kim, P. S., Marais, E. A., Chan Miller, C., Yu, K., Zhu, L., Yantosca, R. M., Sulprizio, M. P., Mao, J., Wennberg, P. O., Crounse, J. D., Teng, A. P., Nguyen, T. B., St. Clair, J. M., Cohen, R. C., Romer, P., Nault, B. A., Wooldridge, P. J., Jimenez, J. L., Campuzano-Jost, P., Day, D. A., Hu, W., Shepson, P. B., Xiong, F., Blake, D. R., Goldstein, A. H., Misztal, P. K., Hanisco, T. F., Wolfe, G. M., Ryerson, T. B., Wisthaler, A., and Mikoviny, T.: Organic nitrate chemistry and its implications for nitrogen budgets in an isoprene- and monoterpene-rich atmosphere: constraints from aircraft (SEAC4RS) and ground-based (SOAS) observations in the Southeast US, Atmos. Chem. Phys., 16, 5969–5991, https://doi.org/10.5194/acp-16-5969-2016, 2016.

Fisher, J. A., Atlas, E. L., [illegible] https://doi.org/10.5194/acp-16-5969-2016 Thompson, C. R., Ryerson, T. B., Peischl, J., Tzompa-Sosa, Z. A., and Murray, L. T.: Methyl, ethyl, and propyl nitrates: Global distribution and impacts on reactive nitrogen in remote marine environments, J. Geophys. Res.-Atmos., 123, 12429–12451, https://doi.org/10.1029/2018jd029046, 2018.

Fuelberg, H. E., Hannan, J. R., van Velthoven, P. F. J., Browell, E. V., Bieberbach Jr., G., Knabb, R. D., Gregory, G. L., Pickering, K. E., and Selkirk, H. B.: A meteorological overview of the Subsonic Assessment Ozone and Nitrogen Oxide Experiment (SONEX) period, J. Geophys. Res.-Atmos., 105, 3633–3651, https://doi.org/10.1029/1999JD900917, 2000.

Giglio, L., Randerson, J. T., and van der Werf, G. R.: Analysis of daily, monthly, and annual burned area using the fourth-generation global fire emissions database (GFED4), J. Geophys. Res.-Biogeo., 118, 317–328, https://doi.org/10.1002/jgrg.20042, 2013.

Gressent, A., Sauvage, B., Defer, E., Pätz, H. W., Thomas, K., Holle, R., Cammas, J.-P., Nédélec, P., Boulanger, D., Thouret, V., and Volz-Thomas, A.: Lightning NO_x influence on large-scale NO_y and O_3 plumes observed over the northern mid-latitudes, Tellus B, 66, 25544, https://doi.org/10.3402/tellusb.v66.25544, 2014.

Gressent, A., Sauvage, B., Cariolle, D., Evans, M., Leriche, M., Mari, C., and Thouret, V.: Modeling lightning-NO_x chemistry on a sub-grid scale in a global chemical transport model, Atmos. Chem. Phys., 16, 5867–5889, https://doi.org/10.5194/acp-16-5867-2016, 2016.

Guenther, A. B., Jiang, X., Heald, C. L., Sakulyanontvittaya, T., Duhl, T., Emmons, L. K., and Wang, X.: The Model of Emissions of Gases and Aerosols from Nature version 2.1 (MEGAN2.1): an extended and updated framework for modeling biogenic emissions, Geosci. Model Dev., 5, 1471–1492, https://doi.org/10.5194/gmd-5-1471-2012, 2012.

Harwood, M. H., Roberts, J. M., Frost, G. J., Ravishankara, A. R., and Burkholder, J. B.: Photochemical Studies of $CH_3C(O)OONO_2$ (PAN) and $CH_3CH_2C(O)OONO_2$ (PPN): NO_3 Quantum Yields, J. Phys. Chem. A, 107, 1148–1154, https://doi.org/10.1021/jp0264230, 2003.

Hoesly, R. M., Smith, S. J., Feng, L., Klimont, Z., Janssens-Maenhout, G., Pitkanen, T., Seibert, J. J., Vu, L., Andres, R. J., Bolt, R. M., Bond, T. C., Dawidowski, L., Kholod, N., Kurokawa, J. I., Li, M., Liu, L., Lu, Z., Moura, M. C. P., O'Rourke, P. R., and Zhang, Q.: Historical (1750–2014) anthropogenic emissions of reactive gases and aerosols from the Community Emissions Data System (CEDS), Geosci. Model Dev., 11, 369–408, https://doi.org/10.5194/gmd-11-369-2018, 2018.

Hofzumahaus, A., Kraus, A., Kylling, A., and Zerefos, C. S.: Solar actinic radiation (280–420 nm) in the cloud–free troposphere between ground and 12 km altitude: Measurements and model results, J. Geophys. Res.-Atmos., 107, 8139, https://doi.org/10.1029/2001jd900142, 2002.

Horner, R. P., Marais, E. A., Wei, N., Ryan, R. G., and Shah, V.: Vertical profiles of global tropospheric nitrogen dioxide (NO_2) obtained by cloud slicing the TROPOspheric Monitoring Instrument (TROPOMI), Atmos. Chem. Phys., 24, 13047–13064, https://doi.org/10.5194/acp-24-13047-2024, 2024.

Hudman, R. C., Jacob, D. J., Turquety, S., Leibensperger, E. M., Murray, L. T., Wu, S., Gilliland, A. B., Avery, M., Bertram, T. H., Brune, W., Cohen, R. C., Dibb, J. E., Flocke, F. M., Fried, A., Holloway, J., Neuman, J. A., Orville, R., Perring, A., Ren, X., Sachse, G. W., Singh, H. B., Swanson, A., and Wooldridge, P. J.: Surface and lightning sources of nitrogen oxides over the United States: Magnitudes, chemical evolution, and outflow, J. Geophys. Res., 112, D12S05, https://doi.org/10.1029/2006jd007912, 2007.

Hudman, R. C., Moore, N. E., Mebust, A. K., Martin, R. V., Russell, A. R., Valin, L. C., and Cohen, R. C.: Steps towards a mechanistic model of global soil nitric oxide emissions: implementation and space based-constraints, Atmos. Chem. Phys., 12, 7779–7795, https://doi.org/10.5194/acp-12-7779-2012, 2012.

Huey, L. G.: Measurement of trace atmospheric species by chemical ionization mass spectrometry: Speciation of reactive nitrogen and future directions, Mass Spectrom. Rev., 26, 166–184, https://doi.org/10.1002/mas.20118, 2007.

Huntrieser, H., Lichtenstern, M., Scheibe, M., Aufmhoff, H., Schlager, H., Pucik, T., Minikin, A., Weinzierl, B., Heimerl, K., Pollack, I. B., Peischl, J., Ryerson, T. B., Weinheimer, A. J., Honomichl, S., Ridley, B. A., Biggerstaff, M. I., Betten, D. P., Hair, J. W., Butler, C. F., Schwartz, M. J., and Barth, M. C.: Injection of lightning-produced NO_x, water vapor, wildfire emissions, and stratospheric air to the UT/LS as observed from DC3 measurements, J. Geophys. Res.-Atmos., 121, 6638–6668, https://doi.org/10.1002/2015JD024273, 2016.

Jacob, D. J., Crawford, J. H., Maring, H., Clarke, A. D., Dibb, J. E., Emmons, L. K., Ferrare, R. A., Hostetler, C. A., Russell, P. B., Singh, H. B., Thompson, A. M., Shaw, G. E., McCauley, E., Pederson, J. R., and Fisher, J. A.: The Arctic Research of the Composition of the Troposphere from Aircraft and Satellites (ARCTAS) mission: design, execution, and first results, Atmos. Chem. Phys., 10, 5191–5212, https://doi.org/10.5194/acp-10-5191-2010, 2010.

Jaeglé, L., Jacob, D. J., Wang, Y., Weinheimer, A. J., Ridley, B. A., Campos, T. L., Sachse, G. W., and Hagen, D. E.: Sources and chemistry of NO_x in the upper troposphere over the United States, Geophys. Res. Lett., 25, 1705–1708, https://doi.org/10.1029/97gl03591, 1998.

Le Breton, M., Bacak, A., Muller, J. B. A., O'Shea, S. J., Xiao, P., Ashfold, M. N. R., Cooke, M. C., Batt, R., Shallcross, D. E., Oram, D. E., Forster, G., Bauguitte, S. J.-B., Palmer, P. I., Parrington, M., Lewis, A. C., Lee, J. D., and Percival, C. J.: Airborne hydrogen cyanide measurements using a chemical ionisation mass spectrometer for the plume identification of biomass burning forest fires, Atmos. Chem. Phys., 13, 9217–9232, https://doi.org/10.5194/acp-13-9217-2013, 2013.

Lee, Y. R., Huey, L. G., Tanner, D. J., Takeuchi, M., Qu, H., Liu, X., Ng, N. L., Crawford, J. H., Fried, A., Richter, D., Simpson, I. J., Blake, D. R., Blake, N. J., Meinardi, S., Kim, S., Diskin, G. S., Digangi, J. P., Choi, Y., Pusede, S. E., Wennberg, P. O., Kim, M. J., Crounse, J. D., Teng, A. P., Cohen, R. C., Romer, P. S., Brune, W., Wisthaler, A., Mikoviny, T., Jimenez, J. L., Campuzano-Jost, P., Nault, B. A., Weinheimer, A., Hall, S. R., and Ullmann, K.: An investigation of petrochemical emissions during KORUS-AQ: Ozone production, reactive nitrogen evolution, and aerosol production, Elementa, 10, 00079, https://doi.org/10.1525/elementa.2022.00079, 2022.

Levy II, H., Mahlman, J. D., and Moxim, W. J.: A stratospheric source of reactive nitrogen in the unpolluted troposphere, Geophys. Res. Lett., 7, 441–444, https://doi.org/10.1029/GL007i006p00441, 1980.

Levy II, H., Moxim, W. J., Klonecki, A. A., and Kasibhatla, P. S.: Simulated tropospheric NO_x: Its evaluation, global distribution and individual source contributions, J. Geophys Res.-Atmos., 104, 26279–26306, https://doi.org/10.1029/1999JD900442, 1999.

Li, Q., Jacob, D. J., Yantosca, R. M., Heald, C. L., Singh, H. B., Koike, M., Zhao, Y., Sachse, G. W., and Streets, D. G.: A global three-dimensional model analysis of the atmospheric budgets of HCN and CH_3CN: Constraints from aircraft and ground measurements, J. Geophys. Res.-Atmos., 108, 8827, https://doi.org/10.1029/2002JD003075, 2003.

Liang, Q., Rodriguez, J. M., Douglass, A. R., Crawford, J. H., Olson, J. R., Apel, E., Bian, H., Blake, D. R., Brune, W., Chin, M., Colarco, P. R., da Silva, A., Diskin, G. S., Duncan, B. N., Huey, L. G., Knapp, D. J., Montzka, D. D., Nielsen, J. E., Pawson, S., Riemer, D. D., Weinheimer, A. J., and Wisthaler, A.: Reactive nitrogen, ozone and ozone production in the Arctic troposphere and the impact of stratosphere-troposphere exchange, Atmos. Chem. Phys., 11, 13181–13199, https://doi.org/10.5194/acp-11-13181-2011, 2011.

Logan, J. A.: Nitrogen oxides in the troposphere: Global and regional budgets, J. Geophys. Res.-Oceans, 88, 10785–10807, https://doi.org/10.1029/JC088iC15p10785, 1983.

Luo, G., Yu, F., and Moch, J. M.: Further improvement of wet process treatments in GEOS-Chem v12.6.0: impact on global distributions of aerosols and aerosol precursors, Geosci. Model Dev., 13, 2879–2903, https://doi.org/10.5194/gmd-13-2879-2020, 2020.

Marais, E. A., Jacob, D. J., Choi, S., Joiner, J., Belmonte-Rivas, M., Cohen, R. C., Beirle, S., Murray, L. T., Schiferl, L. D., Shah, V., and Jaeglé, L.: Nitrogen oxides in the global upper troposphere: interpreting cloud-sliced NO_2 observations from the OMI satellite instrument, Atmos. Chem. Phys., 18, 17017–17027, https://doi.org/10.5194/acp-18-17017-2018, 2018.

Marais, E. A., Roberts, J. F., Ryan, R. G., Eskes, H., Boersma, K. F., Choi, S., Joiner, J., Abuhassan, N., Redondas, A., Grutter, M., Cede, A., Gomez, L., and Navarro-Comas, M.: New observations of NO_2 in the upper troposphere from TROPOMI, Atmos. Meas. Tech., 14, 2389–2408, https://doi.org/10.5194/amt-14-2389-2021, 2021.

Marenco, A., Thouret, V., Nédélec, P., Smit, H., Helten, M., Kley, D., Karcher, F., Simon, P., Law, K., Pyle, J., Poschmann, G., Von Wrede, R., Hume, C., and Cook, T.: Measurement of ozone and water vapor by Airbus in-service aircraft: The MOZAIC airborne program, an overview, J. Geophys. Res.-Atmos., 103, 25631–25642, https://doi.org/10.1029/98jd00977, 1998.

Mickley, L. J., Murti, P. P., Jacob, D. J., Logan, J. A., Koch, D. M., and Rind, D.: Radiative forcing from tropospheric ozone calculated with a unified chemistry-climate model, J. Geophys. Res.-Atmos., 104, 30153–30172, https://doi.org/10.1029/1999jd900439, 1999.

Murray, L. T., Jacob, D. J., Logan, J. A., Hudman, R. C., and Koshak, W. J.: Optimized regional and interannual variability of lightning in a global chemical transport model constrained by LIS/OTD satellite data, J. Geophys. Res.-Atmos., 117, D20307, https://doi.org/10.1029/2012jd017934, 2012.

Murray, L. T., Logan, J. A., and Jacob, D. J.: Interannual variability in tropical tropospheric ozone and OH: The role of lightning, J. Geophys. Res.-Atmos., 118, 11468–11480, https://doi.org/10.1002/jgrd.50857, 2013.

Murray, L. T., Fiore, A. M., Shindell, D. T., Naik, V., and Horowitz, L. W.: Large uncertainties in global hydroxyl projections tied to fate of reactive nitrogen and carbon, P. Natl. Acad. Sci. USA, 118, e2115204118, https://doi.org/10.1073/pnas.2115204118, 2021.

NASA: Airborne Science Data for Atmospheric Composition, NASA [data set], https://www-air.larc.nasa.gov/cgi-bin/ArcView/arctas?DC8=1, (last access: 24 October 2024), 2009.

NASA: Airborne Science Data for Atmospheric Composition, NASA [data set], https://www-air.larc.nasa.gov/cgi-bin/ArcView/seac4rs (last access: 24 October 2024), 2015.

NASA: EARTHDATA, Korea United States Air Quality Study, NASA [data set], https://asdc.larc.nasa.gov/project/KORUS-AQ (last access: 24 October 2024), 2017.

NASA: EARTHDATA, ATom: Merged Atmospheric Chemistry, Trace Gases, and Aerosols, Version 2, NASA [data set], https://daac.ornl.gov/cgi-bin/dsviewer.pl?ds_id=1925 (last access: 24 October 2024) , 2021.

Nault, B. A., Garland, C., Pusede, S. E., Wooldridge, P. J., Ullmann, K., Hall, S. R., and Cohen, R. C.: Measurements of $CH_3O_2NO_2$ in the upper troposphere, Atmos. Meas. Tech., 8, 987–997, https://doi.org/10.5194/amt-8-987-2015, 2015.

Petzold, A., Thouret, V., Gerbig, C., Zahn, A., Brenninkmeijer, C. A. M., Gallagher, M., Hermann, M., Pontaud, M., Ziereis, H., Boulanger, D., Marshall, J., Nédélec, P., Smit, H. G. J., Friess, U., Flaud, J.-M., Wahner, A., Cammas, J.-P., and Volz-Thomas, A.: Global-scale atmosphere monitoring by in-service aircraft – Current achievements and future prospects of the European Research Infrastructure IAGOS, Tellus B, 67, 28452, https://doi.org/10.3402/tellusb.v67.28452, 2015.

Pollack, I. B., Lerner, B. M., and Ryerson, T. B.: Evaluation of ultraviolet light-emitting diodes for detection of atmospheric NO_2 by photolysis - chemiluminescence, J. Atmos. Chem., 65, 111–125, https://doi.org/10.1007/s10874-011-9184-3, 2010.

Prather, M. J. and Jacob, D. J.: A persistent imbalance in HO_x and NO_x photochemistry of the upper troposphere driven by deep tropical convection, Geophys. Res. Lett., 24, 3189–3192, https://doi.org/10.1029/97GL03027, 1997.

Rap, A., Richards, N. A. D., Forster, P. M., Monks, S. A., Arnold, S. R., and Chipperfield, M. P.: Satellite constraint on the tropospheric ozone radiative effect, Geophys. Res. Lett., 42, 5074–5081, https://doi.org/10.1002/2015gl064037, [illegible]015.

Reed, C., Brumby, C. A., Crilley, L. R., Kramer, L. J., Bloss, W. J., Seakins, P. W., Lee, J. D. https://doi.org/10.1002/2015gl064037 -ment by differential photolysis, Atmos. Meas. Tech., 9, 2483–2495, https://doi.org/10.5194/amt-9-2483-2016, 2016a.

Reed, C., Evans, M. J., Di Carlo, P., Lee, J. D., and Carpenter, L. J.: Interferences in photolytic NO2 measurements: explanation for an apparent missing oxidant?, Atmos. Chem. Phys., 16, 4707–4724, https://doi.org/10.5194/acp-16-4707-2016, 2016b.

Roberts, J. M.: The atmospheric chemistry of organic nitrates, Atmos. Environ. A-Gen., 24, 243–287, https://doi.org/10.1016/0960-1686(90)90108-Y, 1990.

Roberts, J. M., Williams, J., Baumann, K., Buhr, M. P., Goldan, P. D., Holloway, J., Hübler, G., Kuster, W. C., McKeen, S. A., Ryerson, T. B., Trainer, M., Williams, E. J., Fehsenfeld, F. C., Bertman, S. B., Nouaime, G., Seaver, C., Grodzinsky, G., Rodgers, M., and Young, V. L.: Measurements of PAN, PPN, and MPAN made during the 1994 and 1995 Nashville Intensives of the Southern Oxidant Study: Implications for regional ozone production from biogenic hydrocarbons, J. Geophys. Res.-Atmos., 103, 22473–22490, https://doi.org/10.1029/98JD01637, 1998.

Roberts, J. M., Flocke, F., Stroud, C. A., Hereid, D., Williams, E., Fehsenfeld, F., Brune, W., Martinez, M., and Harder, H.:

Ground-based measurements of peroxycarboxylic nitric anhydrides (PANs) during the 1999 Southern Oxidants Study Nashville Intensive, J. Geophys. Res.-Atmos., 107, ACH 1-1–ACH 1-10, https://doi.org/10.1029/2001JD000947, 2002.

Ryerson, T. B., Williams, E. J., and Fehsenfeld, F. C.: An efficient photolysis system for fast-response NO_2 measurements, J. Geophys. Res.-Atmos., 105, 26447–26461, https://doi.org/10.1029/2000JD900389, 2000.

Schultz, M. G., Jacob, D. J., Wang, Y., Logan, J. A., Atlas, E. L., Blake, D. R., Blake, N. J., Bradshaw, J. D., Browell, E. V., Fenn, M. A., Flocke, F., Gregory, G. L., Heikes, B. G., Sachse, G. W., Sandholm, S. T., Shetter, R. E., Singh, H. B., and Talbot, R. W.: On the origin of tropospheric ozone and NO_x over the tropical South Pacific, J. Geophys. Res.-Atmos., 104, 5829–5843, https://doi.org/10.1029/98jd02309, 1999.

Seltzer, K. M., Vizuete, W., and Henderson, B. H.: Evaluation of updated nitric acid chemistry on ozone precursors and radiative effects, Atmos. Chem. Phys., 15, 5973–5986, https://doi.org/10.5194/acp-15-5973-2015, 2015.

Shah, V., Jacob, D. J., Dang, R., Lamsal, L. N., Strode, S. A., Steenrod, S. D., Boersma, K. F., Eastham, S. D., Fritz, T. M., Thompson, C., Peischl, J., Bourgeois, I., Pollack, I. B., Nault, B. A., Cohen, R. C., Campuzano-Jost, P., Jimenez, J. L., Andersen, S. T., Carpenter, L. J., Sherwen, T., and Evans, M. J.: Nitrogen oxides in the free troposphere: implications for tropospheric oxidants and the interpretation of satellite NO2 measurements, Atmos. Chem. Phys., 23, 1227–1257, https://doi.org/10.5194/acp-23-1227-2023, 2023.

Silvern, R. F., Jacob, D. J., Travis, K. R., Sherwen, T., Evans, M. J., Cohen, R. C., Laughner, J. L., Hall, S. R., Ullmann, K., Crounse, J. D., Wennberg, P. O., Peischl, J., and Pollack, I. B.: Observed NO/NO_2 Ratios in the Upper Troposphere Imply Errors in NO-NO_2-O_3 Cycling Kinetics or an Unaccounted NO_x Reservoir, Geophys. Res. Lett., 45, 4466–4474, https://doi.org/10.1029/2018gl077728, 2018.

Singh, H. B.: Reactive nitrogen in the troposphere, Environ. Sci. Technol., 21, 320–327, https://doi.org/10.1021/es00158a001, 1987.

Singh, H. B., Thompson, A. M., and Schlager, H.: SONEX airborne mission and coordinated POLINAT-2 activity: Overview and accomplishments, Geophys. Res. Lett., 26, 3053–3056, https://doi.org/10.1029/1999GL900588, 1999.

Singh, H. B., Brune, W. H., Crawford, J. H., Jacob, D. J., and Russell, P. B.: Overview of the summer 2004 Intercontinental Chemical Transport Experiment–North America (INTEX-A), J. Geophys. Res.-Atmos., 111, D24S01, https://doi.org/10.1029/2006JD007905, 2006.

Singh, H. B., Brune, W. H., Crawford, J. H., Flocke, F., and Jacob, D. J.: Chemistry and transport of pollution over the Gulf of Mexico and the Pacific: spring 2006 INTEX-B campaign overview and first results, Atmos. Chem. Phys., 9, 2301–2318, https://doi.org/10.5194/acp-9-2301-2009, 2009.

Sörgel, M., Regelin, E., Bozem, H., Diesch, J.-M., Drewnick, F., Fischer, H., Harder, H., Held, A., Hosaynali-Beygi, Z., Martinez, M., and Zetzsch, C.: Quantification of the unknown HONO daytime source and its relation to NO_2, Atmos. Chem. Phys., 11, 10433–10447, https://doi.org/10.5194/acp-11-10433-2011, 2011.

Stettler, M. E. J., Eastham, S., and Barrett, S. R. H.: Air quality and public health impacts of UK airports. Part I: Emissions, Atmos. Environ., 45, 5415–5424, https://doi.org/10.1016/j.atmosenv.2011.07.012, 2011.

Stratmann, G., Ziereis, H., Stock, P., Brenninkmeijer, C. A. M., Zahn, A., Rauthe-Schöch, A., Velthoven, P. V., Schlager, H., and Volz-Thomas, A.: NO and NO_y in the upper troposphere: Nine years of CARIBIC measurements onboard a passenger aircraft, Atmos. Environ., 133, 93–111, https://doi.org/10.1016/j.atmosenv.2016.02.035, 2016.

Talbot, R. W., Dibb, J. E., Scheuer, E. M., Kondo, Y., Koike, M., Singh, H. B., Salas, L. B., Fukui, Y., Ballenthin, J. O., Meads, R. F., Miller, T. M., Hunton, D. E., Viggiano, A. A., Blake, D. R., Blake, N. J., Atlas, E., Flocke, F., Jacob, D. J., and Jaegle, L.: Reactive nitrogen budget during the NASA SONEX Mission, Geophys. Res. Lett., 26, 3057–3060, https://doi.org/10.1029/1999GL900589, 1999.

The International GEOS-Chem User Community: geoschem/GC-Classic: GEOS-Chem 13.0.2 (13.0.2), Zenodo [code], https://doi.org/10.5281/zenodo.4681204, 2021.

Thomas, K., Berg, M., Boulanger, D., Houben, N., Gressent, A., Nédélec, P., Pätz, H.-W., Thouret, V., and Volz-Thomas, A.: Climatology of NO_y in the troposphere and UT/LS from measurements made in MOZAIC, Tellus B, 67, 28793, https://doi.org/10.3402/tellusb.v67.28793, 2015.

Thompson, C. R., Wofsy, S. C., Prather, M. J., Newman, P. A., Hanisco, T. F., Ryerson, T. B., Fahey, D. W., Apel, E. C., Brock, C. A., Brune, W. H., Froyd, K., Katich, J. M., Nicely, J. M., Peischl, J., Ray, E., Veres, P. R., Wang, S., Allen, H. M., Asher, E., Bian, H., Blake, D., Bourgeois, I., Budney, J., Bui, T. P., Butler, A., Campuzano-Jost, P., Chang, C., Chin, M., Commane, R., Correa, G., Crounse, J. D., Daube, B., Dibb, J. E., Digangi, J. P., Diskin, G. S., Dollner, M., Elkins, J. W., Fiore, A. M., Flynn, C. M., Guo, H., Hall, S. R., Hannun, R. A., Hills, A., Hintsa, E. J., Hodzic, A., Hornbrook, R. S., Huey, L. G., Jimenez, J. L., Keeling, R. F., Kim, M. J., Kupc, A., Lacey, F., Lait, L. R., Lamarque, J.-F., Liu, J., Mckain, K., Meinardi, S., Miller, D. O., Montzka, S. A., Moore, F. L., Morgan, E. J., Murphy, D. M., Murray, L. T., Nault, B. A., Neuman, J. A., Nguyen, L., Gonzalez, Y., Rollins, A., Rosenlof, K., Sargent, M., Schill, G., Schwarz, J. P., St. Clair, J. M., Steenrod, S. D., Stephens, B. B., Strahan, S. E., Strode, S. A., Sweeney, C., Thames, A. B., Ullmann, K., Wagner, N., Weber, R., Weinzierl, B., Wennberg, P. O., Williamson, C. J., Wolfe, G. M., and Zeng, L.: The NASA Atmospheric Tomography (ATom) Mission: Imaging the chemistry of the global atmosphere, B. Am. Meteorol. Soc., 103, E761–E790, https://doi.org/10.1175/bams-d-20-0315.1, 2021.

Toon, O. B., Maring, H., Dibb, J., Ferrare, R., Jacob, D. J., Jensen, E. J., Luo, Z. J., Mace, G. G., Pan, L. L., Pfister, L., Rosenlof, K. H., Redemann, J., Reid, J. S., Singh, H. B., Thompson, A. M., Yokelson, R., Minnis, P., Chen, G., Jucks, K. W., and Pszenny, A.: Planning, implementation, and scientific goals of the Studies of Emissions and Atmospheric Composition, Clouds and Climate Coupling by Regional Surveys ($SEAC^4RS$) field mission, J. Geophys. Res.-Atmos., 121, 4967–5009, https://doi.org/10.1002/2015jd024297, 2016.

Travis, K. R., Jacob, D. J., Fisher, J. A., Kim, P. S., Marais, E. A., Zhu, L., Yu, K., Miller, C. C., Yantosca, R. M., Sulprizio, M. P., Thompson, A. M., Wennberg, P. O., Crounse, J. D., St. Clair,

J. M., Cohen, R. C., Laughner, J. L., Dibb, J. E., Hall, S. R., Ullmann, K., Wolfe, G. M., Pollack, I. B., Peischl, J., Neuman, J. A., and Zhou, X.: Why do models overestimate surface ozone in the Southeast United States?, Atmos. Chem. Phys., 16, 13561–13577, https://doi.org/10.5194/acp-16-13561-2016, 2016.

Travis, K. R., Heald, C. L., Allen, H. M., Apel, E. C., Arnold, S. R., Blake, D. R., Brune, W. H., Chen, X., Commane, R., Crounse, J. D., Daube, B. C., Diskin, G. S., Elkins, J. W., Evans, M. J., Hall, S. R., Hintsa, E. J., Hornbrook, R. S., Kasibhatla, P. S., Kim, M. J., Luo, G., McKain, K., Millet, D. B., Moore, F. L., Peischl, J., Ryerson, T. B., Sherwen, T., Thames, A. B., Ullmann, K., Wang, X., Wennberg, P. O., Wolfe, G. M., and Yu, F.: Constraining remote oxidation capacity with ATom observations, Atmos. Chem. Phys., 20, 7753–7781, https://doi.org/10.5194/acp-20-7753-2020, 2020.

Travis, K. R., Nault, B. A., Crawford, J. H., Bates, K. H., Blake, D. R., Cohen, R. C., Fried, A., Hall, S. R., Huey, L. G., Lee, Y. R., Meinardi, S., Min, K.-E., Simpson, I. J., and Ullman, K.: Impact of improved representation of volatile organic compound emissions and production of NO_x reservoirs on modeled urban ozone production, Atmos. Chem. Phys., 24, 9555–9572, https://doi.org/10.5194/acp-24-9555-2024, 2024.

Volz-Thomas, A., Berg, M., Heil, T., Houben, N., Lerner, A., Petrick, W., Raak, D., and Pätz, H.-W.: Measurements of total odd nitrogen (NO_y) aboard MOZAIC in-service aircraft: instrument design, operation and performance, Atmos. Chem. Phys., 5, 583–595, https://doi.org/10.5194/acp-5-583-2005, 2005.

Weinheimer, A. J.: Chemical Methods: Chemiluminscence, Chemical Amplification, Electrochemistry, and Derivation, in: Analytical Techniques for Atmospheric Measurement, 311–360, https://doi.org/10.1002/9780470988510.ch7, 2006.

Weinheimer, A. J., Walega, J. G., Ridley, B. A., Gary, B. L., Blake, D. R., Blake, N. J., Rowland, F. S., Sachse, G. W., Anderson, B. E., and Collins, J. E.: Meridional distributions of NO_x, NO_y, and other species in the lower stratosphere and upper troposphere during AASE II, Geophys. Res. Lett., 21, 2583–2586, https://doi.org/10.1029/94GL01897, 1994.

Worden, H. M., Bowman, K. W., Kulawik, S. S., and Aghedo, A. M.: Sensitivity of outgoing longwave radiative flux to the global vertical distribution of ozone characterized by instantaneous radiative kernels from Aura-TES, J. Geophys. Res., 116, D14115, https://doi.org/10.1029/2010jd015101, 2011.

Zahn, A., Brenninkmeijer, C. A. M., Asman, W. A. H., Crutzen, P. J., Heinrich, G., Fischer, H., Cuijpers, J. W. M., and van Velthoven, P. F. J.: Budgets of O_3 and CO in the upper troposphere: CARIBIC passenger aircraft results 1997–2001, J. Geophys. Res.-Atmos., 107, ACH 6-1–ACH 6-20, https://doi.org/10.1029/2001JD001529, 2002.